

Dissertation
submitted to the
Combined Faculty of Natural Sciences and Mathematics
of Heidelberg University, Germany
for the degree of
Doctor of Natural Sciences

Put forward by

Xiyuan Xia

born in: Xinjiang, China

Oral examination: 27 July 2022

Towards a more reliable ultracold mixture platform

Referees: Prof. Dr. Markus K. Oberthaler
Prof. Dr. Lauriane Chomaz

Abstract

Ultracold mixture experiments provide a great platform to study fundamental physics as well as to develop quantum technologies. Improving the reliability and stability of these platforms still remains as a significant challenge to be solved. In this thesis, work is carried out to improve a sodium-lithium ultracold mixture platform. Stability of Bose-Einstein condensate production is improved, as well as the ability to exercise more precise control over the internal states of both species.

To improve the stability, the vacuum and optical setups are simplified and each experimental stage is optimised. Better control of internal states via long Rabi cycles is managed by improving the magnetic field stability. Local confinement is achieved using an 1D optical lattice at 610 nm. The imaging and the microwave system are characterised using the optical lattice. Additionally, progress has been made towards observing single atom dynamics in a sodium MOT with fluorescence imaging.

Zusammenfassung

Experimente mit ultrakalten Atomgemischen bieten eine ausgezeichnete Plattform für die Untersuchung der Grundlagenphysik und die Entwicklung von Quantentechnologien. Die Zuverlässigkeit und Stabilität dieser Plattformen ist nach wie vor eine der Herausforderungen, die es zu lösen gilt. Im Laufe dieser Arbeit wurde an der Verbesserung eines Natrium-Lithium-Quantengasexperiments gearbeitet. Die Stabilität der Produktion von Bose-Einstein-Kondensaten wurde verbessert und eine präzisere Kontrolle über die internen Zustände beider Spezies erreicht.

Um die Stabilität zu verbessern, wurden das Vakuum und der optische Aufbau vereinfacht und die einzelnen experimentellen Schritte optimiert. Eine bessere Kontrolle der internen Zustände über lange Rabi-Zyklen wurde durch die Verbesserung der Magnetfeldstabilität erreicht. Die lokale Begrenzung wurde mit Hilfe eines optischen 1D-Gitters bei 610 nm erreicht. Die Bildgebung und das Mikrowellensystem wurden mittels des optischen Gitters charakterisiert. Darüber hinaus wurden Fortschritte bei der Beobachtung der Dynamik einzelner Atome in einer Natrium-MOT mit Fluoreszenzabbildung erzielt.

Contents

1	Ultracold mixtures	1
1.1	Overview	1
1.2	An ultracold sodium-lithium mixture platform	4
2	Motivation: a platform for quantum simulation and computation	9
2.1	A building block towards simulating local $U(1)$ gauge invariance	9
2.2	Experimental sequence	12
2.3	A summary of the experimental results	15
2.3.1	A building block model: spin changing collisions at the mean field level	15
2.3.2	Evolution time	16
2.3.3	Initial condition	17
2.3.4	Offset magnetic field	18
2.4	Drawbacks of the platform	20
2.4.1	Stability of BEC production	20
2.4.2	Spatial dynamics in sodium	21
2.5	Quantum computation using ultracold mixtures	23
2.5.1	A theoretical model	23
2.5.2	The experimental protocol	25
3	Theoretical Background	27
3.1	Atom-light interaction	27
3.1.1	The interaction Hamiltonian	27
3.1.2	Atoms in static magnetic fields	28
3.1.3	Two-level system	29
3.1.4	Rabi oscillations	30
3.1.5	Bloch sphere	31
3.1.6	Ramsey spectroscopy	33
3.1.7	Dressed states	34

3.1.8	Rapid adiabatic passage	35
3.2	Quantum degenerate gases	35
3.2.1	A non-interacting BEC in a harmonic trap	36
3.2.2	Bogoliubov approximation and Gross-Pitaevskii Equation	38
3.2.3	Thomas-Fermi approximation	39
3.2.4	Tunable interactions	40
3.2.5	Expansion of condensates	41
3.2.6	Quantum degenerate mixtures	41
4	The road to degeneracy	43
4.1	Vacuum system	43
4.1.1	An overview of the vacuum system	44
4.1.2	Lifetime of the traps	45
4.1.3	Differential pumping stages	46
4.1.4	Ultra high vacuum generation	47
4.2	Atomic source	51
4.2.1	Old oven design	51
4.2.2	Oven change	52
4.2.3	Drawbacks of the old design	53
4.2.4	Effusive atomic sources	54
4.2.5	Characterisation of the new oven design	55
4.3	Laser Systems	58
4.3.1	Spectroscopy path	59
4.3.2	MOT and repumper path	59
4.3.3	Zeeman slower path	60
4.3.4	Spin-polarisation path	61
4.3.5	Imaging path	62
4.4	Magnetic fields	63
4.4.1	Zeeman slower coils	63
4.4.2	Cloverleaf Trap coils	63
4.4.3	Fast switching of the magnetic fields	64
4.5	Optical dipole trap	65
4.5.1	Trap setup	66
4.5.2	Trap geometry and frequencies	66
4.5.3	Power stabilisation of the trap	68
4.6	Microwave and radio setup	69
4.6.1	Frequency sources	69

4.6.2	I/Q mixers	70
4.6.3	Antennas	70
4.6.4	Controlling the pulses	71
4.7	Imaging system	71
4.7.1	Absorption imaging	71
4.7.2	Optical setup	72
4.8	Experimental control system	73
4.8.1	Hardware for control	73
4.8.2	Software for control	74
4.9	Experimental sequence for double BECs	75
4.9.1	MOT stage	76
4.9.2	Spin-polarisation stage	77
4.9.3	Magnetic trap and evaporative cooling stage	77
4.9.4	Optical dipole trap stage	78
4.9.5	TOF and readout stage	78
5	Characterisation of the platform	81
5.1	Stability of atomic sample production	81
5.2	Internal states manipulation	83
5.2.1	A toy model for magnetic field fluctuations	86
5.2.2	Stabilisation scheme	89
5.2.3	Rabi oscillations with stabilisation	93
5.3	Local confinement	95
5.3.1	Optical lattice	95
5.3.2	Spatial inhomogeneity of one-photon coupling	95
5.3.3	Detection noise of the imaging system	97
5.4	Fluorescence imaging	100
5.4.1	A toy model for atom number dynamics	100
5.4.2	Experimental observations	100
6	Outlook	105
	Bibliography	107

1 Ultracold mixtures

This chapter provides an overview of ultracold atomic mixtures. The advantages as well as the challenges faced conducting mixture experiments are discussed. More specifically, a general description of the sodium-lithium mixture experiment (NaLi) is presented along with the experimental tools that can be used on the platform.

1.1 Overview

Experiments with ultracold atomic gases have proven to be tremendously successful in the last 30 years. Apart from deepening the understanding of atomic systems [1–5], atomic gas experiments have also provided paths to research areas such as many-body physics [6], quantum information processing [7, 8], quantum optics [9] and simulating condensed matter systems [10, 11].

A key feature of the field of ultracold atomic gases is the capability to have full control over the microscopic parameters of the experimental systems. Theoretical study of such systems have been made possible with Hamiltonians, which help to describe the experimental systems and develop new ideas to be implemented on them. Full control over the microscopic parameters makes the implementation of new ideas on the systems possible and also contributes to the developments of new techniques to achieve better control of these systems.

Interactions in degenerate quantum gas experiments play a fundamental role in controlling these systems. While long range dipolar interactions have been made possible through experiments with ultracold molecules [12] and some rare earth metals such as dysprosium [13], the interactions in experiments with ultracold atomic gases are predominantly isotropic, short-range contact collisions. Such interactions are well described by scattering theory and can be tuned using Feshbach resonances. Apart from tuning interactions, other experimental parameters such as the confinement, magnetic field, atom number and temperature can also be controlled precisely in the experiments.

Although atoms can be confined both magnetically and optically in these experiments, the use of optical dipole traps liberates the spin degree of freedom which provides more control over the experiments. The optical confinement used in the experiments can range from a single atom in an optical tweezer to millions of atoms in an optical dipole trap [14, 15]. The geometry of the confinements can also be tailored using tools such as optical lattices [16, 17]. Optical dipole traps provide the confinements of atoms globally, often serving as a starting point for manipulation and control of atoms. On the other hand, local control of atoms is usually carried out with tools like optical tweezers and optical lattices.

In particular, optical lattices have been studied extensively over the past 20 years. Thus, a versatile toolbox for the precise control of atoms has been developed by using different combinations of external fields and optical lattice parameters. Interactions among atoms in an optical lattice can be tuned by changing the lattice depth, where a large lattice depth leads to a small probability of tunnelling between different sites of the lattice as well as strong interactions among atoms on each lattice site. The relatively simple setup needed for optical lattices in 1D makes confinements in higher dimensions feasible by adding extra laser beams in different directions. Different geometries of the confinement such as triangular lattices or Kagome lattices [18, 19] can be achieved by changing the positions of the lattice beams. The degree of freedom of motion in certain directions can be frozen out by tightening the confinement in that direction. Effective 1D or 2D systems have been experimentally demonstrated in recent years [20, 21]. Beyond optical lattices created by using a single wavelength, extra lasers with different wavelengths can be used to create superlattices [22]. The polarisation of the laser light can also be manipulated to achieve spin-dependent optical lattices [23].

In order to obtain the properties of atomic clouds, three main detection techniques are commonly used in the field, namely absorption imaging, fluorescence imaging and phase contrast imaging [25]. For degenerate gases with high phase-space density in optical dipole traps, absorption imaging is used, often along with time of flight measurement by switching off the trapping potential. On the other hand, to determine in situ profiles of atomic clouds, phase contrast imaging becomes more reliable than absorption imaging due to the high optical density of the cloud. In the single atom regime, fluorescence imaging is a common choice as it produces a large signal-to-noise ratio with very low background noise. In optical tweezers and lattices, fluorescence imaging has been proven as a non-destructive and powerful tool [26, 27]. Internal state detection has also been made possible both in optical dipole traps and optical lattices such as using a magnetic field gra-

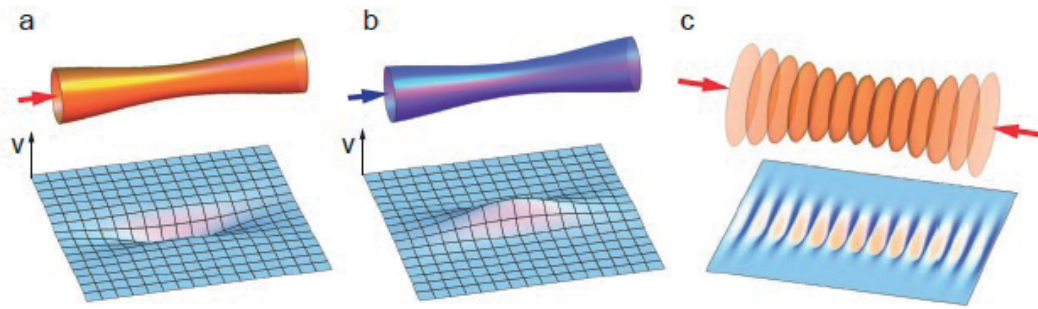


Figure 1.1. An attractive potential for atoms is created using red detuned light as shown in **a**. The blue detuned light creates a repulsive potential as shown in **b**. An optical lattice in 1D can be formed by overlapping two counter-propagating laser beams (**c**). Taken from [24].

dient (Stern Gerlach) to separate internal states [28] as well as other advanced techniques used in quantum gas microscopes [29, 30].

The spin-independent nature of optical trapping provides a path to manipulate the internal states of atoms with the help of the Zeeman effect. The energy difference between internal states induced by an external magnetic field can be used to study the systems of spinor gases. Other parameters such as temperature and density are tunable via evaporation inside the traps. Overall, ultracold atom experiments provide a clean and highly controllable platform for research and industry applications.

In recent years, quantum degenerate mixtures of atomic gases have been a main focus of intensive theoretical and experimental research. Ultracold mixtures provide a path towards rich physics which is inaccessible for single species experiments by adding other species [14, 31–40]. The addition of one extra specie brings extra interactions between different species along with the existing intraspecies interactions, while keeping the versatility and control from the single-specie experiments. Such interactions open doors to the developments of new cooling techniques such as sympathetic cooling, which was instrumental for reaching Fermi degeneracy [34]. Sympathetic cooling is now a commonly used technique in the ultracold mixtures experiments.

Research on the dynamics of degenerate atomic mixtures using short-range contact interactions provides tools to study many interesting physics problems, such as simulating lattice gauge theory [41], building a quantum refrigerator to test thermodynamics in the quantum regime [42] and carrying out quantum computation [43] using the internal states of the mixtures. Other areas of research such as using the

mixtures to create degenerate samples of hetero-nuclear ground state molecules have proven to be a success and have opened an entire new world of quantum simulation and computation, as well one for studying fundamental physics [12, 44].

As a short summary, the ultracold mixtures experiments add a new dimension to the single-specie experiments in addition to benefiting from the great versatility and controllability of the single-specie experiments. However, the introduction of an extra specie also complicates the experiments by adding extra laser systems and electronics. A significant amount of effort can still be made towards simplifying the experimental setups and improving the stability of these experiments.

1.2 An ultracold sodium-lithium mixture platform

The work described in this thesis was carried out on a sodium-lithium mixture experiment (NaLi). Around 3×10^5 sodium atoms and 5×10^4 lithium atoms are cooled to quantum degeneracy in an optical dipole trap with both sodium and lithium atoms being in the state of $|F = 1, m_F = 1\rangle$ as the starting point of the experiment. The Hamiltonian of the system is as follows

$$\hat{H}_{NaLi} = \hat{H}_s + \hat{H}_{ss} + \hat{H}_{NL} \quad (1.1)$$

where the first term \hat{H}_s is the Hamiltonian of the atoms trapped in a potential V_s in the presence of an external magnetic field,

$$\hat{H}_s = \int d^3\mathbf{x} \sum_{\alpha} \hat{\psi}_{s,\alpha}^{\dagger}(\mathbf{x}) \left[\frac{-\nabla_{\mathbf{x}}^2}{2m_s} + V_s(\mathbf{x}) + E_{s,\alpha}(\mathbf{B}) \right] \hat{\psi}_{s,\alpha}(\mathbf{x}) \quad (1.2)$$

In the experiment, the trapping potential is primarily provided by a dipole laser at 1070 nm which is far blue detuned for both sodium and lithium atoms. The spin-independent nature of the trapping potential enables the spin degree of freedom in the system, which is vital for studying the dynamics of spinor gases and engineering quantum applications with spin states. Various levels of confinements in different directions is achieved by a difference in trapping frequencies; the trapping frequency along the direction of gravity is roughly twice the trapping frequencies in the other two directions to compensate for the effect of gravity in the experiment. Local confinements on top of the dipole trap can be achieved by using optical lattices with a tunable laser with a wavelength range of 510 nm to 1020 nm. With such flexibility, confinements in different directions and magnitudes can be realised by tuning the wavelength and the power of the lattice laser. The detail of the optical lattice realised in this experiment can be found in Section 5.3.

Another important tool in the experiment is the control over the magnetic field. The Zeeman shift due to an external magnetic field can be described by using the Breit-Rabi formula. For simplicity, the linear and quadratic Zeeman shifts can be expressed in Equation 1.3. Precise control over the external magnetic field provides the possibility of working with the internal spin states. High stability magnetic fields are desirable for observing spin dynamics such as spin-changing collisions, as well as maintaining precise control over internal spin states such as in Rabi and Ramsey spectroscopy.

$$E_s^m(\mathbf{B}) = p_m(\mathbf{B})m_F + q_m(\mathbf{B})m_F^2 \quad (1.3)$$

where $p_m(\mathbf{B})$ parameterises the linear Zeeman shift and $q_m(\mathbf{B})$ the quadratic Zeeman shift.

In systems with dilute ultracold gases, it is usually sufficient to consider two body interactions. Collisions between two atoms of the same atomic species are characterised by the s-wave scattering lengths in different total spin channels [45, 46]. Therefore the second term \hat{H}_{ss} describes the interactions within the same specie.

$$\hat{H}_{ss} = \frac{1}{2} \int d^3(\mathbf{x}) \sum_{\alpha,\beta} g_{\alpha,\beta}^s \hat{\psi}_{s,\alpha}^\dagger(\mathbf{x}) \hat{\psi}_{s,\beta}^\dagger(\mathbf{x}) \hat{\psi}_{s,\beta}(\mathbf{x}) \hat{\psi}_{s,\alpha}(\mathbf{x}) \quad (1.4)$$

where $g_{\alpha,\beta}^s = \frac{4\pi\hbar^2}{m_s}$ is the interaction constant. It is determined by the following scattering length for sodium and lithium, $a_{11}^N = a_{10}^N = a_{01}^N = 55a_B$, $a_{00}^N = 53a_B$, $a_{11}^L = a_{10}^L = a_{01}^L = 6.8a_B$ and $a_{00}^L = 12.5a_B$ [45].

The third term \hat{H}_{NL} describes the interactions between sodium and lithium atoms in the system,

$$\hat{H}_{NL} = \int d^3(\mathbf{x}) \sum_{\alpha,\beta} g_{\alpha,\beta}^{mix} \hat{\psi}_{N,\alpha}^\dagger(\mathbf{x}) \hat{\psi}_{L,\beta}^\dagger(\mathbf{x}) \hat{\psi}_{L,\beta}(\mathbf{x}) \hat{\psi}_{N,\alpha}(\mathbf{x}) \quad (1.5)$$

where $a_{00}^{mix} = a_{01}^{mix} = a_{10}^{mix} = 19.65a_B$, $a_{11}^{mix} = 20a_B$ and the field operators $\hat{\psi}_{s,\alpha}(\mathbf{x})$ obey bosonic commutation relations

$$[\hat{\psi}_{s,\alpha}, \hat{\psi}_{s',\beta}] = \delta_{ss'} \delta_{\alpha\beta} \delta(\mathbf{x} - \mathbf{y}) \quad (1.6)$$

An example of the interactions between two species is hetero-nuclear spin-changing collisions. The Hamiltonian of the interaction is given by

$$\hat{H}_{SCC} = g^{SCC} \int d^3\mathbf{x} \psi_{N,0}^\dagger(\mathbf{x}) \psi_{L,1}^\dagger(\mathbf{x}) \psi_{N,1}(\mathbf{x}) \psi_{L,0}(\mathbf{x}) + h.c \quad (1.7)$$

where the interaction strength is given by $g^{SCC} = \frac{2\pi\hbar^2}{\mu} a_{SCC}$ and $a_{SCC} = 0.35a_B$.

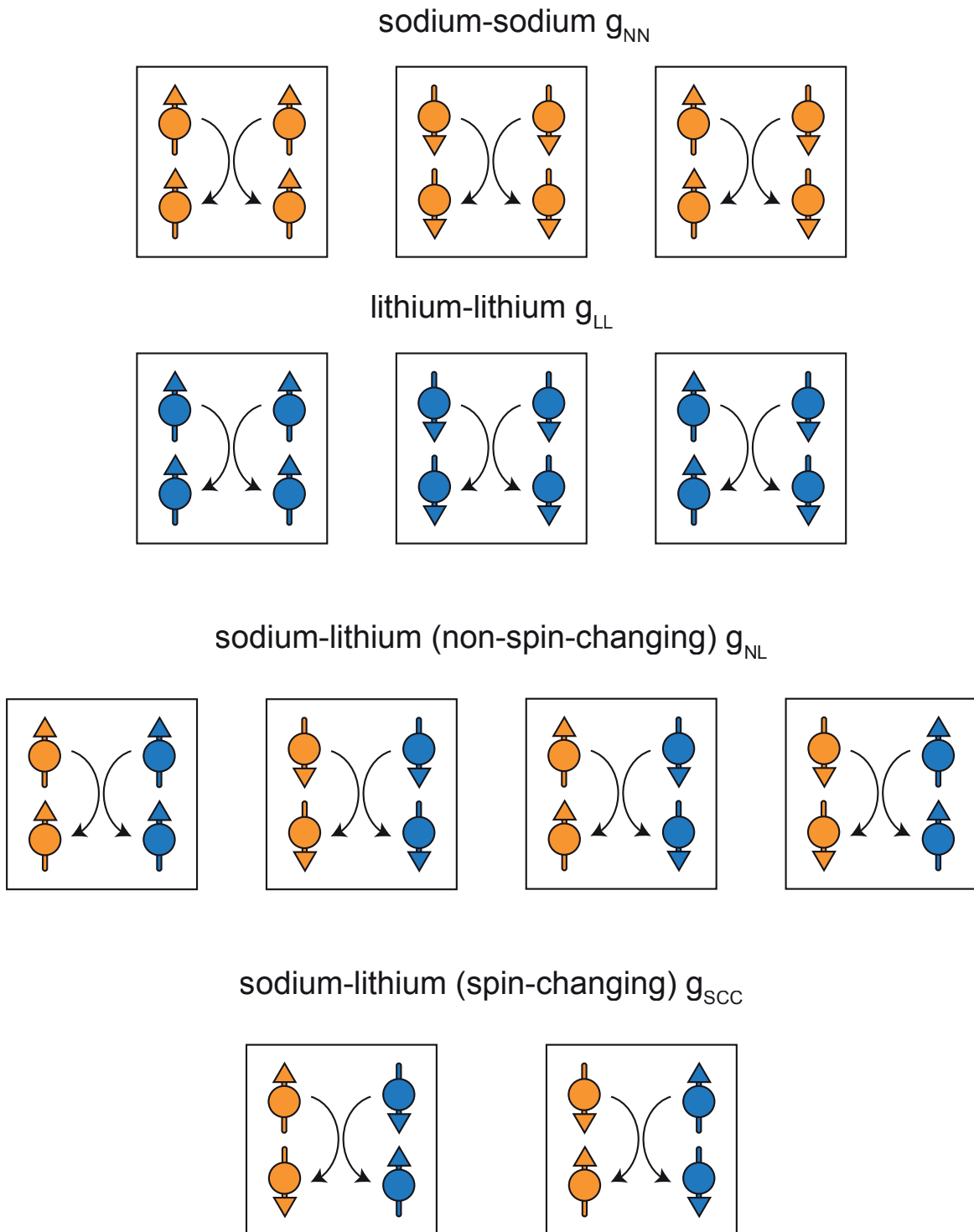


Figure 1.2. Different types of collisions which occur in the system. Adapted from [47].

While both the intraspecies and interspecies interactions are determined by the scattering length of atoms in different states, controlling such interactions have been made possible through Feshbach resonances [48]. Both the sign and magnitude of the scattering length can be tuned via the use of Feshbach resonances, which

remains an important tool to manipulate the behaviour of ultracold quantum gases.

The outline of this thesis is given by the following,

- In Chapter **2**, a project carried out concerning $U(1)$ gauge theory over the course of this thesis is discussed along with a proposed project on quantum computing. The experimental platform served as a quantum simulator in the first project and would serve as a quantum computer in the proposed project. Both projects serve as a motivation of the work described in this thesis.
- In Chapter **3**, the theory behind atom-light interaction, Zeeman shifts and the two-level model is introduced. Techniques used in this thesis such as Rabi and Ramsey spectroscopy are discussed. Moreover, a short summary on the theory behind Bose-Einstein condensates is given.
- In Chapter **4**, both the hardware and the software of the experimental platform are introduced as well as the experimental sequence needed to achieve quantum degeneracy of both species. The main focus is on the modifications and improvements made to the experimental platform.
- In Chapter **5**, the improvements made to the platform are characterised. The improvements on both the stability and atom number of the BECs produced on the platform are shown. The improved magnetic field stabilisation scheme leads to longer Rabi cycles. A simple toy model is presented to understand the effect of both microwave (MW) power and magnetic field fluctuations on Rabi oscillations. Local confinement of atoms using a 1D optical lattice is demonstrated. Further characterisation of the imaging system and MW gradient across the atomic cloud is carried out by taking advantage of a coherent spin state inside the lattice. Efforts made working towards observing single atom dynamics in a sodium MOT using fluorescence imaging are also presented as the first step towards non-destructive imaging on the platform.
- In Chapter **6**, an outlook on further improvements that can be implemented on similar platforms is given. The improvements includes reducing the complexity of the optical setup, active power stabilisation of the MW and RF systems and temperature stabilisation of critical components of the platform. On the detection side, the imaging calibration could be redone as well as work towards non-destructive imaging inside optical lattices.

2 Motivation: a platform for quantum simulation and computation

The versatility of the experimental platform makes it possible to act as a simulator or a computer. A project on constructing a building block towards simulating local $U(1)$ gauge invariance by using the platform as an analogue quantum simulator was carried out during the time spent working on this thesis. Another scheme was shortly proposed after the completion of the project to use the platform as a gate based quantum computer. In this chapter, a short summary of the project is given with an emphasis on the drawbacks of the platform identified during the project along with the improvements needed to progress towards the quantum computing proposal. A detail analysis on the $U(1)$ gauge theory project can be found by in [41, 47] and both projects only serve as a motivation for this thesis.

2.1 A building block towards simulating local $U(1)$ gauge invariance

Gauge theories are one of the cornerstones of modern physics, and more specifically, the world of high energy [49, 50] and condensed matter physics [51]. The interactions between electrons and the electromagnetic field in quantum electrodynamics can be described using a $U(1)$ gauge symmetry. Such a symmetry gives constraints on the dynamics between matter and gauge fields which leads to Schwinger pair-production [52] and symmetry breaking due to confinement [53–55].

To be able to understand and solve these problems numerically, lattice gauge theories are used to formulate gauge theories onto a discrete lattice. However, despite all the efforts put in the field, predicting the dynamics far from equilibrium numerically is still challenging due to limitations of computing power. As a result, building a quantum simulator for such problems attracted a lot interests in the field of ultracold quantum gases [56–58].

The sodium-lithium mixture machine described in the Section 2.2 provides an ideal platform to implement the building block of a $U(1)$ gauge theory. Experimentally, the building block is realised using spin-changing collisions between sodium and lithium atoms at a given magnetic field of around 2 G [45, 59]. The sodium atoms act as the matter field and the lithium atoms as the gauge field. The conservation of angular momentum in the system guarantees the fact that $U(1)$ gauge symmetry is fulfilled. The building block includes all the crucial gauge invariance between the gauge and matter fields with the potential to be extended into a one dimensional lattice gauge theory, in which several of the build blocks will need to be engineered [41]. The advantage of such a set up is its scalability and protection of the gauge invariance.

From the Hamiltonian \hat{H}_{NaLi} of the experimental system given in Section 2.2, several assumptions were made in order to derive the building block model. The Hamiltonian \hat{H}_{NaLi} can be separated into two parts, the density component and the spin component. The spatial dynamics is assumed to be frozen out for atoms confined in tight traps by using a single mode approximation. Under a single mode approximation, the field operator $\hat{\psi}_{s,\alpha}(\mathbf{x})$ can be written as

$$\hat{\psi}_{s,\alpha}(\mathbf{x}) \approx \Phi_{s,\alpha}(\mathbf{x})\hat{b}_{s,\alpha} \quad (2.1)$$

where $\Phi_{s,\alpha}(\mathbf{x})$ is a wavefunction determined from the ground state of the Gross-Pitaevskii equation, $\hat{b}_{s,\alpha}$ is the annihilation operator for the corresponding specie and magnetic substate. Using the approximation, the Hamiltonian \hat{H}_{NaLi} can be written as,

$$\begin{aligned} \hat{H}_{SMA} &= \hat{H}_N^{SMA} + \hat{H}_L^{SMA} + \hat{H}_{NN}^{SMA} + \hat{H}_{NL}^{SMA} + \hat{H}_{SCC}^{SMA} \\ &= \sum_s \left[\hat{E}_{s,1}(B_0)\hat{b}_{s,1}^\dagger\hat{b}_{s,1} + \hat{E}_{s,0}(B_0)\hat{b}_{s,0}^\dagger\hat{b}_{s,0} \right] \\ &+ \sum_s \left[X_{11}^s\hat{b}_{s,1}^\dagger\hat{b}_{s,1}^\dagger\hat{b}_{s,1}\hat{b}_{s,1} + X_{00}^s\hat{b}_{s,0}^\dagger\hat{b}_{s,0}^\dagger\hat{b}_{s,0}\hat{b}_{s,0} + 2X_{10}^s\hat{b}_{s,1}^\dagger\hat{b}_{s,0}^\dagger\hat{b}_{s,1}\hat{b}_{s,0} \right] \\ &+ X_{11}^{NL}\hat{b}_{N,1}^\dagger\hat{b}_{N,1}\hat{b}_{L,1}^\dagger\hat{b}_{L,1} + X_{00}^{NL}\hat{b}_{N,0}^\dagger\hat{b}_{N,0}\hat{b}_{L,0}^\dagger\hat{b}_{L,0} + X_{10}^{NL}\hat{b}_{N,1}^\dagger\hat{b}_{N,1}\hat{b}_{L,0}^\dagger\hat{b}_{L,0} \\ &+ X_{10}^{NL}\hat{b}_{N,0}^\dagger\hat{b}_{N,0}\hat{b}_{L,1}^\dagger\hat{b}_{L,1} + X^{SCC}\hat{b}_{N,0}^\dagger\hat{b}_{L,1}\hat{b}_{N,1}^\dagger\hat{b}_{L,0} + X^{SCC}\hat{b}_{N,1}^\dagger\hat{b}_{L,0}\hat{b}_{N,0}^\dagger\hat{b}_{L,1} \end{aligned} \quad (2.2)$$

where $\hat{E}_{s,\alpha}$ is given by

$$\hat{E}_{s,\alpha} = E_{s,\alpha}(B_0) + \int d^3(\mathbf{x})\Phi_{s,\alpha}^*(\mathbf{x}) \left[\frac{-\nabla_{\mathbf{x}}^2}{2m_s} + V_s(\mathbf{x}) \right] \Phi_{s,\alpha}(\mathbf{x}) \quad (2.3)$$

the reduced interaction constants are given by

$$X_{\alpha,\beta}^s = \frac{g_{\alpha,\beta}^s}{2} \int d^3(\mathbf{x})|\Phi_{s,\alpha}(\mathbf{x})|^2|\Phi_{s,\beta}(\mathbf{x})|^2 \quad (2.4)$$

$$X_{\alpha,\beta}^{NL} = g_{\alpha,\beta}^{NL} \int d^3(\mathbf{x}) \Phi_{N,1}^* \Phi_{L,1}^* \Phi_{N,0} \Phi_{L,0} \quad (2.5)$$

$$X_{\alpha,\beta}^{SCC} = g_{\alpha,\beta}^{SCC} \int d^3(\mathbf{x}) \Phi_{N,1}^* \Phi_{L,1}^* \Phi_{N,0} \Phi_{L,0} \quad (2.6)$$

To focus on the spin degrees of freedom, the Schwinger boson representation is used by introducing the spin operators,

$$\hat{L}_{z,s} = \frac{1}{2} \left(\hat{N}_{s,1} - \hat{N}_{s,0} \right) \quad (2.7)$$

where $\hat{N}_{s,\alpha} = \hat{b}_{s,\alpha}^\dagger \hat{b}_{s,\alpha}$.

$$\begin{aligned} \hat{L}_{+,s} &= \hat{b}_{s,1}^\dagger \hat{b}_{s,0} \\ \hat{L}_{-,s} &= \hat{b}_{s,0}^\dagger \hat{b}_{s,1} \end{aligned} \quad (2.8)$$

Using Equation 2.7 and 2.8, the Hamiltonian \hat{H}_{SMA} can be simplified to the following by dropping all the terms in the Hamiltonian which only contain number operators of conserved quantities,

$$\begin{aligned} \hat{H}_{SMA}^{spin} &= \left[(E_{N,1}(B_0) - E_{N,0}(B_0)) + \chi_N (\hat{N}_N - 1) + \frac{1}{2} \chi_{NL} \hat{N}_L \right] \hat{L}_{z,N} - \chi_N \hat{L}_{z,N}^2 \\ &+ \left[(E_{L,1}(B_0) - E_{L,0}(B_0)) + \chi_L (\hat{N}_L - 1) + \frac{1}{2} \chi_{NL} \hat{N}_N \right] \hat{L}_{z,L} - \chi_L \hat{L}_{z,L}^2 \\ &+ \chi_{NL} \hat{L}_{z,N} \hat{L}_{z,L} + \hat{H}_{SCC} \end{aligned} \quad (2.9)$$

where $\chi_s = X_{11}^s - X_{00}^s$, $\chi_{NL} = X_{11}^{NL} - X_{00}^{NL}$ and \hat{H}_{SCC} is given by

$$\hat{H}_{SCC} = X^{SCC} \left[\hat{b}_{L,1}^\dagger \hat{L}_{-,N} \hat{b}_{L,0} + \hat{b}_{L,0}^\dagger \hat{L}_{+,N} \hat{b}_{L,1} \right] \quad (2.10)$$

The Hamiltonian \hat{H}_{SMA}^{spin} can be simplified further by using the total magnetisation M which is defined as the following,

$$M = \hat{L}_{z,N} + \hat{L}_{z,L} \quad (2.11)$$

the total magnetisation M is a conserved quantity due to the spin-changing collisions. The spin-changing collisions allows the spin state of one specie to change while the spin state of the other specie to change accordingly to conserve the angular momentum. The final Hamiltonian of the building block can then be described using equation 2.12,

$$\frac{H_{BB}}{\hbar} = \chi \hat{L}_{z,N}^2 + \frac{\Delta}{2} (\hat{b}_{L,0}^\dagger \hat{b}_{L,0} - \hat{b}_{L,1}^\dagger \hat{b}_{L,1}) + \lambda (\hat{b}_{L,0}^\dagger \hat{L}_{-,N} \hat{b}_{L,1} + \hat{b}_{L,1}^\dagger \hat{L}_{+,N} \hat{b}_{L,0}) \quad (2.12)$$

where

$$\begin{aligned}
\lambda &= X^{SCC} \\
\chi &= -\chi_N - \chi_L = \chi_{NL} \\
\Delta &= (E_{L,1}(B_0) - E_{L,0}(B_0)) - (E_{N,1}(B_0) - E_{N,0}(B_0)) \\
&\quad + \chi_L(\hat{N}_L - 1) - \chi_N(\hat{N}_N - 1) + \frac{1}{2}\chi_{NL}(\hat{N}_N - \hat{N}_L) + 2M \left(-\chi_L - \frac{1}{2}\chi_{NL} \right)
\end{aligned} \tag{2.13}$$

The building block Hamiltonian provides a clear direction for the experiment as it includes all the necessary ingredients for a minimal gauge theory. With the experimental platform of the mixture, the gauge field is represented by the spin degrees of freedom in sodium, the matter field is represented by the spin degrees of freedom in lithium and the proper gauge invariant interaction is represented by the spin-changing collisions.

2.2 Experimental sequence

The model developed in the last section was then implemented using the NaLi platform. In this section, the experimental sequence used to realise the model is discussed in detail. A sketch of the experimental sequence can be found in Fig.2.3. To start the simulation, sodium and lithium atoms are cooled down to quantum degeneracy in a dipole trap with both species in the state of $|F = 1, m_F = 1\rangle$. After setting the magnetic field around 2 G, a superposition of sodium atoms in the state of $|F = 1, m_F = 1\rangle$ and $|F = 1, m_F = 0\rangle$ is created via a two-pulse transition while keeping the lithium atoms in the state of $|F = 1, m_F = 1\rangle$. The dynamics starts after the superposition is prepared and a period of evolution time of up to 100 ms is added before the detection. In order to detect different spin states, a Stern Gerlach separation pulse is applied to separate the states before imaging.

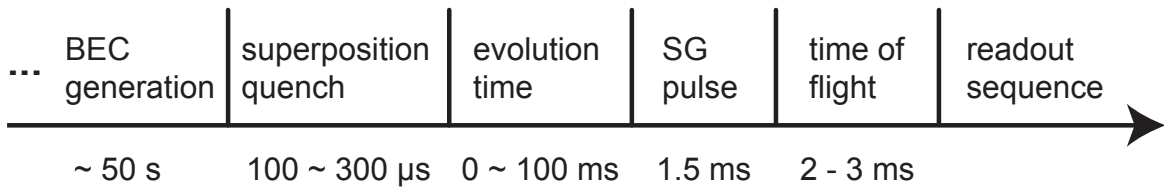


Figure 2.1. A sketch of a spin-changing collision sequence used in the experiment. Adapted from [47].

In order to be able to observe the spin-changing collisions, an external magnetic field of 1.96 to 2.14 G is applied during the superposition quench and the evolution

time stage. The energy splitting between the $|F = 1, m_F = 1\rangle$ and $|F = 1, m_F = 0\rangle$ state are degenerate for both sodium and lithium atoms in an external magnetic field of 1.96 to 2.14 G calculated using the Breit-Rabi formula. The degeneracy makes the spin-changing collisions more energetically favourable which enhances the signal for detection. However, a detuning of around 3 kHz is also required to keep the atoms out of the $|F = 1, m_F = -1\rangle$ state. The stability of the applied magnetic field affects the quench and the dynamics itself drastically, in order to both perform the quench and observe the dynamics consistently, a short-term stability below 1 mG is achieved using an activate field stabilisation scheme.

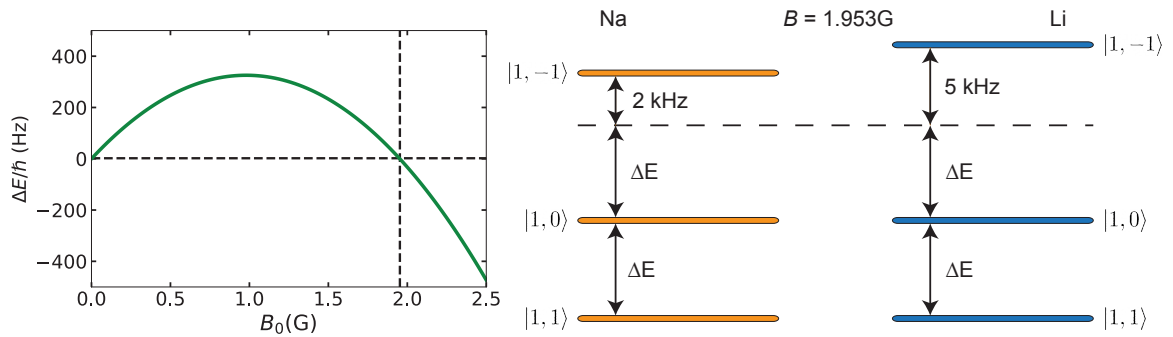


Figure 2.2. Top: the energy difference ΔE of $|1, 1\rangle$ and $|1, 0\rangle$ for two species against the external magnetic field B_0 calculated using the Breit-Rabi formula, the energy degeneracy being around 2 G. **Bottom:** the Zeeman splitting of sodium and lithium for $B_0 \approx 2$ G. Adapted from [47].

The superposition quench that transfers a proportion of atoms from the $|F = 1, m_F = 1\rangle$ state to the $|F = 1, m_F = 0\rangle$ state is a necessary step to start the dynamics of spin-changing collisions. The conservation of angular momentum requires atoms before and after such collisions to only occupy certain magnetic substates. In the situation where both species are only in the $|F = 1, m_F = 1\rangle$ state, spin-changing collision is not allowed as the angular momentum lost during one collision cannot be absorbed by any atoms in the system. Therefore at least one specie must be in a superposition of two different states of $|F = 1, m_F = 1\rangle$ and $|F = 1, m_F = 0\rangle$ to start the dynamics. In this case, sodium atoms are quenched into a superposition while keeping lithium in the $|F = 1, m_F = 1\rangle$ state. A clear signal of lithium in the $|F = 1, m_F = 0\rangle$ state can be observed if the spin-changing collisions occurred during the evolution time.

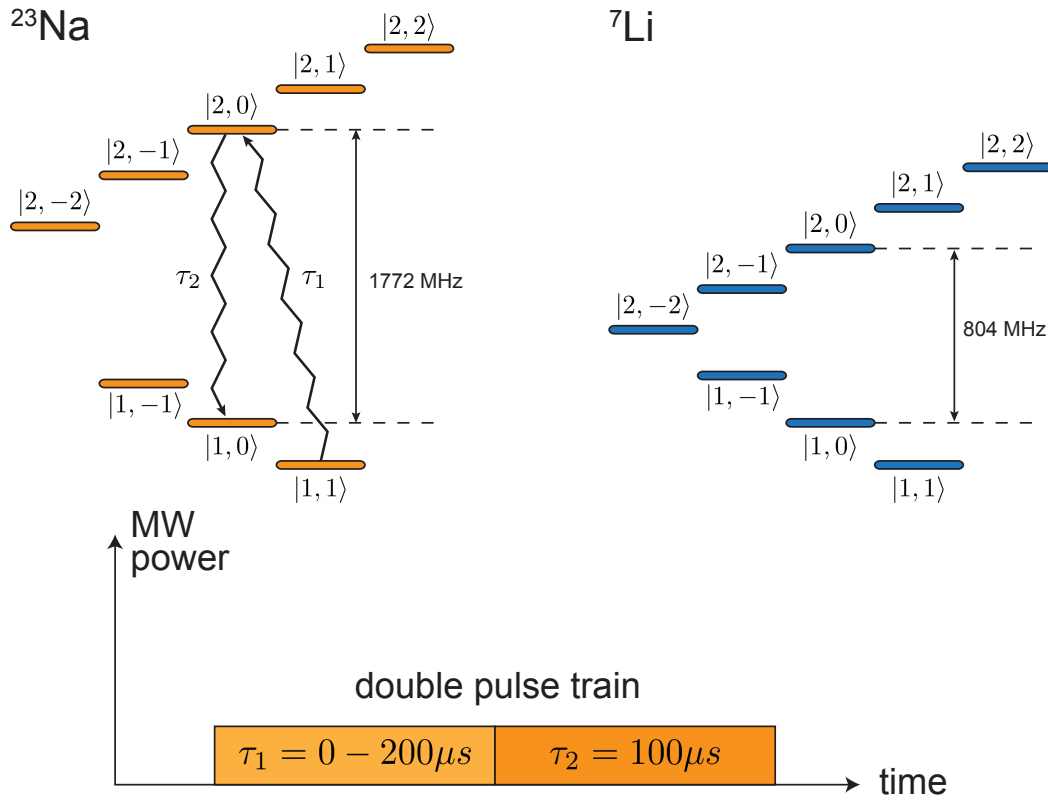


Figure 2.3. The two-pulse scheme used in the experiment to prepare the initial condition for the spin-changing collisions. By varying the duration of the first pulse τ_1 , the amount of sodium atoms transferred to $|F = 1, m_F = 0\rangle$ varies too. Adapted from [47].

Due to the fact that the energy difference between the two states for both species are the same, direct coupling between the two required states is not feasible as it leads to a population transfer in lithium atoms too. A two-pulse scheme is used to achieve the superposition in sodium without affecting lithium; the first pulse transfers atoms from $|F = 1, m_F = 1\rangle$ to $|F = 2, m_F = 0\rangle$ at around 1772 MHz is applied followed by the second pulse, transferring the atoms from $|F = 2, m_F = 0\rangle$ back to $|F = 1, m_F = 0\rangle$. The duration of the second pulse is fixed at $100 \mu\text{s}$ and the duration of the first pulse is used to determine the amount of the atoms transferred to the $|F = 1, m_F = 0\rangle$ state. The maximum total quench time is around $300 \mu\text{s}$ which is significantly shorter than the evolution time. Therefore, the quench can be considered as the initialisation of the spin-changing collisions. Fig.2.3 illustrates the two-pulse scheme used to initialise the spin-changing collisions.

To obtain the atomic signal after the evolution time, the population of each spin component from both species can be separated by using a Stern Gerlach pulse which has a strong magnetic field gradient. The atoms in different spin states ac-

celerate differently based on their magnetic moments. After the evolution phase, the trapping potential is switched off and a Stern Gerlach pulse is applied followed by imaging to determine the population in each hyperfine state. Absorption imaging is used to determine the number of atoms accurately in each state given the high density of the cloud. An example of an atomic signal for both sodium and lithium can be seen from Fig.2.4.

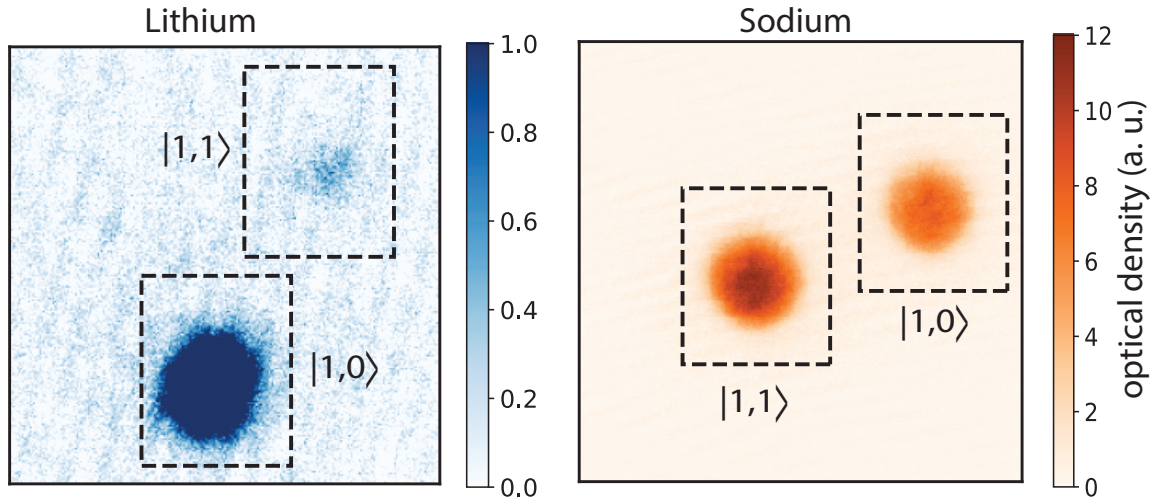


Figure 2.4. An example of atom signal obtained by absorption imaging together with the Stern Gerlach separation.

2.3 A summary of the experimental results

Using the experimental sequence described in the last section, several measurements were performed to characterise the building block model at the mean field level. Three parameters were scanned, the evolution time t_{evo} , the population ratio $\eta_0 = N_{Na,m_f=0}/N_{Na,total}$ prepared by the initial quench and the offset magnetic field B . The ratio of the lithium atoms in the state of $|F = 1, m_F = 0\rangle$ to the total population of the lithium atoms is the main observable used in the project.

2.3.1 A building block model: spin changing collisions at the mean field level

As shown in Section 3.1, the dynamics of the building block model can be described by the Hamiltonian defined in Equation 2.12,

$$\frac{H_{BB}}{\hbar} = \chi \hat{L}_{z,N}^2 + \frac{\Delta}{2} (\hat{b}_{L,0}^\dagger \hat{b}_{L,0} - \hat{b}_{L,1}^\dagger \hat{b}_{L,1}) + \lambda (\hat{b}_{L,0}^\dagger \hat{L}_{-,N} \hat{b}_{L,1} + \hat{b}_{L,1}^\dagger \hat{L}_{+,N} \hat{b}_{L,0}) \quad (2.14)$$

The mean field approximation is used in this model due to the large number of atoms for both sodium (3×10^6) and lithium (5×10^5), therefore the quantum fluctuations can be neglected at high occupation number [60]. By applying the Ehrenfest theorem, a set of equations of motion can be derived.

$$\begin{aligned}
\partial_t L_{x,N} &= -2\chi L_{z,N} L_{y,N} + 2\lambda L_{z,N} L_{y,L} \\
\partial_t L_{y,N} &= 2\chi L_{z,N} L_{x,N} - 2\lambda L_{z,N} L_{x,L} \\
\partial_t L_{z,N} &= 2\lambda L_{y,N} L_{x,L} - 2\lambda L_{x,N} L_{y,L} \\
\partial_t L_{x,L} &= -\Delta L_{y,L} + 2\lambda L_{z,L} L_{y,N} \\
\partial_t L_{y,L} &= \Delta L_{x,L} - 2\lambda L_{z,L} L_{x,N} \\
\partial_t L_{z,L} &= 2\lambda L_{y,L} L_{x,N} - 2\lambda L_{x,L} L_{y,N}
\end{aligned} \tag{2.15}$$

The set of equations can be solved numerically by using the parameters extracted from the fittings of the experimental data, with the initial conditions being chosen in line with the experimental measurements. The variable $N_p/N = N_{L,0}/N_L$ is used to understand the dynamics of the building block at the mean field level, which is also the observable measured in the experiment.

2.3.2 Evolution time

Firstly, in order to have a basic understanding of the dynamics, the evolution time t_{evo} is scanned between 0 and 100 ms with a fixed superposition in sodium at a given magnetic field. An example of such a scan over the parameter t_{evo} is shown in Fig.2.5. The number of atoms in $|F = 1, m_F = 1\rangle$ and $|F = 1, m_F = 0\rangle$ for both sodium and lithium is plotted as a function of the evolution time t_{evo} . Additionally, the ratio between the atoms in $|F = 1, m_F = 0\rangle$ and the total population is also plotted for each specie. A damped oscillation in the population of $|F = 1, m_F = 0\rangle$ can be observed with around 6 % maximum transfer. Whilst the same measurements are carried out for the sodium atoms, the effect of the spin-changing collisions cannot be observed in sodium due to a combination of underlying dynamics within the sodium atoms and technical issues which appeared in the experiment.

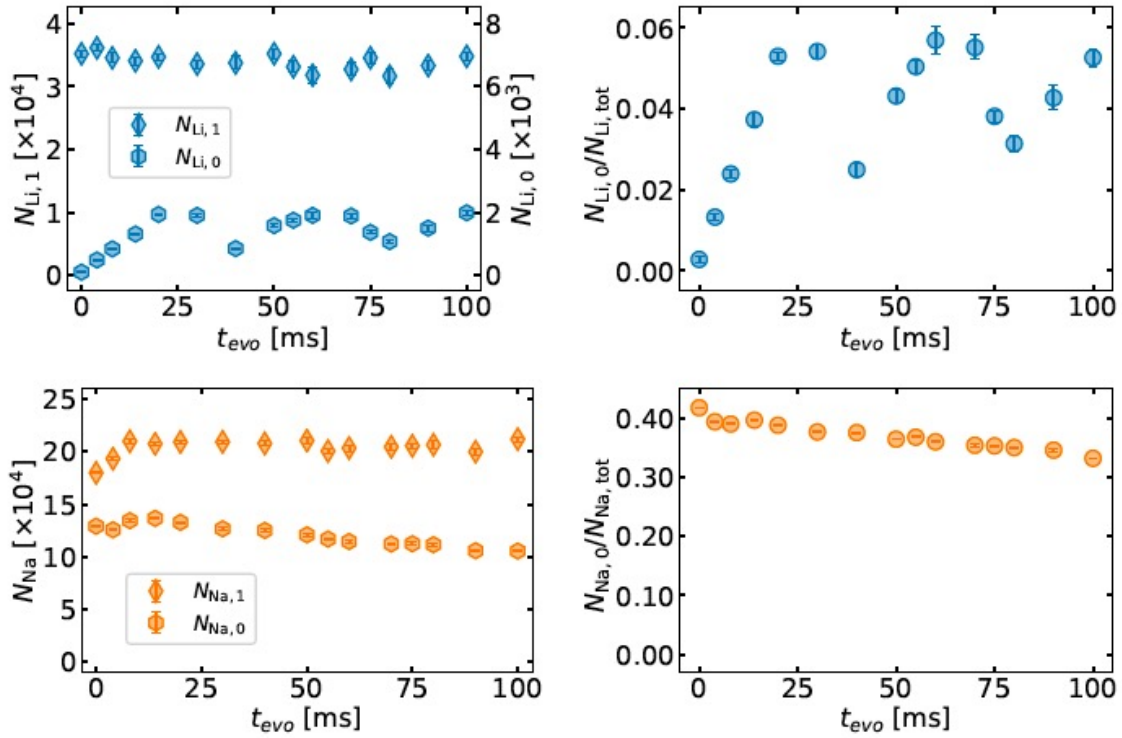


Figure 2.5. A dataset of the populations in the two hyperfine states for both sodium (**below**) and lithium (**above**) as a function of the evolution time t_{evo} . Adapted from [47].

2.3.3 Initial condition

To quantify the superposition used as the initial condition, the quantity $\eta_0 = N_{Na,0}/N_{Na,tot}$ is used. Similar measurements are carried out for the initial condition η_0 by varying the duration of the first pulse τ_1 in the two-pulse sequence, which leads to different amounts of sodium atoms transferred to $|F = 1, m_F = 0\rangle$. A fixed evolution time of 30 ms is used for the measurements as this is significantly shorter than the lifetime of the $|F = 1, m_F = 0\rangle$ state. Since the effects of the spin-changing collisions on the sodium atoms cannot be detected as mentioned above, the population ratio at 30 ms is assumed to be the same as the initial condition for sodium.

As can be seen from Fig.2.6, a clear resonance can be observed in the lithium atoms in $|F = 1, m_F = 0\rangle$ due to the spin-changing collisions. A sudden rise up to 8 % of the atoms in $|F = 1, m_F = 0\rangle$ can be seen when τ_1 is around 75 μs , corresponding to roughly 25 % of sodium atoms in $|F = 1, m_F = 0\rangle$ as the initial condition. A slow decay of the lithium population in the state of $|F = 1, m_F = 0\rangle$ as the transfer of the sodium atoms in $|F = 1, m_F = 0\rangle$ surpasses 25 % of the total sodium population.

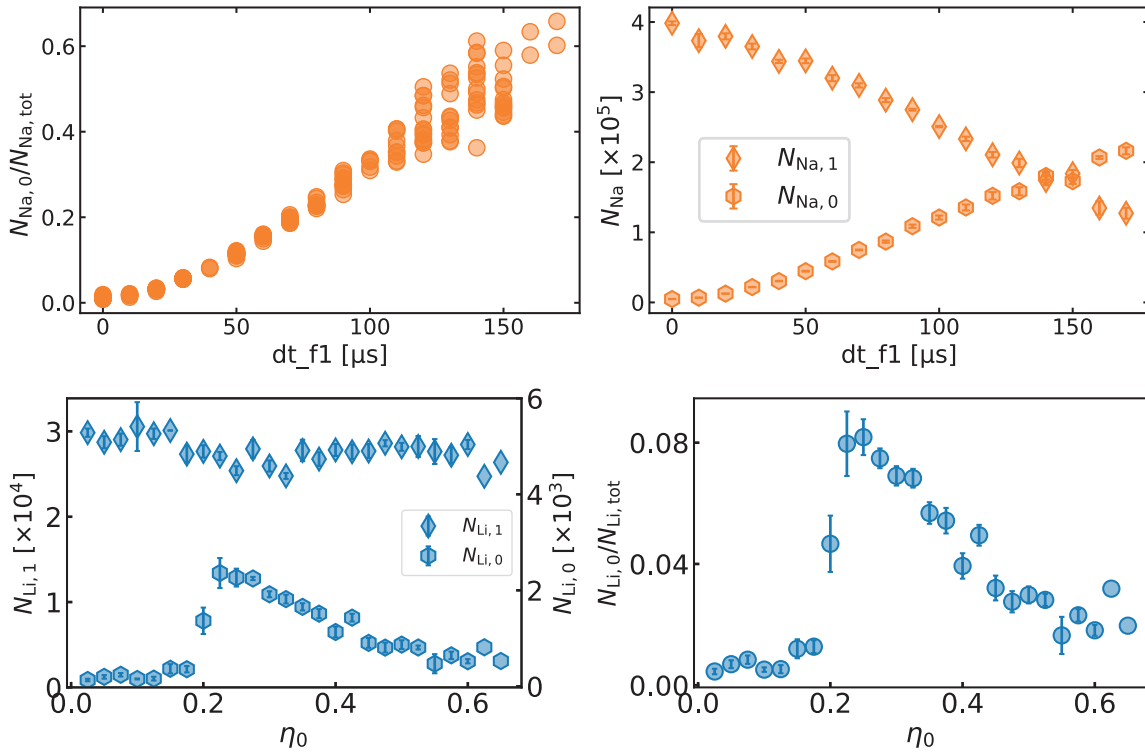


Figure 2.6. Top: the population of sodium atoms in $|F = 1, m_F = 0\rangle$ and $|F = 1, m_F = 1\rangle$ as a function of first pulse duration. **Bottom:** a dataset of the populations in the hyperfine state for lithium as a function of the initial condition of superposition in sodium. Adapted from [47].

2.3.4 Offset magnetic field

While both the initial condition and the evolution time give a good understanding of the building block model, the control over the magnetic field provides a more complete picture. As the magnetic field applied is varied, the measurements on the initial conditions are repeated.

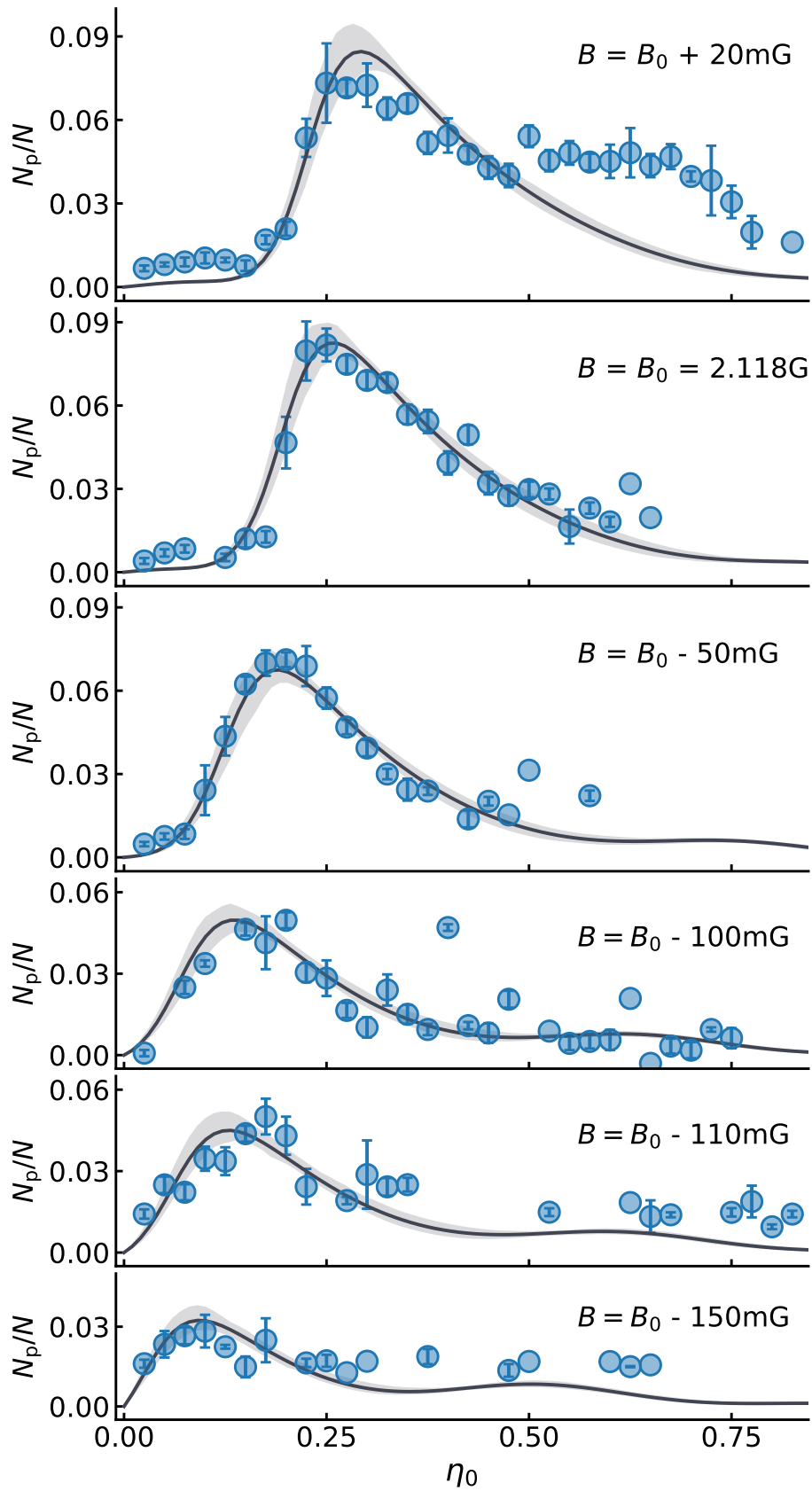


Figure 2.7. A dataset of the population of lithium as a function of the initial condition η_0 in the presence of various magnetic fields B . Adapted from [47].

The distinct feature of the resonance condition is still present at various magnetic fields B , however the resonance shifts to a lower superposition η_0 with a reduction in the height of the peak as the magnetic field decreases. For magnetic fields below 1.968 G, there is almost no such distinct feature that can be seen any more, as shown in Fig.2.7.

2.4 Drawbacks of the platform

While the dynamics of the building block predicted by the mean field level agrees relatively well with the experimental data as shown in the last section, there are still a few challenges that need to be understood and overcome experimentally.

2.4.1 Stability of BEC production

The challenge in producing Bose-Einstein condensates consistently on the platform remains one of the main obstacles to achieve the continuous running of the machine. The problem can be seen in the raw data taken for the building block project; a cut-off filter is needed to post select the raw data as shown in Fig.2.8. Especially in the case of lithium, where sympathetic cooling is used, the atom number fluctuates drastically in the condensate. Given the long cycling time of the experiment, around 60 s, a normal running day would usually result in 600 shots with 60 % fidelity. Statistical analysis requires large amounts of data, which is very challenging given a short amount of time.

The difficulty in producing Bose-Einstein condensates reliably can be analysed from both a hardware and software point of view. On the hardware side, the platform was not able to operate at night without human intervention, therefore the strong magnetic fields and the laser systems are switched off during night, as well as the ovens to recycle atoms. Daily drifts in the room temperature, magnetic fields and laser power can be observed when the machine is switched back on in the morning, and several hours are usually required to optimise the laser power and the experimental parameters such as the trap bottom of the magnetic trap. Regularly turning the lasers on and off causes both reductions in lifetime and jumps in the wavelength and power due to changes in the cavity temperature. On the software side, the experimental control system used in the platform crashes regularly alongside the other electronics such as the camera software, which leads to a long sequence of shots without atoms if not restarted. More seriously, sometimes the malfunctioning of the

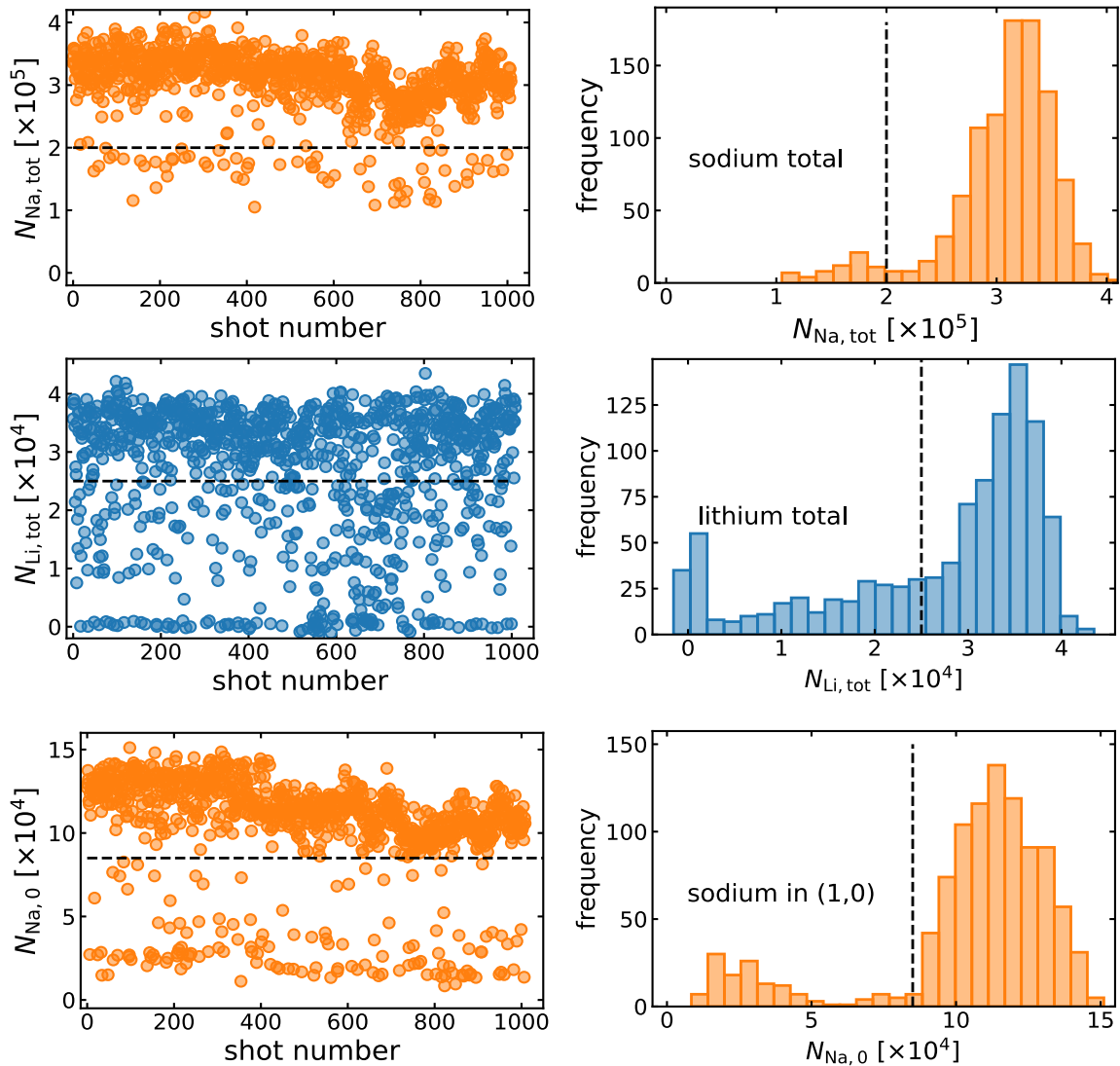


Figure 2.8. The difficulty in producing Bose-Einstein condensates for both species on the platform. Adapted from [47].

experimental control system causes the power supplies to remain at currents which could lead to detrimental effects such as the coils overheating.

To summarise, the combined effects from both the hardware and software result in a large inconsistency in BEC production on the platform. Most experiments require stable production of BECs as the starting point, therefore a stable platform is both necessary and advantageous for both quantum simulation and computation.

2.4.2 Spatial dynamics in sodium

During the quench phase of the experiment, spatial dynamics can be observed in sodium atoms with absorption imaging. Such an example can be found in Fig.2.9.

With a relatively large atom number, a ringing shape structure can be observed in the state of $|F = 1, m_F = 1\rangle$ with a compression in density for atoms in $|F = 1, m_F = 0\rangle$. In the regime of a large evolution time, breathing modes can be observed in sodium with frequencies on the order of the trapping frequencies.

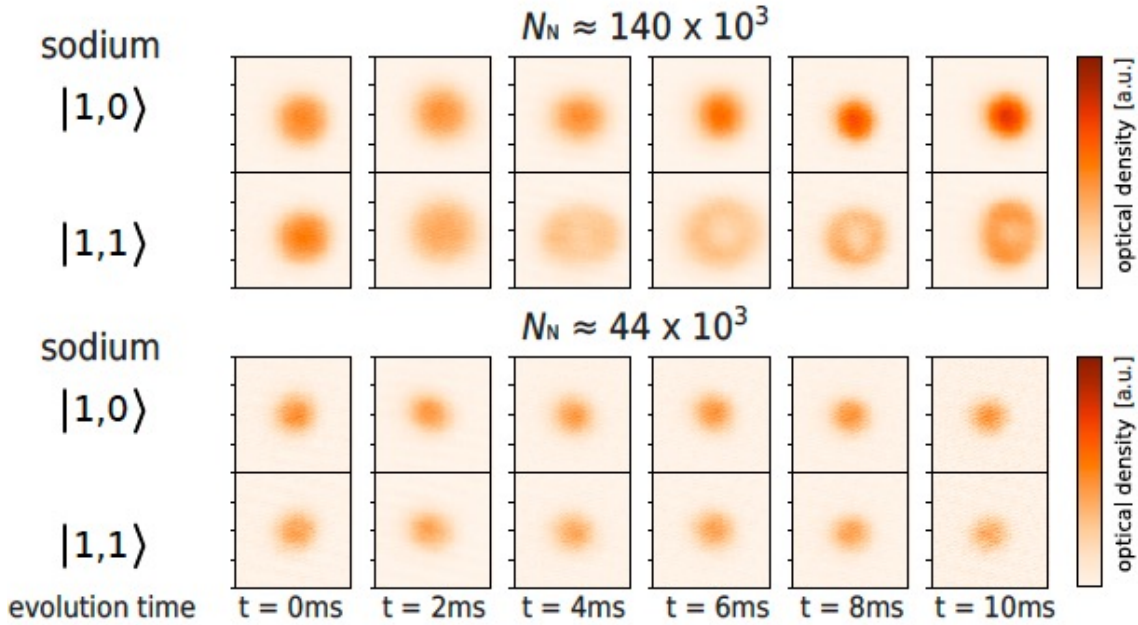


Figure 2.9. An example of the spatial dynamics of sodium involved in the quench phase of the experiment. Two sets of the measurements were carried out with different amount of atoms using a 50:50 superposition. Adapted from [47].

Two separate physical effects can be used to explain the dynamics observed, with the first one being potential separation and the second being phase separation [61–63]. The density distribution of an interacting BEC in its ground state is controlled by the external trapping potential and the interspecie interactions. The equilibrium state of a spin 1/2 Bose gas can be either miscible or immiscible depending on which one is more energetically favourable. The condition on miscibility is given as the following [63],

$$\sqrt{g_{11}g_{00}} < g_{10}^2 \quad (2.16)$$

where g_{ij} is the interaction strength between the state $|F = 1, m_F = i\rangle$ and $|F = 1, m_F = j\rangle$ for the respective specie. In the case of sodium, the condition is not fulfilled therefore the two states are immiscible.

The spatial dynamics can still occur even if the two states involved are miscible. When the system is in the ground state before the quench, the density profiles remain the same for both components after the quench. However, this density profile does not correspond to the ground state of the new system with two spin states, and

a redistribution of the density will happen depending on the magnitude of interaction strength. Given $g_{11} > g_{10}$ for sodium, the $|F = 1, m_F = 1\rangle$ state will sit at the edge of the potential with a lower density which causes the spatial dynamics.

Due to the lack of the ability to resolve the in-situ density profile of each component, no quantitative measurements can be done to study the dynamics, therefore the dynamics is not included specifically in the building block model; instead a decoherence term is used. In order to make the system cleaner and simpler, suppression of the dynamics is considered by tightening the confinement of atoms. Since the dynamics is the result of a competition between the trapping potential and the interactions between atoms, by increasing the trapping potential it can be ensured that the interactions between atoms are negligible. The use of optical lattices can be a relatively simple and controllable way to suppress the spatial dynamics.

2.5 Quantum computation using ultracold mixtures

Although the machine suffers from some drawbacks arising from both the hardware and software used, the idea of carrying out quantum computing and information processing with the platform is still promising [43]. As proposed by Valentin Kasper and others, the platform makes an ideal candidate for quantum computing. In this section, the focus is on the implementation of the scheme on the platform of the sodium-lithium mixture; the quantum error correction scheme presented in [43] is not discussed due to the difficulty of such experiments.

2.5.1 A theoretical model

A collective spin of one atomic specie with a controllable length confined in an optical tweezer or lattice acts as a fundamental unit of computing, a qudit. The other atomic specie forms a bath which is used to generate the entanglement between two distant qudits via the exchange of phononic excitations. The operations on a single collective spin in combination with their pairwise entanglement forms a universal gate set where the gate speed is much faster than the decoherence time of the platform. Combining all the conditions above, the scheme fulfils DiVincenzo's criteria for quantum computation [64].

To implement the scheme on the platform, lithium atoms are natural candidates for the qudits while sodium atoms can form a bath with phononic excitations. The detailed derivation of the Hamiltonian can be found in [43].

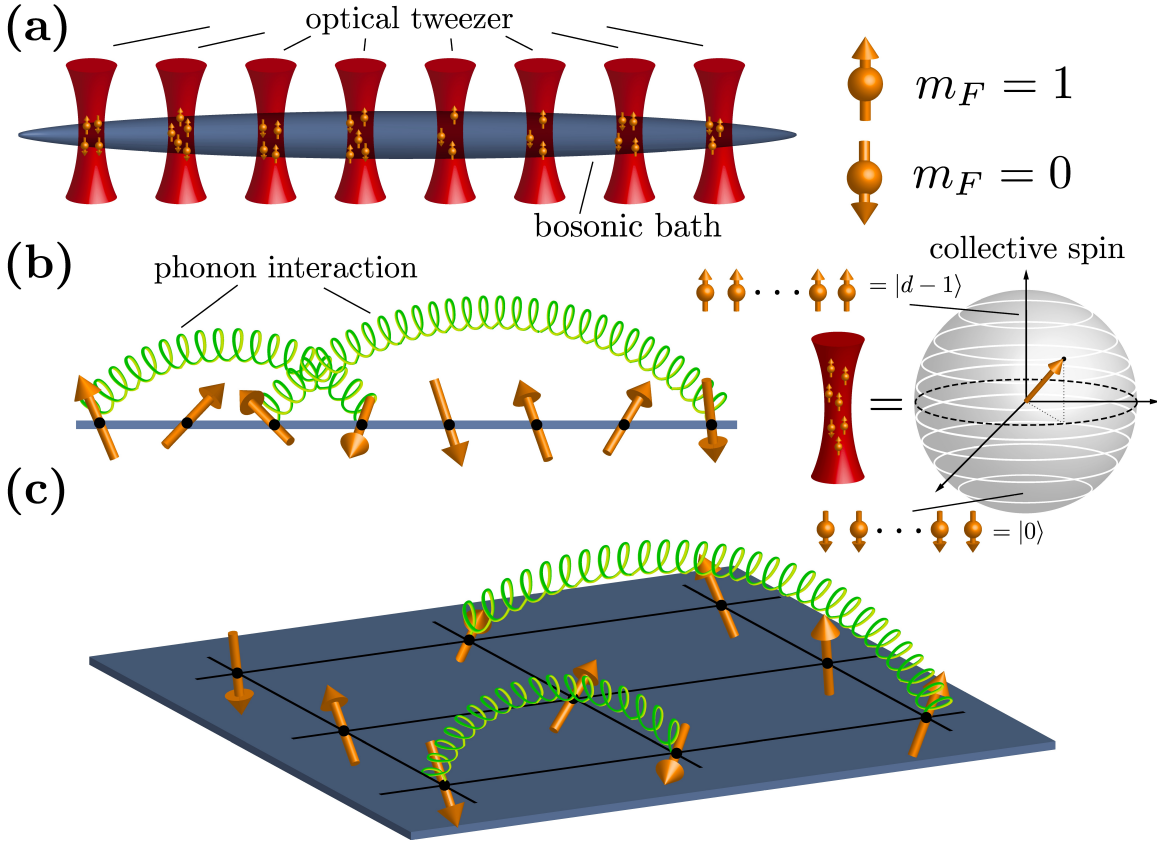


Figure 2.10. Quantum computing using ultracold mixtures. Taken from [43].

Starting with the single specie Hamiltonian \hat{H}_s defined in equation 1.2, with the trapping potential being a deep optical lattice where tunnelling is forbidden, the Hamiltonian of lithium atoms in an optical lattice is given as the following,

$$\hat{H}_A = \sum_{\mathbf{y}} \left[\chi(\mathbf{y}) \hat{L}_z^2(\mathbf{y}) + \Delta(\mathbf{y}) \hat{L}_z(\mathbf{y}) + \Omega(\mathbf{y}) \hat{L}_x(\mathbf{y}) \right]. \quad (2.17)$$

where the Schwinger representation for \hat{L}_z and \hat{L}_x in equation 2.7 and 2.8 is used and \mathbf{y} is the location of individual lattice site. The coupling constants are given below and the energy shift E_A^m can be calculated using equation 1.3.

$$\chi = \frac{1}{2} (\tilde{g}_A^{00} + \tilde{g}_A^{11} - 2\tilde{g}_A^{10}), \quad (2.18)$$

$$\Delta = \frac{1}{2} (N_A - 1) (\tilde{g}_A^{11} - \tilde{g}_A^{00}) + E_A^1 - E_A^0, \quad (2.19)$$

$$\tilde{g}_A^{mn} = g_A^{mn} \int_{\mathbf{x}} |\hat{\psi}_A(\mathbf{x} - \mathbf{y})|^4 \quad (2.20)$$

The first term indicates the interactions between the atoms, while the second term is the energy shift due to an external magnetic field and the third term is the Rabi coupling between the hyperfine states. The coupling constant χ can be switched off by distributing atoms in $|F = 1, m_F = -1\rangle$ and $|F = 1, m_F = 1\rangle$ instead of $|F = 1, m_F = 0\rangle$

and $|F = 1, m_F = 1\rangle$ as well as using Raman transitions [65]. The other two coupling constants can also be tuned via Raman transitions as demonstrated in platforms with ions [66]. The independent control over all the coupling constants on individual sites of an optical lattice can generate all unitary operations on a single collective spin for both qubits and qudits. A detailed discussion on the completeness of the unitary operations can be found in [43].

A phononic bath in 1D or 2D formed by sodium atoms confined in an optical dipole trap can be described using the Hamiltonian \hat{H}_B where only the purely phononic part is considered,

$$\hat{H}_B = \sum_{\mathbf{k}} \hbar\omega_{\mathbf{k}} \hat{b}_{\mathbf{k}}^\dagger \hat{b}_{\mathbf{k}}, \quad (2.21)$$

where $\hat{b}_{\mathbf{k}}$ is the annihilation operator of a phonon mode at wave number \mathbf{k} with component $k_i = \frac{\pi}{L}m_i$. Here, the transversal degrees of freedom are assumed to be frozen out for sufficiently low temperatures, and the density profile of the condensate is assumed to be homogeneous by using a box potential.

Finally, the interactions between the collective spins and the phononic bath can be realised using the contact interactions between sodium and lithium, with the interaction Hamiltonian being given by,

$$\hat{H}_{int} = \sum_{\mathbf{y}, \mathbf{k}} [\bar{g}_{\mathbf{k}}(\mathbf{y}) + \delta g_{\mathbf{k}}(\mathbf{y}) L_z(\mathbf{y})] (b_{\mathbf{k}} + \text{H.c.}), \quad (2.22)$$

where

$$\bar{g}_{\mathbf{k}}(\mathbf{y}) = L(\mathbf{y}) [\tilde{g}_{AB, \mathbf{k}}^0(\mathbf{y}) + \tilde{g}_{AB, \mathbf{k}}^1(\mathbf{y})], \quad (2.23)$$

$$\delta g_{\mathbf{k}}(\mathbf{y}) = \tilde{g}_{AB, \mathbf{k}}^1(\mathbf{y}) - \tilde{g}_{AB, \mathbf{k}}^0(\mathbf{y}). \quad (2.24)$$

where the first term corresponds to a constant polaronic shift and the second term is used to create entanglement between the spins [67, 68]. The speed of the entanglement gate is determined by the scattering length between two atomic species.

2.5.2 The experimental protocol

For state preparation, the collective spins can be prepared by creating superpositions of one atomic species in their hyperfine states in an optical lattice or tweezers. Post selections or Mott-insulator states can be used to fix the atom number in each site. A box potential in 1D or 2D can be created using optical dipole traps for the other atomic species as a phononic bath. A sophisticated microwave/RF system is

needed to implement different gates on the collective spins. For detection, fluorescence imaging is needed in the regime of a small atom number while homodyne detection can be used for large collective spins [69, 70].

State perpetration and readouts with a very high fidelity are vital for running gate-based quantum computers. However, there are still several experimental challenges to overcome in order to implement the proposed scheme on the platform. Preparing collective spins in optical lattices or tweezers is yet to be implemented on the machine. A stable magnetic field of the order of $100\ \mu\text{G}$ is desired during both reliable perpetration and coherent evolution of the states. High fidelity fluorescence imaging is yet to be realised on the platform which is also important for the reasons mentioned above. Additionally, a continuously running platform with a reliable state perpetration is a good starting point to implement the proposal.

3 Theoretical Background

In this chapter, the theory used behind the work of this thesis is presented. The first part starts with the basic interactions between a single atom and electromagnetic fields, the Zeeman effect due external magnetic fields and then discusses the two-level model for atoms. Important techniques such as Rabi and Ramsey spectroscopy for state manipulation of the Bloch sphere are also explained. The second part focuses on the theories behind systems with many atoms, which describes Bose-Einstein condensates.

3.1 Atom-light interaction

3.1.1 The interaction Hamiltonian

The general Hamiltonian of a charged particle in an electromagnetic field with the scalar potential ϕ and vector potential \mathbf{A} is given as the following

$$\hat{H} = \frac{1}{2m}(\hat{p} - q\mathbf{A})^2 + q\phi \quad (3.1)$$

In the case of hydrogen-like atoms, the Hamiltonian can be simplified to

$$\hat{H} = \frac{-i\hbar e}{m}\mathbf{A} \cdot \nabla \quad (3.2)$$

The vector potential \mathbf{A} can be expressed using the following equation for plane polarised electromagnetic waves,

$$\mathbf{A}(\mathbf{r}, \omega, t) = \hat{\epsilon}A_0(\omega)(e^{i[\mathbf{k}\cdot\mathbf{r}-\omega t]} + c.c) \quad (3.3)$$

where the matrix elements coupling the ground state $|g\rangle$ and the excited state $|e\rangle$ have the form $\langle e|e^{-i\mathbf{k}\cdot\mathbf{r}}\hat{\epsilon} \cdot \nabla|g\rangle$ and $\hat{\epsilon}$ is the polarisation unit vector.

For optical transitions where the wavelength of light is much larger than the size of the atom, the electric dipole approximation can be applied by only taking the first

term in the expansion series $e^{-i\mathbf{k}\cdot\mathbf{r}}$. As a result, the interaction Hamiltonian can be written as

$$\hat{H} = \hat{D} \cdot \mathbf{E} \quad (3.4)$$

where $\hat{D} = e \sum_i \hat{r}_i$ is the atomic dipole operator while the electric field can be written as $\mathbf{E} = \hat{\epsilon} \cos(\omega t)$.

3.1.2 Atoms in static magnetic fields

The angular momentum state of an atom in the absence of an external magnetic field is given by the hyperfine interaction,

$$\hat{H}_{hfs} = A\hat{I} \cdot \hat{J} \quad (3.5)$$

where A is the hyperfine splitting constant, \hat{I} is the nuclear spin operator and \hat{J} is the electronic angular momentum. The eigenstates $|F, m_F\rangle$ of the Hamiltonian can be described using the total angular momentum operator $\hat{F} = \hat{I} + \hat{J}$. The eigenvalues of the states are given as

$$E_{HFS}(F, m_f) = \frac{1}{2}[F(F+1) - I(I+1) - J(J+1)] \quad (3.6)$$

By applying an external magnetic field, the magnetic dipole moment of the atom couples the total angular momentum \hat{F} as well as the nuclear spin \hat{I} , which introduces an extra term in the Hamiltonian

$$\hat{H}_B = A\hat{I} \cdot \hat{J} + (g_I\mu_N\hat{I} + g_J\mu_B\hat{J}) \cdot \mathbf{B} \quad (3.7)$$

where μ_B and μ_N are the Bohr magneton and nuclear magneton respectively. For $J = 1/2$, corresponding to alkaline metal atoms in the ground state, an analytical expression can be obtained for the eigenvalues, which is known as the Breit-Rabi formula

$$E(F = I \pm \frac{1}{2}, m_F) = -\frac{\Delta_{hfs}}{2(2I+1)} - m_F g_I \mu_N |\mathbf{B}| \pm \frac{\Delta_{hfs}}{2} \sqrt{1 + \frac{4m_F}{2I+1}x + x^2} \quad (3.8)$$

where

$$x = \frac{(g_J\mu_B - g_I\mu_N)|\mathbf{B}|}{\Delta E_{hfs}} \quad (3.9)$$

The linear and quadratic Zeeman shift can be obtained by expanding the Breit-Rabi formula in equation 3.8 as a function of the magnetic field, and the energy of each m_F state can be written as the following

$$E^{m_F}(\mathbf{B}) = E_0 - p_m(\mathbf{B})m_F + q_m(\mathbf{B})m_F^2 \quad (3.10)$$

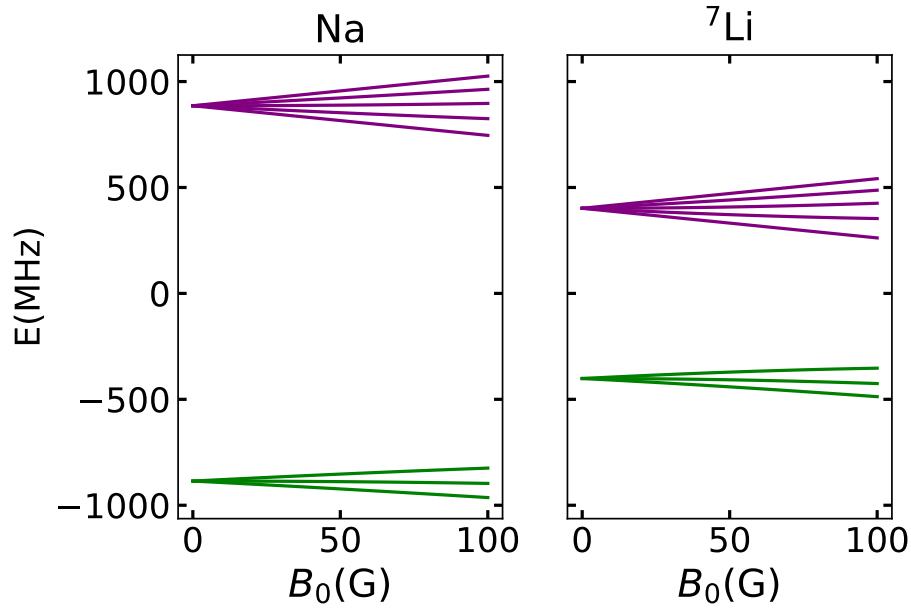


Figure 3.1. The hyperfine structure and Zeeman shift in external magnetic field for both Na and Li in $F = 1$ (green) and $F = 2$ (purple), according to the Breit-Rabi formula.

where for $F = 1$,

$$E_0 = -\frac{5\Delta E_{hfs}}{8} - \frac{(g_J - g_I)^2 \mu_B^2 |\mathbf{B}|^2}{4\Delta E_{hfs}} \quad (3.11)$$

$$p_m = \frac{g_J - 5g_I}{4} \mu_B |\mathbf{B}| \quad (3.12)$$

$$q_m = \frac{(g_J - g_I)^2}{16\Delta E_{hfs}} \mu_B^2 |\mathbf{B}|^2 \quad (3.13)$$

3.1.3 Two-level system

Consider an atom with the ground state $|g\rangle$ and the excited state $|e\rangle$ which can be coupled by an electric dipole transition of ω_0 . The atom interacts with a monochromatic radiation field of frequency ω .

The evolution of the system can be described by using the time-dependent Schrödinger equation

$$i\hbar \frac{\partial \psi(\mathbf{r}, t)}{\partial t} = \hat{H} \psi(\mathbf{r}, t) \quad (3.14)$$

The Hamiltonian of the interaction is the sum of the unperturbed atom Hamiltonian \hat{H}_0 and the electric dipole transition Hamiltonian $\hat{V} = \hat{d} \cdot \mathbf{E}$. The wavefunction of the system at time t is given by

$$\psi(\mathbf{r}, t) = c_g(t) |g\rangle + c_e(t) |e\rangle e^{-i\omega_0 t} \quad (3.15)$$

Substituting equation 3.15 into equation 3.14, two coupled-differential equations for the coefficients c_g and c_e can be derived,

$$i\hbar \frac{dc_g(t)}{dt} = c_e \langle g | \hat{d} \cdot \mathbf{E} | e \rangle e^{-i\omega_0 t} \quad (3.16)$$

$$i\hbar \frac{dc_e(t)}{dt} = c_g \langle e | \hat{d} \cdot \mathbf{E} | g \rangle e^{i\omega_0 t} \quad (3.17)$$

The electric field of the light can be written as $\mathbf{E} = E_0 \cos(k\mathbf{r} - \omega t)\hat{\epsilon}$ and $\Delta = \omega - \omega_0$ is the detuning of the light frequency relative to the atomic transition. The coupling constant Ω is defined as the Rabi frequency

$$\Omega = \frac{E_0}{\hbar} \langle e | \hat{d} \cdot \hat{\epsilon} | g \rangle \quad (3.18)$$

As can be seen from the equation 3.18, the Rabi frequency is determined by the intensity of the light, the atomic states involved and the polarisation through the dipole matrix element.

In order to solve the equations for the coefficients c_g and c_e , the rotating wave approximation is used. In the rotating wave approximation, the terms like $e^{-i(\omega+\omega_0)}$, which oscillate significantly faster than the frequency of driving field, can be neglected, as their time dependence averages out over the much slower timescale of the evolution of the coefficients c_g and c_e . The approximation is valid for weak driving fields such as $\Omega \ll \omega$. Under this approximation, the time evolution of the coefficients c_g and c_e can be expressed as follows

$$\begin{aligned} \frac{d^2 c_g}{dt^2} - i\Delta \frac{dc_g}{dt} + \frac{\Omega^2}{4} c_g &= 0 \\ \frac{d^2 c_e}{dt^2} + i\Delta \frac{dc_e}{dt} + \frac{\Omega^2}{4} c_e &= 0 \end{aligned} \quad (3.19)$$

3.1.4 Rabi oscillations

Assuming an atom is in the ground state $|g\rangle$ initially, then the equations 3.19 can be solved and the probability of the atom being in the excited state $|e\rangle$ is given by

$$|c_e(t)|^2 = \frac{\Omega^2}{\Omega'^2} \sin^2 \left(\frac{\Omega' t}{2} \right) \quad (3.20)$$

where $\Omega' = \sqrt{\Omega^2 + \Delta^2}$. In the case of $\Delta = 0$, a pulse of duration $T = \frac{\pi}{\Omega}$ transfers the atoms from the ground state to the excited state or vice versa, usually referred to as a " π -pulse". If the pulse duration is set to be $T = \frac{\pi}{2\Omega}$, the atom is transferred from the ground state to an equal linear superposition of the ground state and the excited state, and the pulse is referred as a " $\pi/2$ -pulse" accordingly.

3.1.5 Bloch sphere

The use of the Bloch sphere helps to visualise the evolution of the quantum states in two-level systems more intuitively. Any pure state $|\psi\rangle$ of a two-level system can be mapped as a vector known as the Bloch vector on the Bloch sphere. The north and south pole of the Bloch sphere represent the two basis states $|e\rangle \rightarrow (1, 0)^T$ and $|g\rangle \rightarrow (0, 1)^T$ of the system. Any pure state of the system can be represented by a vector on the Bloch sphere, known as the "Bloch vector".

$$|\theta, \phi\rangle = \cos \frac{\theta}{2} |e\rangle + e^{i\phi} \sin \frac{\theta}{2} |g\rangle \quad (3.21)$$

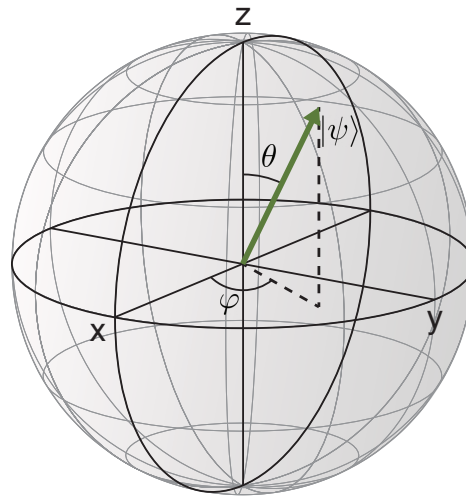


Figure 3.2. Any pure state $|\psi\rangle$ of a two-level system can be mapped on the Bloch sphere with two angles ϕ and θ .

Two examples of the Bloch vectors in a two-level system are shown in Fig 3.3. Similarly, the π -pulse and the $\pi/2$ -pulse can also be visualised as the rotations of the states on the Bloch sphere.

The Pauli matrices $\hat{\sigma}_x$, $\hat{\sigma}_y$ and $\hat{\sigma}_z$ form a set of bases of the Hilbert space and the two basis states $|e\rangle$ and $|g\rangle$ are the eigenstates of the operator \hat{R}_z . The rotation operators around different axes can be generated using the set of Pauli matrices. Rotations can be realised using external oscillating electromagnetic fields with controlled-phase. The full control over the states in two-level systems can be used for engineering complicated states or gates for quantum information processing.

$$\hat{\sigma}_x = \begin{pmatrix} 0 & -1 \\ 1 & 0 \end{pmatrix} \quad \hat{\sigma}_y = \begin{pmatrix} 0 & -i \\ i & 0 \end{pmatrix} \quad \hat{\sigma}_z = \begin{pmatrix} 1 & 0 \\ 0 & -1 \end{pmatrix} \quad (3.22)$$

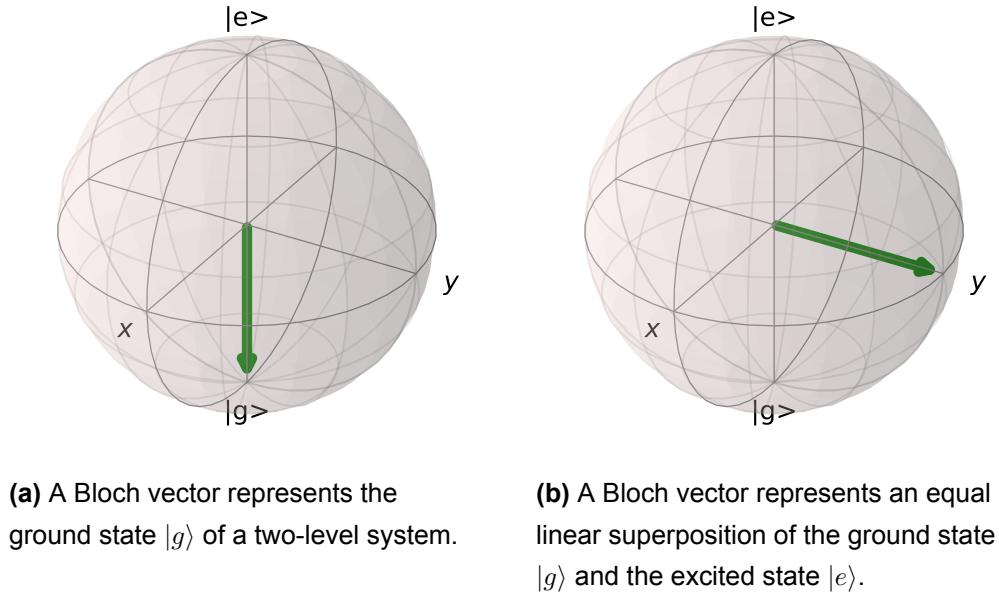


Figure 3.3. The Bloch vectors used to represent different quantum states of a two-level system.

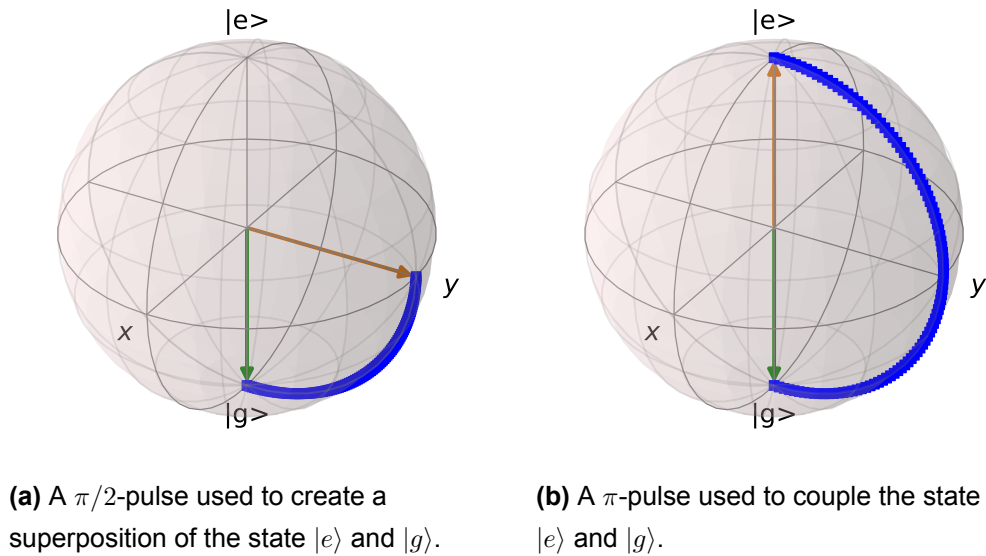


Figure 3.4. The rotations around the x-axis of the Bloch sphere.

Another set of operators which are particularly useful in describing coupled systems are the ladder operators $\hat{\sigma}_{\pm}$,

$$\hat{\sigma}_+ = \frac{1}{2}(\hat{\sigma}_x + i\hat{\sigma}_y) \quad (3.23)$$

$$\hat{\sigma}_- = \frac{1}{2}(\hat{\sigma}_x - i\hat{\sigma}_y) \quad (3.24)$$

where the commutation relations $[\hat{\sigma}_+, \hat{\sigma}_-] = 2\hat{\sigma}_z$ and $[\hat{\sigma}_z, \hat{\sigma}_{\pm}] = \pm\hat{\sigma}_{\pm}$ are followed.

Experimentally, Rabi spectroscopy is used to accurately determine the transi-

tion frequency between the ground state and the excited state of the system. The Hamiltonian of the system is given as

$$\hat{H}_{Rabi} = \frac{\hbar\Delta}{2}\hat{\sigma}_z + \frac{\hbar\Omega}{2}(\sin(\phi)\hat{\sigma}_x + \cos(\phi)\hat{\sigma}_y) \quad (3.25)$$

where the first term corresponds to the Larmor precession of the state with the frequency equal to the detuning Δ without the external electromagnetic field, and the second term introduces Rabi oscillations between the two states of the system with a Rabi frequency of Ω . The rotation axis can be controlled using the phase of the field ϕ . By changing the interaction time with the external electromagnetic field, the probability of the system being in one of the two states can be used to determine the detuning Δ and therefore the transition frequency. However, factors such as the inhomogeneity of the external electromagnetic field affect the accuracy of this method.

3.1.6 Ramsey spectroscopy

To measure the transition frequencies more accurately, the scheme developed by Ramsey splits the one π -pulse used in the Rabi scheme into two $\pi/2$ -pulses with a free evolution time Δt_{evo} in between the two pulses. As shown in Fig. 3.5, the first $\pi/2$ -pulse rotates the initial state onto the equator of the Bloch sphere, then the state evolves along the equator during the evolution time Δt_{evo} , and the second $\pi/2$ -pulse is given to bring the state to the another pole of the Bloch sphere. The advantage of using two short pulses instead of a long pulse is to reduce the effects from the inhomogeneities and systematic shifts.

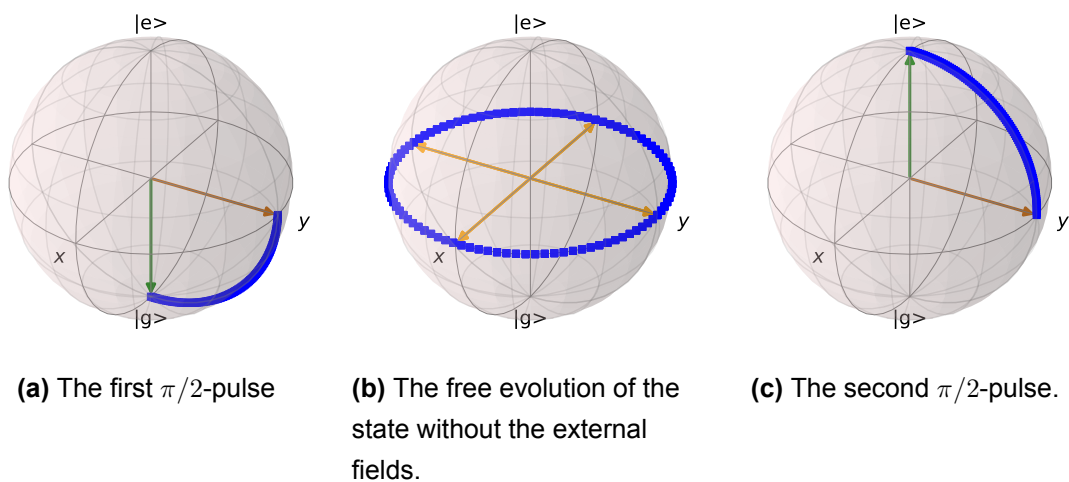


Figure 3.5. A sequence used for Ramsey spectroscopy.

As shown in Fig 3.5, the first $\pi/2$ -pulse rotates the initial state onto the equator of the Bloch sphere, then the state evolves along the equator during the evolution time Δt_{evo} , and the second $\pi/2$ -pulse is given to bring the state to the another pole of the Bloch sphere. Before the first $\pi/2$ -pulse is given, the phase ϕ between the electromagnetic field and the system is undefined. The first $\pi/2$ -pulse sets the phase to 0. A phase of $\phi = \Delta \times T_{evo}$ is naturally accumulated during the free evolution time, then the phase ϕ is measured by using the second $\pi/2$ -pulse which brings the system to the excited state. As a result, the probability of finding the system in the excited state is given as the

$$P(\phi) = \frac{1 + \sin(\phi)}{2} = \cos^2\left(\frac{\phi}{2}\right) \quad (3.26)$$

where $\phi = \Delta \times T_{evo}$.

3.1.7 Dressed states

By introducing two new coefficients $c'_e = c_e e^{i\Delta t}$ and $c'_g = c_g$, the equations of motion of the two-level system can be written as

$$i\hbar \frac{dc'_g(t)}{dt} = c'_e \frac{\hbar\Omega}{2} \quad (3.27)$$

$$i\hbar \frac{dc'_e(t)}{dt} = c'_g \frac{\hbar\Omega}{2} - c'_e \hbar\Delta \quad (3.28)$$

The Hamiltonian of the system can be written as in equation 3.29

$$\hat{H} = \frac{\hbar}{2} \begin{pmatrix} 0 & \Omega \\ \Omega & -2\Delta \end{pmatrix} \quad (3.29)$$

The two eigenstates $|g'\rangle$ and $|e'\rangle$ with corresponding eigenvalues E_g and E_e can be obtained as follows

$$|e'\rangle = \cos\theta |g\rangle - \sin\theta |e\rangle \quad E_e = \frac{\hbar}{2} \left(-\Delta - \sqrt{\Omega^2 + \Delta^2} \right) \quad (3.30)$$

$$|g'\rangle = \sin\theta |g\rangle - \cos\theta |e\rangle \quad E_g = \frac{\hbar}{2} \left(-\Delta + \sqrt{\Omega^2 + \Delta^2} \right) \quad (3.31)$$

In the case of $\Omega \ll \Delta$, a shift in energy $\Delta E = \frac{\hbar\Omega^2}{4\Delta}$ of each state can be seen by expanding the square root terms. The energy of the ground and the excited state shift in opposite direction. This shift is known as the AC Stark shift which is commonly used to trap and manipulate atoms. The two eigenstates are known as the dressed states which are coherent superpositions of the two bare states $|e\rangle$ and $|g\rangle$.

3.1.8 Rapid adiabatic passage

Although transferring population from one state to another state can be implemented using a π -pulse with the resonant frequency, there are still factors that limit the transfer efficiency. The main factors are unstable frequencies, inconsistent timing, unstable power and unstable external magnetic fields. All these factors contribute to the failure of an incomplete transfer, and the remaining atoms in the undesired state can lead to losses in the trap or other unwanted dynamics. One primary example would be the remaining sodium atoms in $|F = 2, m_F = 2\rangle$ that cause losses in the number of lithium atoms in the dipole trap.

As a result, a more robust scheme to transfer atoms is needed. The rapid adiabatic passage uses a dressed state to transfer atoms from one state to another adiabatically as it is typically used in a two-level system [71]. A microwave (RF) pulse sweeps in frequency starting with a large detuning Δ across the resonance, and the atoms in the initial states are projected completely onto the dress state, evolving with the dress state as the detuning changes. When the pulse is switched off at the other side of the resonance, the atoms in the dress state will get transferred back to the final state, therefore achieving an almost complete transfer.

The transfer efficiency is determined by the rate of the sweep, too fast of a sweep causes atoms to tunnel adiabatically into unwanted states. The Landau-Zener formula is used to describe the probability of such tunnelling,

$$P = e^{-\frac{2\pi\Omega^2}{\alpha}} \quad (3.32)$$

where α is the sweeping speed and Ω is the resonant Rabi frequency for the desired transition. A strong Rabi coupling between the states is ideal for more reliable transfers. Both sweeping in frequency at a constant speed and sweeping the magnetic field at a constant speed can be used to achieve the rapid adiabatic passage. However, the first option is usually used in the experiment as it is easier to implement on the platform.

3.2 Quantum degenerate gases

The Heisenberg uncertainty principle gives a relation between the uncertainty in position Δx and momentum Δp ,

$$\Delta x \Delta p \geq \frac{\hbar}{2} \quad (3.33)$$

as the atoms lose energy during the process of cooling, the model of wave packets is a better description with a de Broglie wavelength,

$$\lambda_{db} = \sqrt{\frac{2\pi\hbar^2}{mk_B T}} \quad (3.34)$$

where m is the mass of the atom and T is the temperature. The number of particles contained in a volume of λ_{db}^3 is defined as the phase-space density,

$$\rho = n_0 \lambda_{db}^3 \quad (3.35)$$

with n_0 being the peak density of the sample. In the regime of $\rho = 1$, the atoms are so cold such that the individual wavefunction of each atom starts to overlap. At a critical temperature T_c , the wavefunctions collapse into the lowest energy quantum state forming a Bose-Einstein condensate.

The occupation number of an atomic state i with energy ϵ_i of an ideal Bose gas is given by,

$$N_i = \frac{1}{e^{(\epsilon_i - \mu)/k_B T} - 1} \quad (3.36)$$

where μ is the chemical potential governed by the total amount of atoms. As the temperature decreases, the total atom number is divided into two parts in order to prevent from diverging, the atom number in the ground state N_0 and the atom number in all other states N_{rest} . By using Equation 3.36, total number of atoms can be expressed as

$$N = N_0 + N_{rest} = N_0 + \sum_{i=1}^{\infty} \frac{1}{e^{(\epsilon_i - \mu)/k_B T} - 1} \quad (3.37)$$

To conserve the atom number, the chemical potential μ needs to increase as the temperature goes down. At a certain temperature T_c , N_0 is much larger than N_{rest} . If the temperature keeps dropping, all the atoms will be in the ground state eventually and a pure Bose-Einstein condensate is formed with no thermal component present.

3.2.1 A non-interacting BEC in a harmonic trap

All the calculations carried out in this section are under the approximation there is no interaction between atoms within the BEC. However, the corrections needed to include these interactions are on the order of a few percent [72].

The conservative potential $U(\mathbf{r})$ used in this work can be approximated as a harmonic potential,

$$U(\mathbf{r}) = \frac{1}{2}m(\omega_x^2 x^2 + \omega_y^2 y^2 + \omega_z^2 z^2) \quad (3.38)$$

The condition to form a Bose-Einstein condensation in such a trap can be calculated [73] with the critical temperature T_c given by

$$T_c = \frac{\hbar\omega_0}{k_B} \left(\frac{N}{1.202} \right)^{\frac{1}{3}} \quad (3.39)$$

with N being the atom number and the mean trapping frequency $\omega_0 = (\omega_x\omega_y\omega_z)^{\frac{1}{3}}$. The peak atomic density is given by the number of atoms divided by the effective volume V_E ,

$$n_0 = \frac{N}{V_E} = N\omega_0^3 \left(\frac{m}{2\pi k_B T} \right)^{\frac{3}{2}} \quad (3.40)$$

where the effective volume is $V_E = \int e^{\left(\frac{-U(\mathbf{r})}{k_B T}\right)} d^3\mathbf{r}$. The condensate fraction as a function of the temperature can be defined as the ratio between the population in the ground state and the total population,

$$\frac{N_0}{N} = 1 - \left(\frac{T}{T_c} \right)^3 \quad (3.41)$$

The BEC behaves like an ideal gas, without the interactions, as all the atoms are in the ground state of the harmonic potential $U_{\mathbf{r}}$. The ground state wavefunction of a three-dimensional harmonic trap is given by

$$\phi_0 = \left(\frac{m\omega_0}{\pi\hbar} \right)^{\frac{3}{4}} e^{-\frac{m}{2\hbar}(\omega_x x^2 + \omega_y y^2 + \omega_z z^2)} \quad (3.42)$$

The density distribution of the ground state can be calculated using $n(\mathbf{r}) = N|\phi_0(\mathbf{r})|^2$ with a Gaussian profile and scales linearly with the atom number N . However, the size of the BEC is determined by the harmonic oscillator length a_{ho}

$$a_{ho} = \sqrt{\frac{\hbar}{m\omega_0}} \quad (3.43)$$

a_{ho} is also the average width of the Gaussian in the ground state wavefunction ϕ_0 . The individual width of the condensate $\sigma_i = \sqrt{\frac{\hbar}{m\omega_i}}$ in each direction can then be used to determine the spread in momentum space in each direction via the Heisenberg uncertainty principle,

$$\sigma_{p,i} = \frac{\hbar}{\sigma_i} = \sqrt{\hbar m \omega_i} \quad (3.44)$$

Finally, the average release energy for an ideal BEC can be calculated using $E_{rel} = \frac{p^2}{2m}$,

$$E_{rel} = \frac{1}{2}\hbar(\omega_x + \omega_y + \omega_z) \quad (3.45)$$

which is independent of the atom number N .

3.2.2 Bogoliubov approximation and Gross-Pitaevskii Equation

For interacting atoms in a BEC, a many-body Hamiltonian for N particles in an external potential can be used to calculate the properties of the BEC. However, this method is not feasible for a large number of atoms. A mean field description for dilute Bose gas was developed by Bogoliubov to solve this issue [74].

$$\hat{\Psi}(\mathbf{r}, t) = \hat{\Psi}'(\mathbf{r}, t) + \Phi(\mathbf{r}, t) \quad (3.46)$$

where the field operator $\hat{\Psi}(\mathbf{r}, t)$ is split into the expectation value $\Phi(\mathbf{r}, t)$ of the field operator and a first order perturbation $\hat{\Psi}'(\mathbf{r}, t)$. The expectation value is also known as the condensate wavefunction due to the fact that the density distribution of the BEC is given by $n(\mathbf{r}, t) = |\Phi(\mathbf{r}, t)|^2$.

As binary collisions are the dominating interactions between the atoms in a cold dilute gas, the condition where the approximation holds is given by $\langle n \rangle |a|^3 \ll 1$ with $\langle n \rangle$ being the mean atomic density and a being the s-wave scattering length. Gross and Pitaevskii then replaced the interaction potential between the particles with an effective interaction potential,

$$V(\mathbf{r} - \mathbf{r}') = g\delta(\mathbf{r} - \mathbf{r}') \quad (3.47)$$

where $g = \frac{4\pi\hbar^2 a}{m}$.

In the case of $T \ll T_c$, the first order perturbation $\hat{\Psi}'(\mathbf{r}, t)$ can be dropped and $\hat{\Psi}(\mathbf{r}, t)$ can be swapped by $\Phi(\mathbf{r}, t)$. Plugging in $\psi(\mathbf{r}, t)e^{-\frac{i\mu t}{\hbar}}$ for Φ ,

$$\left[-\frac{\hbar^2 \nabla^2}{2m} + V(\mathbf{r}) + g|\psi(\mathbf{r})|^2 \right] \psi(\mathbf{r}) = \mu\psi(\mathbf{r}) \quad (3.48)$$

which is a time-independent Gross-Pitaevskii equation (GPE). The equation has the form of a non-linear Schrödinger equation due to the interaction term $|\psi(\mathbf{r})|^2$, and when the interaction is set to be zero ($g = 0$), the GPE is reduced to the usual Schrödinger equation.

When the system is in the ground state, the energy is only dependent on the density and can be expressed in the form of [75]

$$E(n) = \int d\mathbf{r} \left[\frac{\hbar^2}{2m} |\nabla \sqrt{n}|^2 + nV(\mathbf{r}) + \frac{gn^2}{2} \right] = E_k + E_H + E_{int} \quad (3.49)$$

The quantum kinetic energy E_k is derived from the uncertainty principle, the second term E_H is the potential energy of the system and the last term E_{int} comes from the

interactions between particles and is referred to as the mean field energy. The chemical potential μ can be expressed in terms of E_k , E_H and E_{int}

$$\mu = \frac{E_K + E_h + 2E_{int}}{N} \quad (3.50)$$

Summing over the three directions gives

$$2E_k - 2E_h + 3E_{int} = 0 \quad (3.51)$$

3.2.3 Thomas-Fermi approximation

In the mean field regime, the interactions between atoms can be well described using the energy E_{int} which only depends on the density of the condensation and the s-wave scattering length. To understand the effect from the interactions, the ratio between E_{int} and E_k is used [75]

$$\frac{E_{int}}{E_k} = \frac{N|a|}{a_{ho}} \quad (3.52)$$

With a BEC of sufficiently large atom number N , the ratio between the two energy terms is much larger than 1. Then, the kinetic energy term E_k can be neglected, and so the ground state energy of the system can be obtained. Such an assumption is called the Thomas-Fermi approximation. Using $|\psi|^2 = n(\mathbf{r})$, the density profile can be obtained from equation 3.48

$$n(\mathbf{r}) = \begin{cases} \frac{\mu - V(\mathbf{r})}{g}, & \text{for } \mu - V(\mathbf{r}) > 0 \\ 0, & \text{otherwise} \end{cases} \quad (3.53)$$

The density profile reflects the shape of the potential, for atoms in a harmonic trap the density profile is an inverted parabola. In the case of $\mu = V(\mathbf{r})$, the density profile vanishes at the Thomas Fermi radii

$$R_{TFi} = \sqrt{\frac{2\mu}{m\omega_i^2}} = a_{ho} \frac{\omega_{ho}}{\omega_i} \left(\frac{15Na}{a_{ho}} \right)^{\frac{1}{5}} \quad (3.54)$$

where ω_i is the trapping frequency in the i-direction. The peak density in the trap centre can also be calculated by setting $V(\mathbf{r}) = 0$,

$$n_0 = \frac{\mu}{g} = \frac{\mu m}{4\pi\hbar^2 a} \quad (3.55)$$

Normalising the density profile provides a relation between the chemical potential and the atom number,

$$\mu = \frac{\hbar\omega_0}{2} \left(\frac{15Na}{a_{ho}} \right) \quad (3.56)$$

By dropping the kinetic energy term, the release energy only depends on the interaction energy E_{int} . The average energy and the release energy in the Thomas-Fermi approximation can be obtained by integrating over the density profile in Equation 3.49,

$$E = \frac{5}{7}\mu \quad (3.57)$$

$$E_{rel} = \frac{2}{7}\mu \quad (3.58)$$

The dependence of the release energy on both the scattering length and the atom number has been demonstrated experimentally [76–78].

3.2.4 Tunable interactions

The interactions within the BEC can be controlled via Feshbach resonances as mentioned earlier by changing an external magnetic field. When the change in the scattering length is adiabatic, the density distribution evolves, therefore equations 3.57 and 3.58 still hold.

On the other hand, a sudden change in a magnetic field changes the scattering length from a to a' non-adiabatically. There is not enough time for the density profile to reach equilibrium and is still determined by the scattering length a . As a result, the release energy per particle is changed to the following,

$$E_{rel}(a') = \frac{2}{7}n_0(a)g(a') = \frac{2}{7}\mu(a)\frac{a'}{a} \quad (3.59)$$

which scales linearly with a' [78].

- In the case of $a > 0$, the interactions between the atoms are repulsive which produces a stable BEC with a strong mean-field expansion.
- In the case of $a < 0$, the interactions between the atoms are attractive which leads to a higher density in the centre of the trap to reduce the interaction energy. The attractive forces can be compensated with the quantum kinetic energy. However due to the different scaling factors between the two, stable BECs can only be formed with the atom number below a critical value $N_{critical} = k^* \frac{a_{ho}}{|a|}$, where k^* is the stability constant determined by the ratio of the trapping frequencies [79].
- In the case of $a = 0$, there is no interaction between the atoms in a BEC with minimal internal energy.

3.2.5 Expansion of condensates

When the trapping potential is switched off, the mean field energy of a condensate is converted into the kinetic energy in an anisotropic way. The acceleration due to the internal energy is proportional to the density of the mean field energy and therefore the density gradient [75]. For a cigar shape condensate trapped in an anisotropic potential in which the trapping frequency in the radial direction is larger than the trapping frequency in the axial direction $\omega_\rho > \omega_z$, the aspect ratio of a freely expanding condensate is inverted and acts as an important signature of BECs [80].

The Thomas-Fermi radii in the radial (ρ) and axial (z) directions of a condensate during the free expansion is given by,

$$R_{\rho,z}(t) = \lambda_{\rho,z}(t)R_{\rho,z}(0) \quad (3.60)$$

where $R_{\rho,z}(0)$ is the Thomas-Fermi radii in the trap and $\lambda_{\rho,z}$ is the scaling parameter. In the case of sudden turning off of a trap, the time evolution of the scaling parameters can be described using the equation,

$$\frac{d^2}{d\tau^2}\lambda_\rho = \frac{1}{\lambda_\rho^3\lambda_z} \quad (3.61)$$

$$\frac{d^2}{d\tau^2}\lambda_z = \frac{\epsilon}{\lambda_\rho^2\lambda_z^2} \quad (3.62)$$

$\tau = \omega_\rho t$ and $\epsilon = \omega_z/\omega_\rho$.

A thermal cloud expands isotropically once released from a trap, and the width of such a cloud $\sigma_{\rho,z}$ can be written as,

$$\sigma_{\rho,z}^2 = \frac{k_B T}{m} \left(\frac{1}{\omega_{\rho,z}^2} + t^2 \right) \quad (3.63)$$

where T is the temperate of the cloud and m is the atomic mass. The initial cloud size in a trap is determined by the trapping frequencies while the rate of expansion is determined by the temperature of the cloud. The time of flight measurement can be used to determine the temperate of the atoms.

3.2.6 Quantum degenerate mixtures

To describe the quantum degenerate mixtures of two species, a pair of coupled Gross-Pitaevskii equations are used with additional terms for interspecies interactions,

$$\left[-\frac{\hbar^2}{2m_1}\nabla^2 + V_1(\mathbf{r}) + g_{11}|\psi_1(\mathbf{r})|^2 + g_{12}|\psi_2(\mathbf{r})|^2 \right] \psi_1(\mathbf{r}) = \mu_1\psi_1(\mathbf{r}) \quad (3.64)$$

$$\left[-\frac{\hbar^2}{2m_2} \nabla^2 + V_2(\mathbf{r}) + g_{21}|\psi_1(\mathbf{r})|^2 + g_{22}|\psi_2(\mathbf{r})|^2 \right] \psi_2(\mathbf{r}) = \mu_2 \psi_2(\mathbf{r}) \quad (3.65)$$

The $\psi_1(\mathbf{r})$ and $\psi_2(\mathbf{r})$ are the wavefunctions for species 1 and 2 respectively with mass m_1 and m_2 and chemical potential μ_1, μ_2 . The interactions between the atoms are the dominating terms in the equations, the terms $g_{11}|\psi_1(\mathbf{r})|^2$ and $g_{22}|\psi_2(\mathbf{r})|^2$ describe the intraspecies interactions, and the interspecies interactions are encompassed in the additional terms $g_{12}|\psi_2(\mathbf{r})|^2$ and $g_{21}|\psi_1(\mathbf{r})|^2$. The interaction coupling constants are given by,

$$g_{11} = \frac{4\pi\hbar^2}{m_1} a_{11} \quad (3.66)$$

$$g_{22} = \frac{4\pi\hbar^2}{m_2} a_{22} \quad (3.67)$$

$$g_{12} = g_{21} = 2\pi\hbar^2 \left(\frac{m_1 + m_2}{m_1 m_2} \right) a_{12} \quad (3.68)$$

with a_{11} and a_{22} being the single species scattering lengths and a_{12} being the inter-species equivalent.

The relative strength Δ between the interspecies interactions and the intraspecies interactions can be used to characterise the behaviour of the mixture,

$$\Delta = \frac{g_{12}}{\sqrt{g_{11}g_{22}}} = \frac{a_{12}}{\sqrt{a_{11}a_{22}}} \sqrt{\frac{(m_1 + m_2)^2}{4m_1m_2}} \approx \frac{a_{12}}{\sqrt{a_{11}a_{22}}} \quad (3.69)$$

When Δ is less than -1, the mixture becomes miscible and unstable against collapse as the attractive interactions between the two species dominate over the repulsing interactions within the BECs. In the case when $|\Delta|$ is less than 1, the intraspecies interactions dominate, resulting in a stable and miscible mixture. When Δ is larger than 1, a phase separation of the two components is caused by the dominant repulsive interspecies interactions.

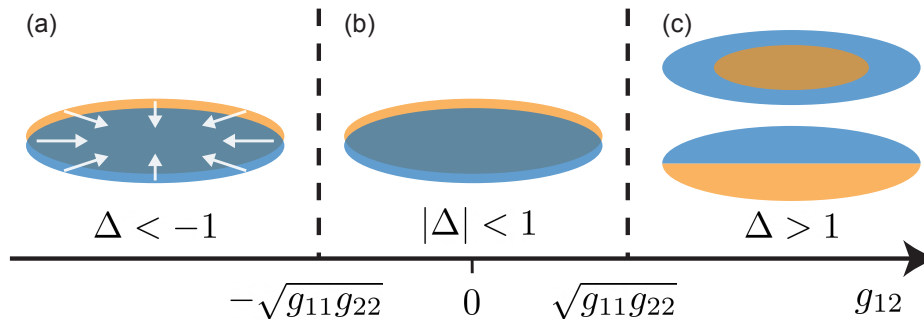


Figure 3.6. Characteristics of a dual-species BEC as a function of the interaction parameter $\Delta = \frac{g_{12}}{\sqrt{g_{11}g_{22}}}$.

4 The road to degeneracy

In this chapter, a guide on how to generate the dual-species Bose-Einstein condensates is given along with the changes made to the platform. An extensive discussion on the vacuum system and the atomic sources is provided as they are two of the main bottlenecks for the continuous operation of the platform.

4.1 Vacuum system

The quality of the vacuum is assessed by the pressure and the mean free path of the particles inside the vacuum. The mean free path is the average distance that a particle can travel between two consecutive collisions. Based on the pressure and the mean free path, vacuums can be divided into the following categories. In order

Vacuum quality	Pressure (Pa)	Mean free path (m)
Atmospheric pressure	1.013×10^5	6.8×10^{-8}
Low vacuum	1×10^5 to 3×10^3	10^{-8} to 10^{-4}
Medium vacuum	3×10^3 to 1×10^{-1}	10^{-4} to 10^{-1}
High vacuum	1×10^{-1} to 1×10^{-7}	10^{-1} to 10^3
Ultra high vacuum	1×10^{-7} to 1×10^{-10}	10^3 to 10^8
Extremely high vacuum	$<1 \times 10^{-10}$	$>10^8$
Outer space	$<3 \times 10^{-15}$	$>10^8$
Perfect vacuum	0	∞

Table 4.1. Pressure and the mean free path ranges of each quality of vacuum.

to carry out the work with degenerate gases, an ultra high vacuum below 10^{-10} mbar is required.

4.1.1 An overview of the vacuum system

The vacuum system can be divided into four sections, the pumping station, the atomic source, the pumping stages and the science cell. Each section is connected to a valve which can be used to isolate the section from the rest of the system. A schematic view of the vacuum system can be found in Fig 4.1.

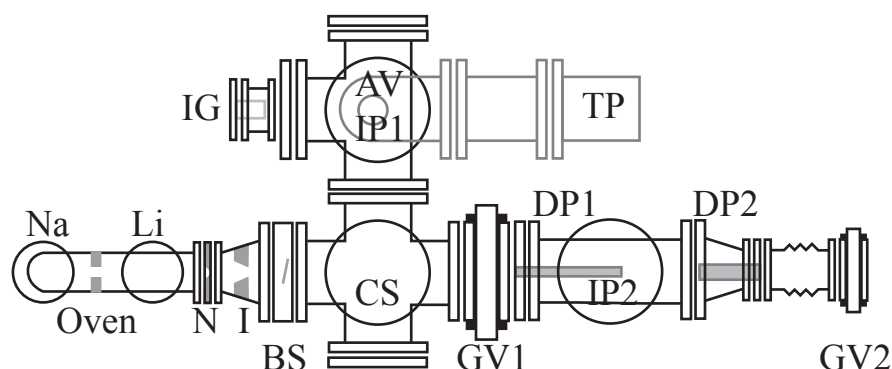


Figure 4.1. The front part of the vacuum system. (Top view). Taken from [81].

The pumping stage section includes a roughing pump, a turbo pump, a ventilation valve, a pressure gauge, a metal angle valve and a residual gas analyser (RGA). The whole section serves as the primary tool to achieve a high/ultra-high vacuum.

The oven section consists of the dual specie oven, a six-way cross and a metal gate valve. The gate valve is connected to the pumping stage via a six-way cross. An ion pump is connected to one flange of the six-way cross to maintain the pressure in the region. This section has the highest pressure around 3×10^{-8} mbar in the whole vacuum system.

The intermediate section includes two differential pumping stages, a 75 L ion pump and a gate valve connected to the science cell. The function of this section is to limit the amount of the particle flow from the oven section to the science cell in order to achieve a sufficiently low pressure.

The science cell section is located at the end of the experiment where sodium and lithium atoms are trapped and cooled to quantum degeneracy as shown in Fig 4.2. The science cell is connected to both a 150 L titanium sublimation pump and an ionisation gauge. The titanium sublimation pump is used to achieve and maintain the ultra-high vacuum required for degeneracy experiments. The hot-filament ionisation gauge is also installed to monitor the pressure in the science cell region.

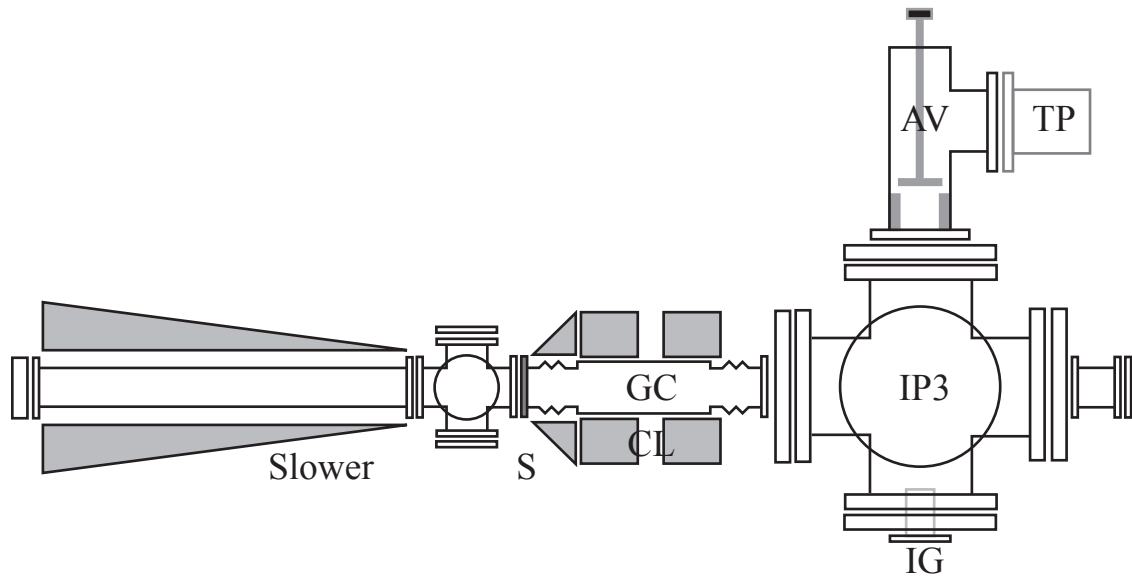


Figure 4.2. The rear part of the vacuum system including the science cell section (Top view). Taken from [81].

4.1.2 Lifetime of the traps

The lifetime of an atom trap is predominantly determined by the amount of residual background particles. The background particles collide with the atoms trapped causing losses. In order to reach quantum degeneracy, atoms in the trap require a long lifetime for going through all the different stages of cooling processes. On this platform, the amount of time it takes to reach degeneracy is around 50 seconds. As a result, an ultra high vacuum with a pressure in the region of 1×10^{-10} mbar is necessary to maintain the required lifetime.

The hot-filament ionisation gauge installed in the science cell section gives an indication of the pressure in the region. The gauge has a lower detection limit of 2.7×10^{-11} mbar, therefore a more precise way of determining pressure is to measure the lifetime of the atoms in the traps. Such measurements can be obtained during different stages of the experiment. On the platform, measurements are usually done in the magnetic trap with sodium atoms, after the first evaporative cooling ramp to reduce the cycle time of the measurements. Atoms are held in the trap for a given time before imaging. A graph of atom number against the holding time is plotted and a simple exponential decay curve is fitted to determine the lifetime of the trap. Two sets of measurements can be found in Fig. 4.3, the first set of measurements were carried out when the ion gauge had a reading below the detection limit and the second was done when the reading on the ion gauge was at 1×10^{-10} mbar.

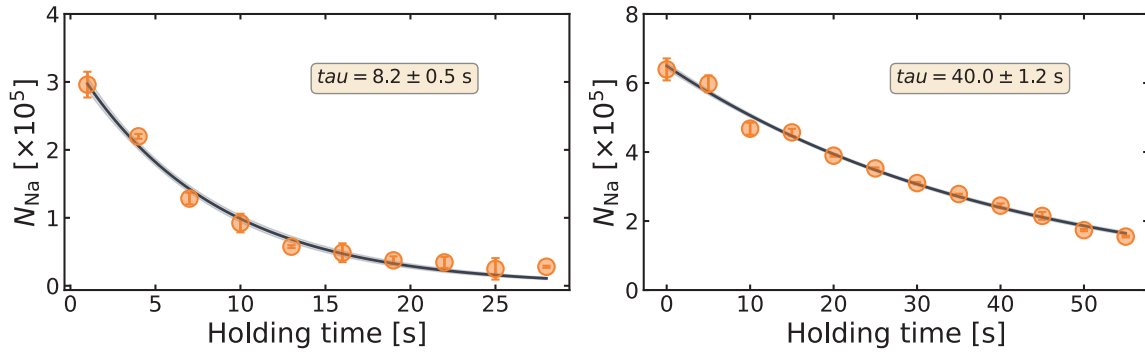


Figure 4.3. A comparison of the magnetic trap lifetime measured between a functioning and non-functioning vacuum. **Left:** an example of lifetime measurement for the atoms in the magnetic trap under a non-functioning vacuum. **Right:** an example of lifetime measurement for the atoms in the magnetic trap under a functioning vacuum.

4.1.3 Differential pumping stages

The differential pumping stages are located in the intermediate region between the atomic source and the science cell to limit the flow rate of the particles into the science cell. The pumping stages are usually implemented by using long tubes with small diameters. Such tubes geometrically favour the passing of collimated atomic beams with few collisions over the background particles. The probability of a background particle passing through the tube is relatively small due to a large number of the collisions it experiences in the tube.

To quantify the reduction in pressure, the differential pumping factor is defined as the ratio of the pressures in the two regions the pumping tube is connected to. Given two vacuum chambers connected with a differential pumping tube, the pressure in the first chamber is P_1 , the base pressure in the second chamber is negligible with pumping speed S_2 and the conductance of the tube is C , which is small. The gas leak into the second chamber is given by $P_1 C$ and therefore the pressure in the second chamber is given by $\frac{P_1 C}{S_2}$, then the ratio between P_1 and P_2 is given by $\frac{S_2}{C}$ which can, in theory, be large.

On the sodium-lithium platform, the ion pump in the science cell region provides a pumping speed of 500 L s^{-1} , the conductance of the pumping tubes cannot be too small so that the atomic flux can pass through. Given the high operating temperature needed for the atomic source, the best pressure can be achieved in the oven region is around $3 \times 10^{-8} \text{ mbar}$ after several weeks of baking. Combining all these effects, two differential pumping stages are used on the experiment as shown in Fig

4.4. The first pumping stage reduces the pressure between the oven region and the intermediate chamber by a factor of 100, the pressure in the intermediate chamber should be in the region of 2×10^{-10} mbar in the ideal scenario, which can be checked by the reading of the ion pump located in this region. The second pumping stage is located between the intermediate chamber and the science cell which reduces the pressure by a factor of ten. An ultimate pressure in the region of 2×10^{-11} mbar can be achieved which is sufficiently low for creating Bose-Einstein condensates.

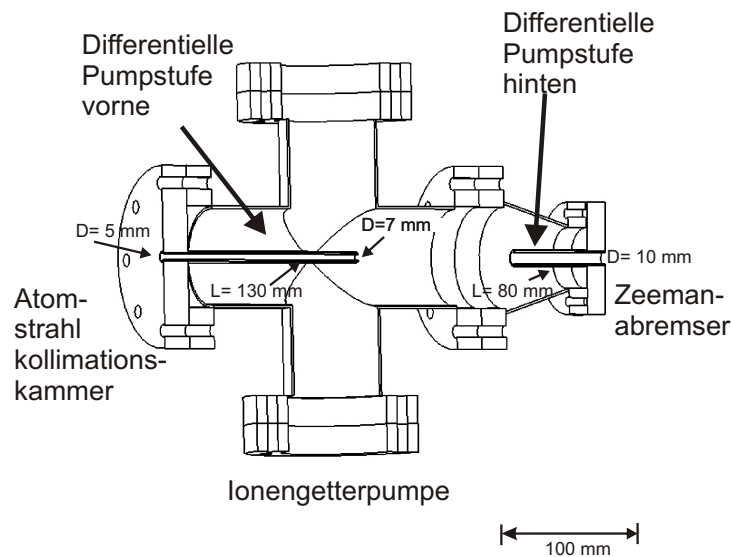


Figure 4.4. A schematic diagram of the two differential pumping stages used in the experiment. The first one is 130 mm long and has a conical shape which reduces the pressure by a factor of 100. The second one is 80 mm long which reduces the pressure by a factor of 10. Taken from [82].

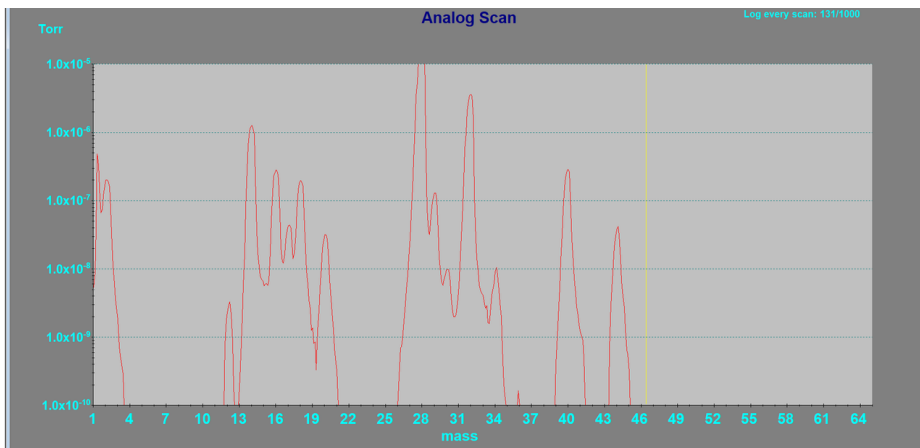
4.1.4 Ultra high vacuum generation

Ultra high vacuums can only be achieved via several stages with different pumping mechanisms. A basic guide on generating ultra high vacuum is given below.

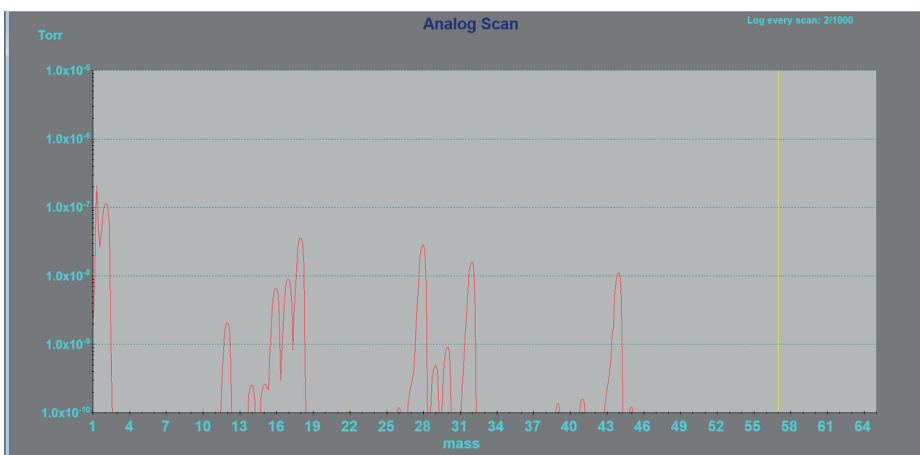
- **Pre-baking and cleaning:** the vacuum components need to be cleaned properly using detergents such as ethanol and acetone. Certain components need to be baked properly at different temperatures before installation to speed up the degassing processes. In particular, the atomic source needs to be baked at a temperature which is higher than the operating temperature to reduce

the amount of hydrogen coming out of the stainless steel. Excessive hydrogen can be the limiting factor for achieving an ultra high vacuum as some ion pumps perform poorly in absorbing hydrogen. Vacuum firing is also another recommended option when manufacturing the vacuum components to reduce the hydrogen problem. Components such as viewports and valves with maximum baking temperatures needs to be checked before baking.

- **Vacuum assembly:** after pre-baking and cleaning, the components can be assembled together using appropriate gaskets and screw sets. Gaskets with different materials are used in different conditions, and three different types of gaskets are used on the platform. Nickel gaskets are used in corrosive environments such as in the atomic source, silver gaskets are used where high temperature bake-outs are required and copper gaskets can be used where a high temperature is not often required. In order to seal the vacuum, hex socket screws, washers and nuts are used in vacuum applications. Non-magnetic 316 stainless steel sets are used in the platform, and like the choice of the gaskets, silver coated screw sets are used in the atomic source region to avoid welding of the components. A criss-cross (star) tightening pattern would normally be used to ensure an even preload distribution is achieved in the joint.
- **Primary pumping:** once the vacuum is closed, the roughing pump is started to generate a low or medium vacuum around 1×10^{-1} mbar. Oil-free pumps should be used to prevent contamination of the vacuum. The process should take fewer than 15 minutes if no major leak is present. Once the pressure is below 1 mbar, the turbomolecular pump can be switched on. The pressure then should drop further down to 1×10^{-6} mbar in half an hour in a clean and functioning vacuum.
- **Leak test:** after the pressure is below 1×10^{-4} mbar, a leak test should be carried out using a residual gas analyser or leak detector with helium gas. All the joints and the valves should be checked by spraying helium gas, and if a leak is present, further tightening is required.
- **Baking:** the baking process helps to speed up the pumping significantly by increasing the desorption and diffusion rate. After the leak test, the whole vacuum system should be wrapped with aluminium foil first, then heating bands and clamps can be installed on the system. Type K thermocouples are also placed onto the different parts of the system to monitor temperatures. The



(a) An analogue scan of the RGA showing the system with a major leak after primary pumping



(b) An analogue scan of the RGA showing the system without a major leak after primary pumping

Figure 4.5. A comparison between the vacuum system with and without a major leak after initial pumping.

wrapping process should be as uniform as possible with the focus on the pumps, valves and crosses. A second layer of aluminium foil are then used to prevent the heat loss from the system. The heat bands and clamps are connected to the tunable current sources for heating. The heating up should be done as homogeneously as possible while recording the temperatures of each component. A general rule of thumb is 1 degree per minute for most stainless steel parts, however components with glass require extra care to be taken. A strong temperature gradient should also be avoided to prevent any parts cracking. The residual gas analyser should be used constantly for monitoring purpose during the baking. Cooling down the system should only be carried out once the pressure dropped back to the value before heating up.

Another indication of a clean vacuum is only the hydrogen peak being present in the vacuum, as can be seen in the RGA in Figure 4.6.

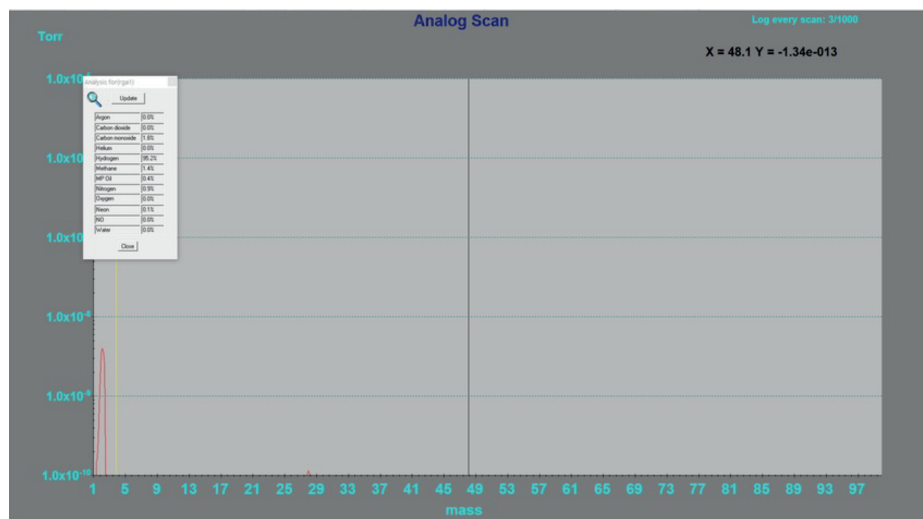


Figure 4.6. An indication of a clean vacuum in the RGA at high temperature.

- **Switching on the ion pumps:** the ions pumps in the system can be turned on once the vacuum system is at room temperature. When the ion pumps are switched on initially, a high current corresponding to high pressure can be observed on the controllers of the ion pumps due to the accumulation of particles in the ion pumps. However, the pressure should drop quickly. Pumps are left to run for some time to let the pressure settle.
- **Further baking:** if the final pressure is still not sufficiently low, further baking can be done with the ion pumps on as this is a quicker way to achieve the ultimate pressure in the system. The procedure is the same as the baking process mentioned above with more attention on the ion pump readings as those pumps only work below certain pressure.

4.2 Atomic source

4.2.1 Old oven design

The atomic source provides the sodium and lithium atoms required for the experiment. A dual-species atomic source is used in the experiment, the old design based on the work from Ketterle's group [83]. Given lithium and sodium have very different vapour pressures at a given temperature, as shown in Fig.4.7, a multi-chamber oven design is used.

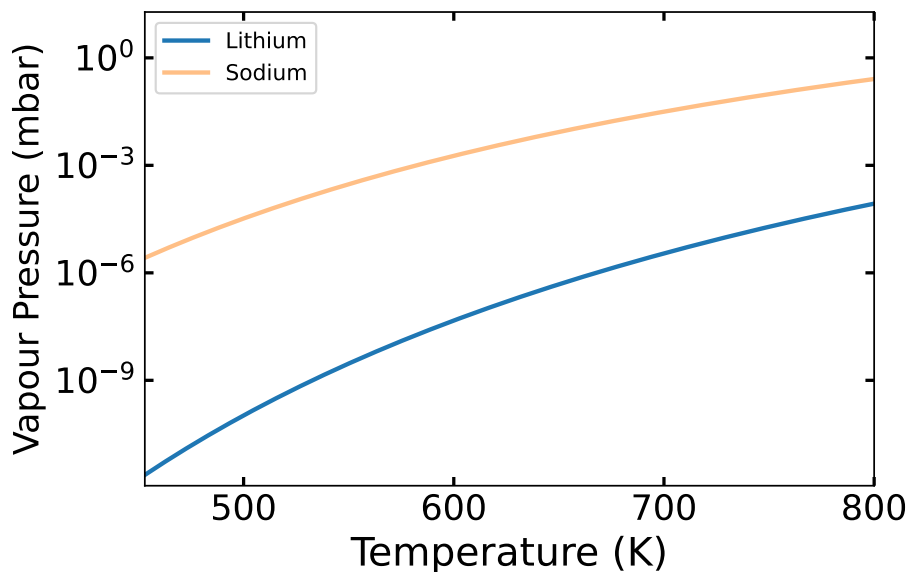


Figure 4.7. Vapour pressure of both sodium and lithium.

The design consists of two separate chambers and two nozzles as shown in Fig.4.8. Sodium and lithium chunks are filled into the two cups from the bottom using CF40 flanges. Both cups and nozzles are heated independently using heating clamps, and the temperature of each region can be controlled independently. The sodium atoms coming out of the reservoir enter into a mixing chamber through the small tube with diameter of 5 mm, and then atoms of both species go into a collimation chamber through the oven nozzle (4 mm diameter). The collimation of the atomic flux is carried out by the oven nozzle along with the copper block shown in Fig.4.9. The source is connected to the main part of the experiment via a CF63 flange. The atoms travelling along the direction of the Zeeman slower will get trapped in the science cell. The sodium and lithium reservoirs are heated at 360 °C and 380 °C respectively during the day. When the experiment is switched off at night, both reservoirs are cooled down to 260 °C overnight to recycle some

atoms. One common problem with this type of source is clogging, therefore both the mixing nozzle and oven nozzle are kept at 450 °C to prevent this. Nickel gaskets are used for both reservoirs and the connection to the main experiment due to high operating temperatures and the corrosive nature of the mixture.

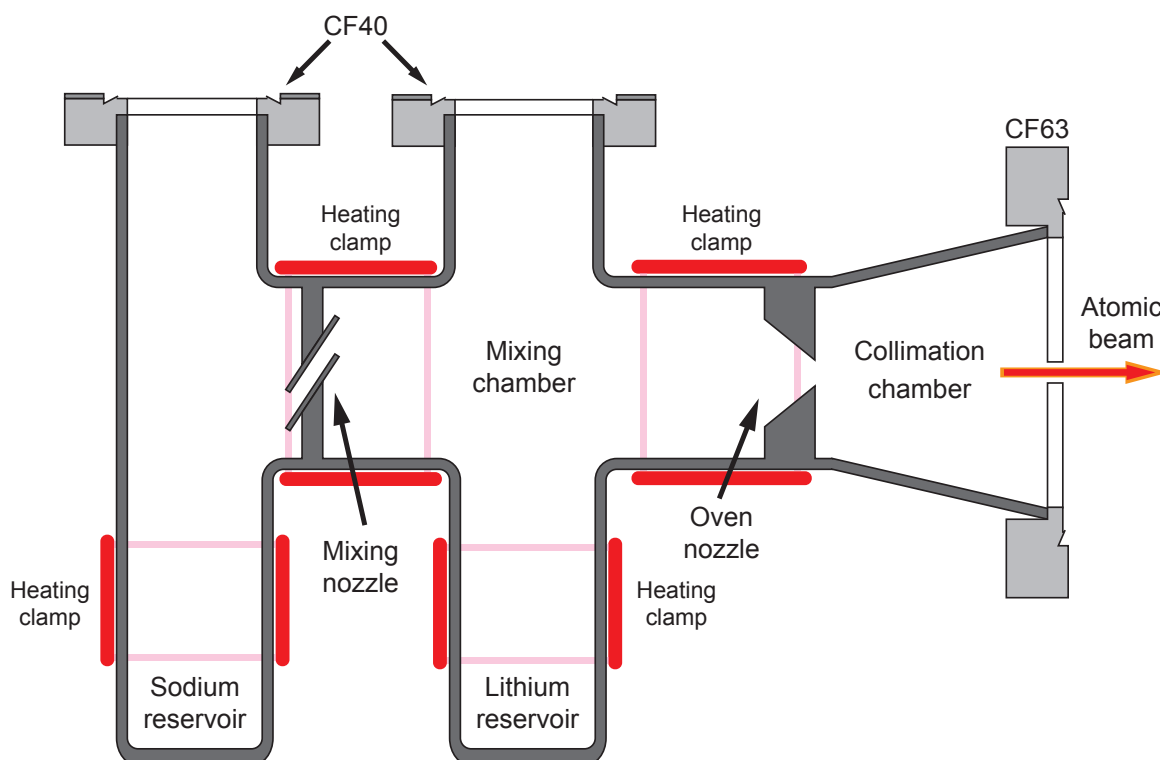


Figure 4.8. A schematic of the dual-species atomic source used on the experiment. Adapted from [84].

4.2.2 Oven change

A guide on refilling the atomic source, which is usually required every year, is given below with some remarks. In order to speed up the whole process, a spare oven is recommended to reduce the downtime of the platform.

- Two oven cups are filled with 50 g sodium and 25 g lithium in a glovebox filled with argon. As sodium and lithium are oxidised in the air rapidly, both alkali should be stored in a glovebox when not used. Scratch off any oxidation layers on the sodium chunks and cut the lithium rods to check for serious oxidation (black parts).
- Cooling down the oven by disconnecting all the heating clamps, then close the valve to the science cell and switch off all the ion pumps. Open the metal valve to the pumping station.

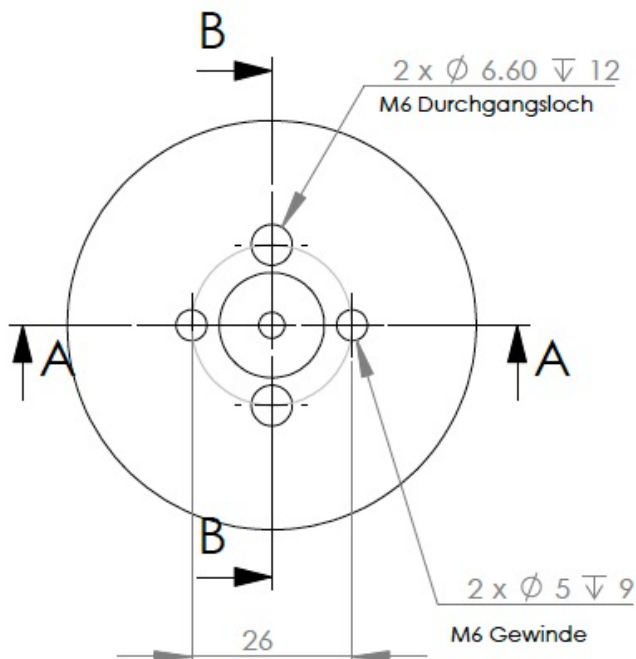


Figure 4.9. A technical drawing of the copper block used to collimate the atomic flux out of the source. Adapted from [82].

- Once the oven is cold, flush the system with nitrogen while disassembling the old oven and connect the new oven. Immediately start to pumping down and follow the instructions above to regenerate the ultra high vacuum.
- The oven taken from the system should be sealed properly with flanges and aluminium foils for sometime to get most of sodium and lithium fully oxidised. Then the oven can be moved into a fume cupboard for cleaning. First start to rinse the oven slowly with 99.9% ethanol, violent chemical reactions might happen as sodium and lithium react with ethanol producing heat and hydrogen (this process can take up to few days). Once all the sodium has reacted, water can be used to clean the oven once more. The chemical waste from the cleaning process usually has really high PH values and should be handled properly.
- Once the oven is clean, place it in a baking oven at 300 °C for one or two days before reuse.

4.2.3 Drawbacks of the old design

While the oven design has been used on the platform for several years, it has suffered from a few issues. The relatively low efficiency of the source leads to high

operating temperatures which reduces the lifetime of the source and increases the pressure in the source region. After a few years of running, the vacuum chamber becomes coated with a thick layer of sodium and lithium. The coating causes further degradation of the other components such as the valves, ion pumps and vacuum chambers. Over the course of this thesis, the ion pump near the oven had to be changed three times as white powder was found in the ion pumps, causing short circuits. The gate valve between the oven region and the slower region had to be changed every few years too, due to the severe coating causing leaks.

4.2.4 Effusive atomic sources

As a result of all the problems mentioned above, a new oven is designed to address these issues. The oven design is inspired by the work done in the group of Selim Jochim and the erbium oven used in Innsbruck [85, 86]. The oven works in the effusive regime along with a bright wall collimator which will be discussed in detail in this section.

The ideal gas law can be used to describe a box of ideal atomic gas in thermal equilibrium at temperature T ,

$$P = nk_B T \quad (4.1)$$

where P is the pressure, n is the number density and k_B is the Boltzmann constant. If such a box is connected to the vacuum with a circular aperture of diameter b_1 , the atoms then can escape from the box into the vacuum due to the pressure difference. The atoms can also collide with each other during the process, and the mean free path λ_{mfp} of an atom is given by following

$$\lambda_{mfp} = \frac{1}{\sqrt{2}\pi d_0^2 n} \quad (4.2)$$

where d_0 is the diameter of an atom. In the case of $\lambda_{mfp} < b_1$, the atoms will collide many times before leaving the box which can be described using fluid dynamics. On the other hand, in the effusive regime ($\lambda_{mfp} \geq b_1$), the collisions are mainly between the atoms and the wall instead of between atoms. Diffusive reflections can occur in this regime, where an atom sticks to the wall during a collision and gets emitted by the wall at a random angle. As a result of such process, atoms hitting in the inner surface of the aperture can return to the box. Both the velocity and the spatial distribution of the atoms inside the box is independent of the process of atoms leaving the box in the effusive regime.

Assuming the oven works in the effusive regime, the flux of the atoms leaving the box can be calculated as following,

$$\Theta = \frac{1}{4} n v_{rms} A \quad (4.3)$$

where n is the number density of the atoms inside the box, v_{rms} is the mean speed of the atoms and A is the area of the aperture. To figure out the mean speed of the atoms inside the box, the 3D Maxwell-Boltzmann velocity distribution can be used,

$$P_v(T) = C \left(\frac{m}{k_B T} \right)^{\frac{3}{2}} v^2 e^{-\frac{mv^2}{2k_B T}} \quad (4.4)$$

where C is the normalisation constant and m is the mass of an atom. Both the most probable velocity and the mean velocity then can be calculated using the following equations,

$$v_{mp} = \sqrt{\frac{2k_B T}{m}} \quad v_{rms} = \frac{2v_{mp}}{\sqrt{\pi}} \quad (4.5)$$

4.2.5 Characterisation of the new oven design

In the new design, two separate collimation tubes are introduced to collimate the atomic flux of individual species as shown in Fig 4.10. Atoms coming out of each reservoir enter a collimation tube with diameter of 6.25 mm heated to 450 °C which is well above the melting point of sodium (98 °C) and lithium (180 °C) to prevent clogging. The atoms stick to the walls of the heated tube can be re-emitted with a certain probability to exit the collimation tube [87]. The design is expected to increase the lifetime of the source significantly by reducing the number of lost atoms coming out the source. These lost atoms also cause coating on the vacuum chambers as well as damaging the ion pumps. Two separate reservoirs are also used for independent temperature control of sodium and lithium given their difference in the vapour pressure. The design also focuses on getting rid of the chemical reactions between sodium and lithium at high temperatures by isolating one from the other. There is a thin wall which has a thickness of 1.5 mm between the apertures of the collimation tubes which physically prevents any reactions from happening.

The new design was tested on the platform when the ion pump near the oven was broken. The procedure for changing the oven was followed and the ultra high vacuum was generated after the change. In order to characterise and monitor the performance of an atomic source, both qualitative and quantitative approaches were used on the platform. A simple qualitative method used is to monitor the fluorescence from sodium atoms at the first six way cross near the oven, where a viewpoint is installed for this purpose as shown in Fig.4.11.

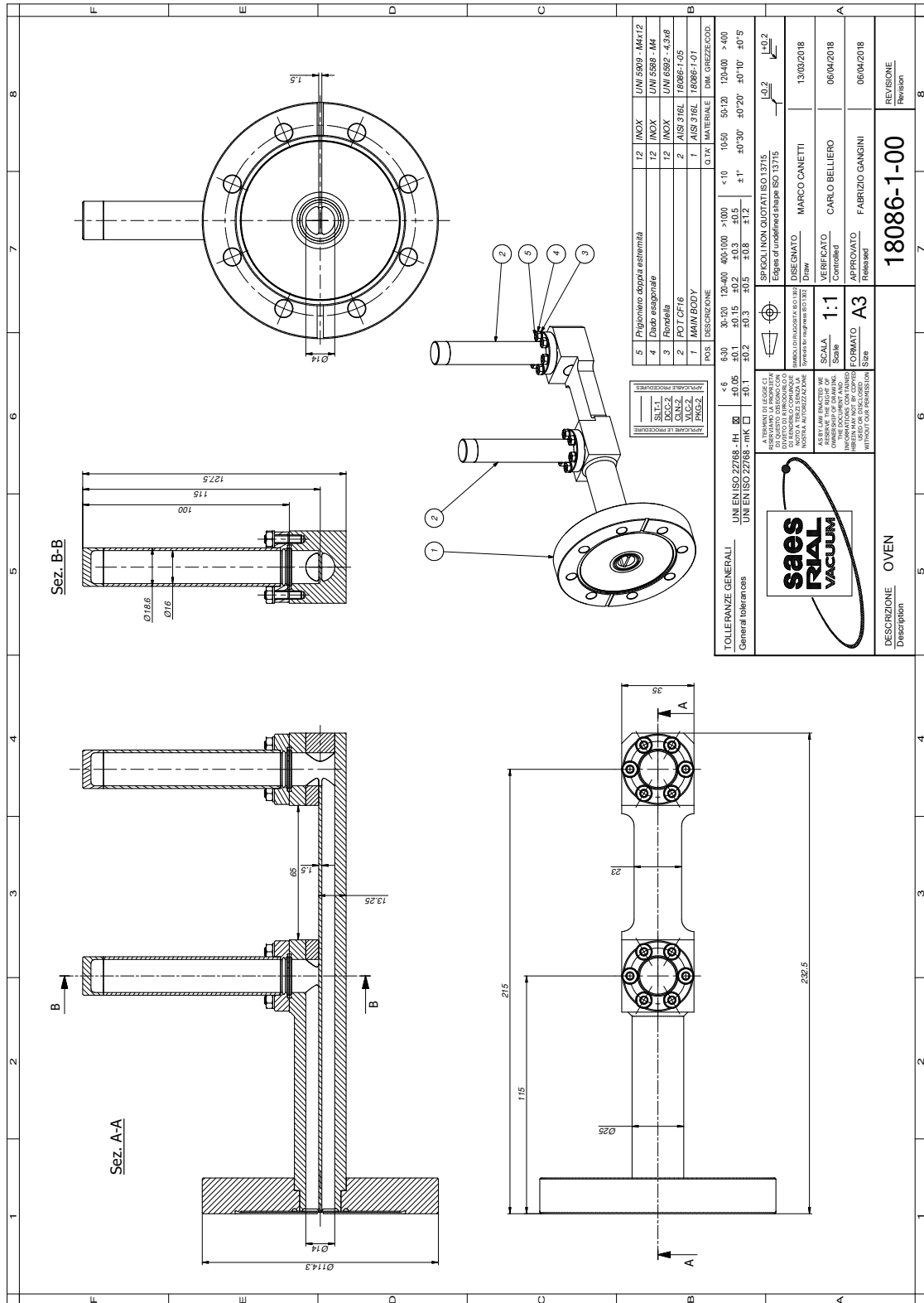
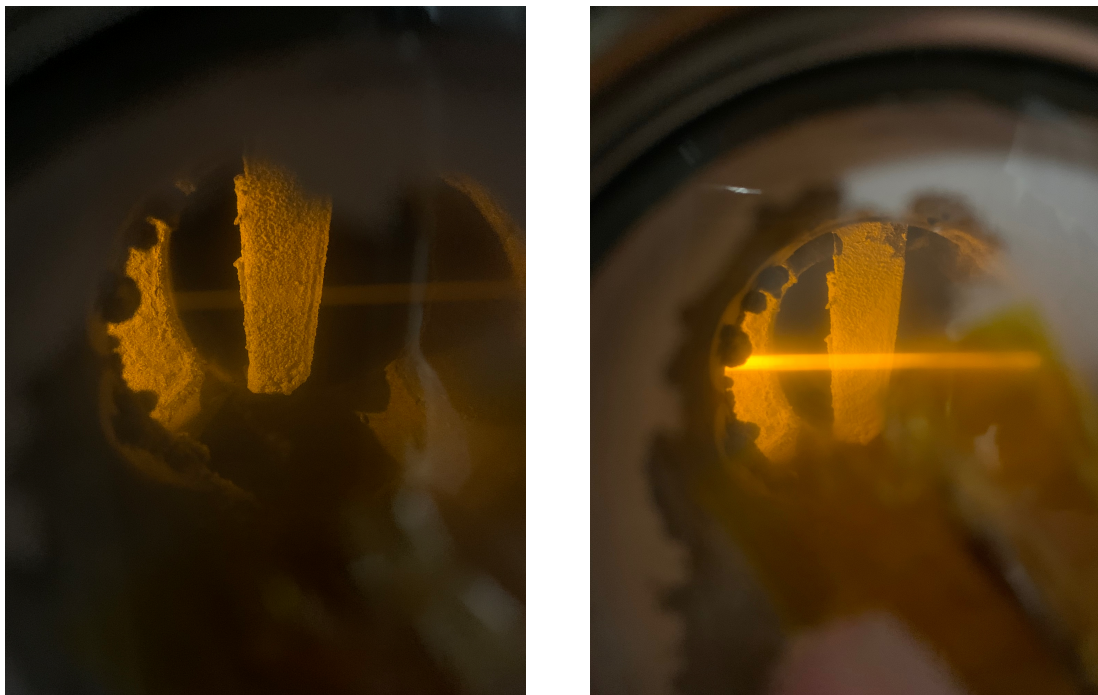


Figure 4.10. A technical drawing of the new oven design. Two separate long tubes are used to collimate the atoms of each specie and increase the lifetime of the source. A thin wall of thickness 1.5 mm is designed to block the chemical reactions between sodium and lithium.



(a) An example of relatively low oven fluorescence coming out of the oven.

(b) An example of relatively high oven fluorescence coming out of the oven.

Figure 4.11. A comparison of the oven fluorescence seen at the viewport next to the oven.

While the fluorescence observed next to the oven gives a rough indication of the performance of the source, there is a more precise method which measures the fluorescence signal next to the science cell. A CCD camera (MAKO G-030B) is mounted at the viewport next to the science cell and two pictures are taken during a single fluorescence measurement as shown in Fig.4.12. One picture is taken with the magnetic field of the Zeeman slower and one without, and then the difference in counts of the two pictures is calculated as a quantitative measure for the performance of the atomic source.

Provided all the advantages of the new oven design mentioned above, there are several issues which limit the performance of the oven in this specific system due to pressure constraints, the main one being the alignment of the Zeeman slower beam. The differential pumping stages used on the platform generally have small diameters with 5 mm being the smallest, as shown in Fig. 4.4. For the laser beam of the Zeeman slower to pass through the pumping stages, the beam has to be very focused to around 2 mm in diameter at the entrance of the oven. The 1.5 mm thin-wall used to decouple the species as shown in Fig.4.10 blocking most of the slower beam leads to a small portion of the atoms coming out the source being slowed and

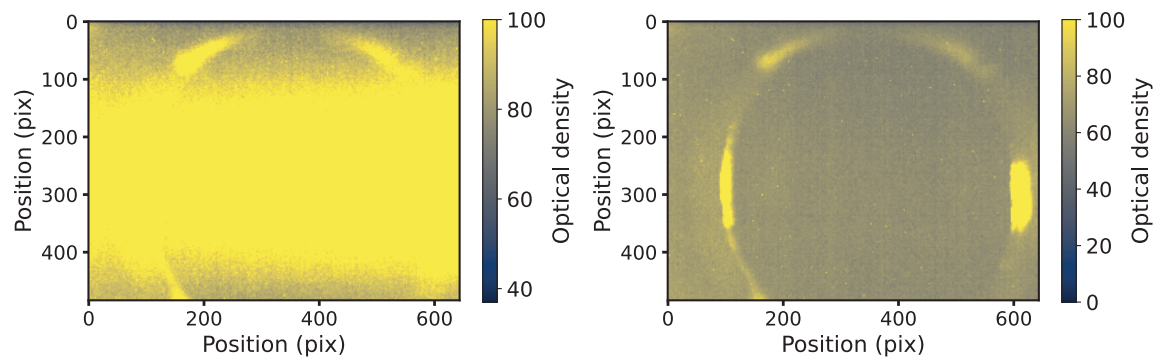


Figure 4.12. **Left:** a signal picture shows some fluorescence where the Zeeman slower magnetic field is on. **Right:** a reference picture shows no fluorescence where the Zeeman slower magnetic field is off.

captured in the MOT region. Overall, the new atomic source is not suitable for the platform due to the geometries of the pumping stages and the Zeeman slower.

During the work on this thesis, the vacuum system has been opened several times to change the atomic source and replace the broken components such as the ion pumps. The amount of sodium and lithium accumulated inside the vacuum system absorbed a significant amount of water during the process. Sodium hydroxide and lithium hydroxide were formed in the vacuum chamber especially around the regions of valves and pumping stages. Both chemical compounds have melting points above $300\text{ }^{\circ}\text{C}$ which makes cleaning via baking extremely challenging.

4.3 Laser Systems

Laser cooling and trapping require light with different frequencies to address transitions between the internal states of atoms. Given two different species are used in this platform, two independent laser systems are implemented.

For sodium, a laser (TA-SHG pro-589) from Toptica Photonics which provides around 1.3 W power is used. There are three main parts of the SHG laser, the master laser which emits 30 mW at 1178 nm , a tapered amplifier which amplifies the light coming from the master laser to around 2.5 W and a folded ring cavity in a bow-tie configuration which generates 1.3 W at 589 nm for laser cooling. The coupling into the tapered amplifier and the SHG cavity are managed automatically by two pairs of piezo-mirrors.

For lithium, two commercial lasers from Toptica in a master-slave configuration are used in the platform. The master laser (DL pro) which provides roughly 30 mW

is used only for the spectroscopy. The slave laser (TA pro) outputs around 320 mW and is used for laser cooling. The slave laser is frequency stabilised using an offset lock. Additionally, a homemade tapered amplifier seeded with 50 mW from the slave laser provides the power (280 mW) needed for the repumping transition for ${}^7\text{Li}$.

4.3.1 Spectroscopy path

The sodium laser is locked on the $F = 2$ to $F' = 3$ crossover transition of the sodium D_2 line using the technique of saturated absorption spectroscopy as described in [88]. A commercial sodium vapour cell (Thorlabs CP25075-NA) is heated up to 150°C in the spectroscopy setup. A simple pump-probe scheme is used, in which a pump beam is modulated using a 71 MHz AOM with a +1 order in a double path configuration while the probe beam is monitored with a photodiode. The obtained spectroscopy signal is then sent into a lock-in amplifier (LIA-BV(D)-150) from FEMTO along with the 22 kHz reference signal used to modulate the spectroscopy AOM. An in-house built PID controller is used to lock the laser using the error signal generated from the lock-in amplifier.

Similar to the sodium spectroscopy setup, the lithium master laser is locked on to the $F = 2$ to $F' = 3$ transition of the ${}^7\text{Li}$ D_2 line. The vapour cell which contains both ${}^6\text{Li}$ and ${}^7\text{Li}$ is manufactured in-house as described in [89]. The temperature of the cell is actively stabilised at 450°C while operating and 360°C when on standby. The stabilisation system is also used in the sodium-potassium mixture platform. The same pump-probe scheme used on sodium is implemented on lithium too, with the only difference being the -1 order used in the double path for the pump beam.

For the lithium slave laser, an offset lock is used to stabilise the frequency. The output of the master laser and slave laser are combined using a narrowband fibre optic coupler (TN670R5A2) from Thorlabs. The combined signal is monitored by a photodiode from Hamamatsu which is then mixed with a reference signal from a voltage controlled oscillator. The combined signal is used as the error signal to lock the slave laser with a PID controller. One big advantage of the locking scheme is that the offset frequency between the two lasers can be controlled during the experiment, which is exploited in different loading stages of the lithium MOT.

4.3.2 MOT and repumper path

In order to capture sodium atoms in a magneto-optical trap, both cooling and repumping lights are needed. The frequencies needed for cooling and repumping

as shown in Fig 4.13 are generated using standard acousto-optic modulators from Gooch & Housego. In particular, the repumping transition around 1.78 GHz is generated using a 1.7 GHz acousto-optic modulator (EF-1700-100-589) from Brimrose Corp along with a standard AOM (120.7 MHz) from Gooch & Housego. The first order efficiency of the 1.7 GHz AOM is between 5 % and 10 % which requires re-aligning regularly. The light passing through the AOMs is transferred to the experimental table using single-mode fibres.

To generate a lithium MOT, the light for the cooling transition comes out of the lithium slave laser. The cooling light is coupled into the same fibres as for the cooling light for sodium. A part of the light (50 mW) from the slave laser is used to seed the home-built tapered amplifier which provides the light for the repumping transition. The repumping transition is around 800 MHz away from the cooling transition for lithium as shown in Fig 4.14. The home-built tapered amplifier includes a 350 MHz AOM in the double-path configuration to address this issue. The seed light is fibre coupled onto a separate platform where the home-built TA is placed and the output of the TA is fibre coupled back to the experimental table. The repumping light for lithium is made to overlap with the MOT light and coupled into the same fibres.

On the experimental table, the laser light for cooling with circular polarisation is retro-reflected by the mirrors in three perpendicular directions to create a three-dimensional confinement. The linearly-polarised repumper light for sodium is shone in at Brewster's angle to the science cell to minimise the loss from reflections. The centre of the repumper beam is shielded to create a dark-spot MOT, where no atoms are pumped at the centre of the MOT to increase the phase space density [90]. For lithium, the repumping and MOT light share the same optical paths.

4.3.3 Zeeman slower path

To capture a sufficiently large amount of atoms in a MOT, the atoms coming out the source need to be slowed down to a range of velocities that can be captured for the MOT. Several different methods such as 2D-MOTs and Zeeman-slowers are available for this purpose, a Zeeman slower is used on the platform due to the age of the experiment. In the case of sodium, the cooling transition used for the Zeeman slower is generated with an AOM, and the repumping transition comes from the sideband of an Electro-optic modulator from QUBIG. In the case of lithium, the cooling light is provided from the slave laser and the repumping light is from the TA. The slower light for both species is shone in from the viewport at the rear end of the experiment in free space. To focus the light to pass through the differential

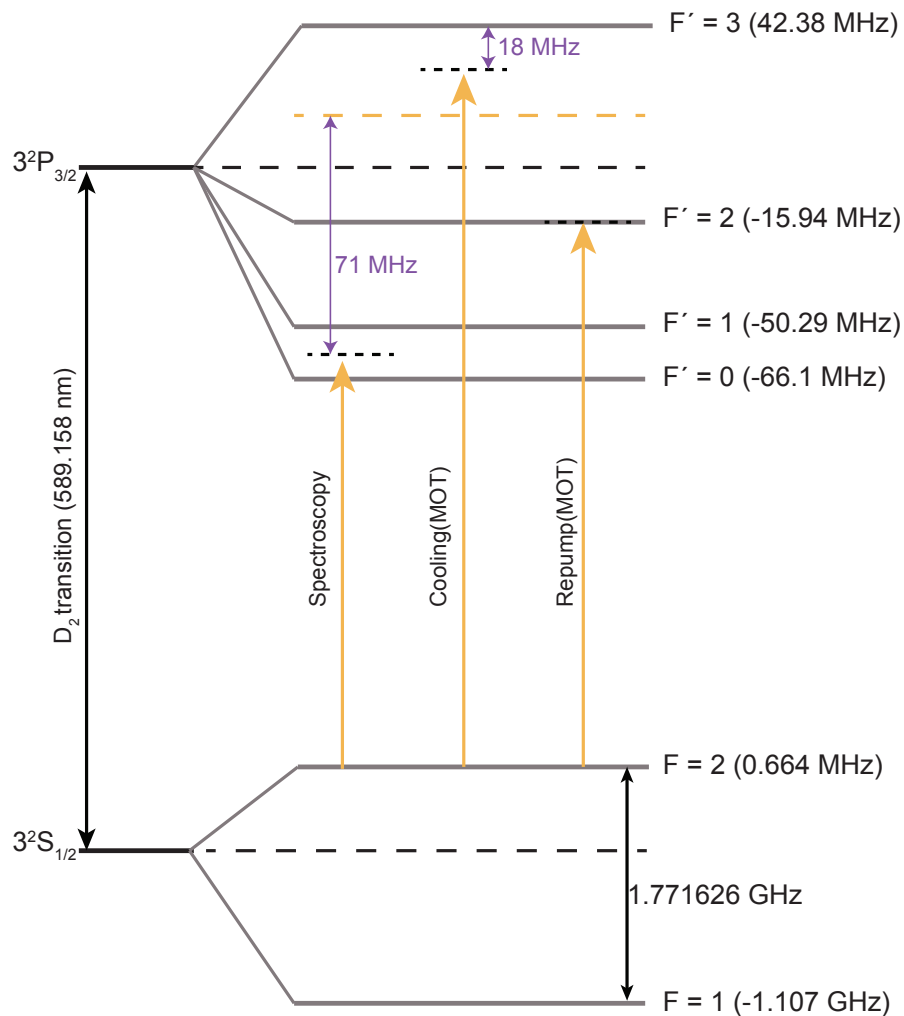


Figure 4.13. The hyperfine structure of the Na D_2 transition. The cooling, repumping and spectroscopy transitions are all indicated. Adapted from [91].

pumping stages, a Galilean telescope is used.

4.3.4 Spin-polarisation path

With the spin-dependent nature of magnetic traps, only one fifth of the atoms from the MOT are transferred into the trappable state $|2, 2\rangle$. The remaining atoms in other states causing losses need to be removed. The spin-polarisation scheme used in the platform is based on the work done in the group of Utrecht [92]. The scheme utilises a combination of a magnetic field and optical transitions that are stable against polarisation imperfections and magnetic field instabilities, while still reducing the off-resonant scattering rate significantly. Two separated optical transitions known as the umpump and umpump repumper are used in the scheme.

For sodium, the umpump is generated using the +1 order of a 76 MHz AOM.

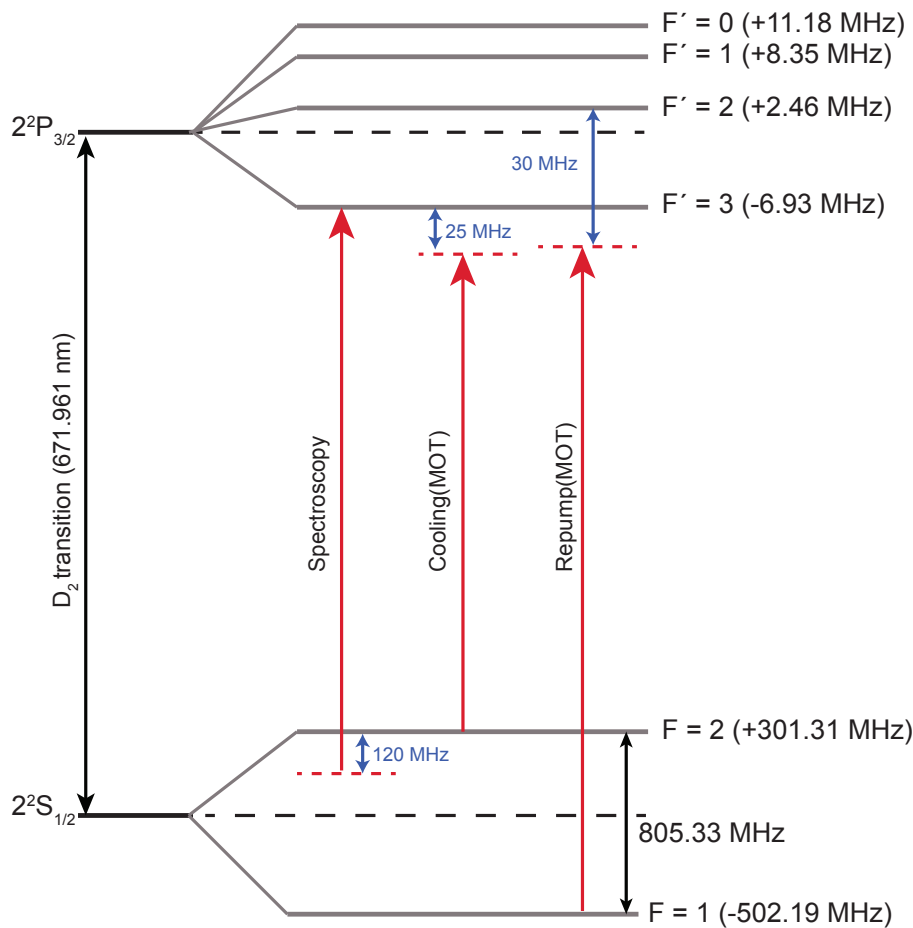


Figure 4.14. The hyperfine structure of the ${}^7\text{Li}$ D_2 transition. The cooling, repumping and spectroscopy transitions are all indicated. Adapted from [91].

The light passing through the 1.7 GHz AOM is frequency shifted by another 80 MHz for the unpump repumper beam. Working with ${}^7\text{Li}$ does not require the unpump repumper transition, therefore only the unpump is implemented using an 23.9 MHz acousto-optic deflector. All the beams for sodium and lithium are coupled into the same fibre and combined into one of the MOT beam's paths using a beam splitter on the experimental table.

4.3.5 Imaging path

A separate breadboard is used for imaging. Both sodium and lithium imaging frequency are controlled by using two separate AOMs, and due to the space constraint of the breadboard both AOMs are in single-path configurations. Part of the light from the lithium slave laser and the sodium laser are transferred onto the imaging breadboard using two fibres. After being frequency shifted by the respective AOMs, the light for sodium and lithium are then coupled into the same fibre connected to the

Path	Sodium(MHz)	Lithium-7(MHz)
Spectroscopy	+70.8	-120
Zeeman slower	-200.2	-271.3
MOT cooling	+82.3	-80.3
MOT repumping	+112.7	+150.2
umpump	+76.0	+23.9
umpump repumper	+80.0	N/A
Imaging	+105.3	-80.6
EOM (sodium)	+1713	N/A
acousto-optic modulator(sodium)	+1699.1	N/A

Table 4.2. The frequencies of the AOMs used in the optical setup on the platform for both sodium and lithium.

experimental table. On the experimental table, the imaging light is aligned to the direction of gravity. A detailed description of the imaging system is given in Section 4.7.

4.4 Magnetic fields

4.4.1 Zeeman slower coils

Another important ingredient needed for atom cooling and trapping is the magnetic fields. To slow the atoms coming out of the source, the magnetic field needed for the spin-flip slower is controlled using two pairs of coils known as the big slower and the smaller slower coils. An extra pair of coils known as the compensation coils is added to cancel out the excess magnetic field from the slower. To be able to manipulate the magnetic field generated by each coil independently, the three pairs of coils are connected to individual power supplies.

4.4.2 Cloverleaf Trap coils

In the science cell region, a design of the Cloverleaf Trap is implemented to generate all the necessary magnetic fields [76]. As shown in Fig.4.15, the design includes four pairs of coils, namely curvature, gradient, finetune and anti-bias. The curvature coils are arranged in the Helmholtz configuration, producing a magnetic field for axial confinement without introducing a field gradient near the centre of the trap.

The gradient coils provide radial confinement. The anti-bias coils are larger than the curvature coils to provide a more uniform field. The uniform field is used to lower the bias field at the centre of the trap. Finally, the finetune coils provide the magnetic field during the spin-polarisation stage. The coils are placed in a pair of holders in two separate planes to increase optical access to the trapped atoms.

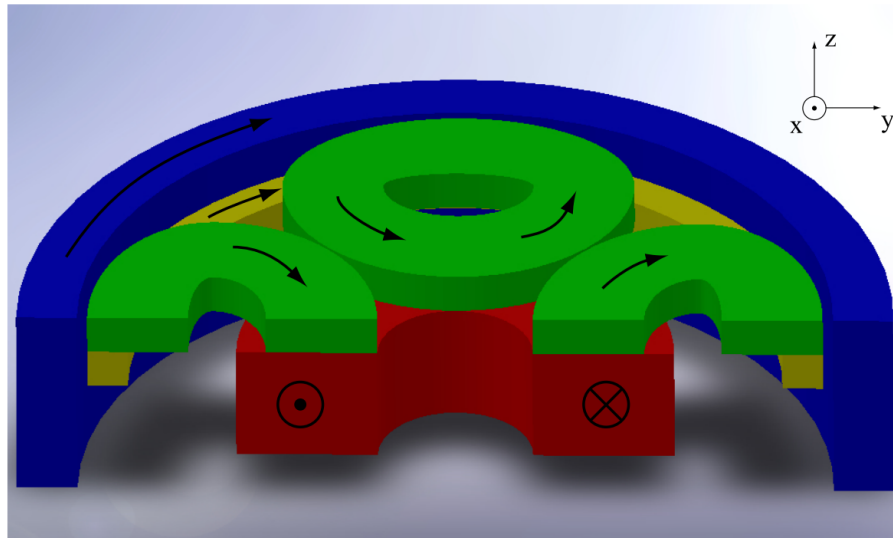


Figure 4.15. A cross-section view of the design of the Cloverleaf Trap. Four pairs of coils are present, gradient (green), anti-bias (blue), curvature (red) and finetune (yellow). Image taken from [88].

4.4.3 Fast switching of the magnetic fields

Each pair of coils is connected to a power supply for independent control. The fast switching of the magnetic fields is achieved by using a series of insulated-gate bipolar transistors (IGBTs). IGBTs act like switches with a very short response time and are controlled via the corresponding drivers. In the platform, both the IGBTs (MBI600U4-120) and drivers (VLA517R) used are from FUJI Electric. The driver has a logic input which is isolated electrically via an internal outcoupler and needs to be powered using a 24 V power supply. The output of the driver is either 15 V or -2 V corresponding to conducting and non-conducting of the circuit.

Given each pair of the coils needs an IGBT, 8 IGBTs were implemented in the platform. To control each IGBT independently and remotely, a driving circuit was also installed which includes 8 IGBT drivers and logic gates to protect the circuit. A series of common logic gates were used in the circuit to prevent false switches of the IGBTs, causing short circuits. Additionally, the switching frequency is limited

to 12 kHz by using monostable multivibrators. The details of the old design is given in [93]. However, in the course of this thesis, the driving circuit repeatedly malfunctioned due to issues related to the logic gates. As all of the IGBT drivers are coupled using a single circuit, issues in one path often held back the other paths. The old control circuit was replaced by a series of identical circuits to decouple all the IGBTs drivers from each other. Each circuit is used to control one IGBT only, which makes exchanging and replacing parts easier without affecting other working components.

The current design completely omits the logic gates used in the old design due to the complexity of the gates. The circuit consists of one input for power and one input for the control signal. The voltage regulator(L7820CV) is used to stabilise the input voltage. The output is directly connected to the respective IGBT. Eight identical circuits are used in the platform to enable the fast switching of the magnetic fields. The minimal switching time of the coils is around 3 ms, which is similar to the old control circuit and limited by the inductance of the coils. The finetune coils can be switched a lot faster with a minimum switching time of around 0.5 ms.

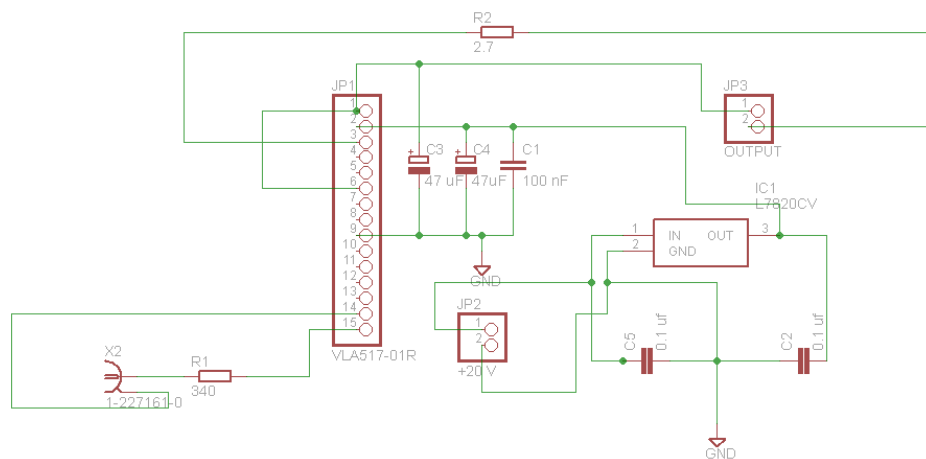


Figure 4.16. The schematic of the current control circuit for a single IGBT used on the platform.

4.5 Optical dipole trap

To trap atoms with far-detuned light, atoms can be treated as classic oscillators due to the low saturation intensity and scattering rate. The dipole potential and scattering rate can then be expressed as follows

$$U_{dip}(\mathbf{r}) = -\frac{3\pi c^2}{2\omega_0^3} \left(\frac{\Gamma}{\omega_0 - \omega} + \frac{\Gamma}{\omega_0 + \omega} \right) I(\mathbf{r}) \quad (4.6)$$

$$\Gamma_{sc}(\mathbf{r}) = \frac{3\pi c^2}{2\hbar\omega_0^3} \left(\frac{\omega}{\omega_0}\right)^3 \left(\frac{\Gamma}{\omega_0 - \omega} + \frac{\Gamma}{\omega_0 + \omega}\right)^2 I(\mathbf{r}) \quad (4.7)$$

where Γ is the natural linewidth of the transition, ω_0 is the frequency of the transition and ω is the frequency of the light. The dipole potential is proportional to the intensity. Therefore, the force acts to push the atoms away from the high intensity region when the detuning is positive ($\Delta = \omega - \omega_0 > 0$) and to attract atoms when the detuning is negative, and the force equates to zero when the light is on resonance ($\Delta = 0$). The dipole potential scales as I/Δ and the scattering rate scales as I/Δ^2 , therefore optical dipole traps work in a regime where the intensity is high, to maximise the trap depths, and where the detuning is also large to minimise the heating caused the scattering. Given the conservative nature of the dipole force, it cannot be used for cooling directly but more often is used for storing cold atoms. Far-detuned, high power dipole traps are often used to trap atoms with temperatures well below 1 mK as the heating rate is very low [94].

4.5.1 Trap setup

The optical dipole trap used in the platform has been modified during the course of this thesis. The dipole laser used has been changed from a 30 W DiNY cwQ 50 laser to a 50 W laser from IPG Photonics due to a malfunctioning chiller of the DiNY laser. The output beam waist of the IPG laser is around 2 mm which is a factor of 3 larger than the original from the DiNY, therefore a telescope is used to reduce the beam diameter. The output of the laser is divided into two paths known as the waveguide and dimple. The waveguide path is roughly 8 W and the dimple path is roughly 2 W measured near the science cell. A set of piezoelectric mirrors are used at the ends of the optical paths for a final adjustment of the beams onto the atoms. By scanning the control voltage of the mirror driver, the mirror can be tilted in small steps in a repeatable fashion which is crucial for the final alignment.

4.5.2 Trap geometry and frequencies

The geometry of the trap is arranged as follows; the waveguide beam is shone in at an angle of 8° with respect to the axis of the magnetic trap and the dimple beam is placed diagonally from bottom to top, making an angle of 50° to the direction of gravity. The beam waist of the waveguide is compressed to $30 \mu\text{m}$ by a cylindrical telescope in the direction of gravity and $60 \mu\text{m}$ in the horizontal direction. The dimple

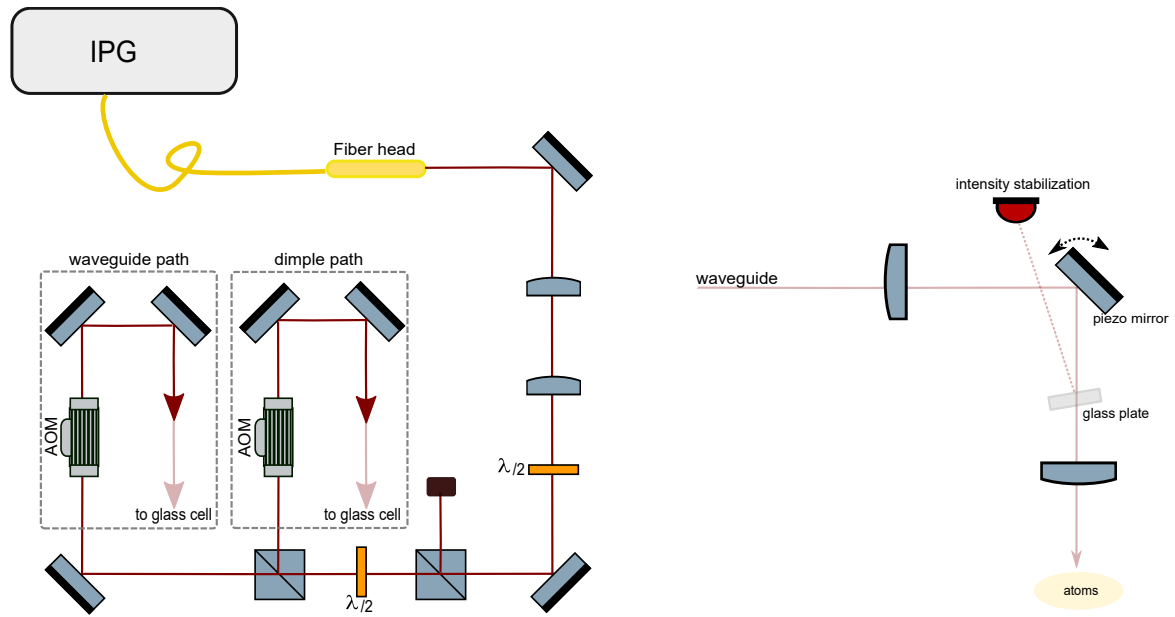


Figure 4.17. A schematic of the optical dipole trap setup. Taken from [91].

beam has a uniform waist of $80\ \mu\text{m}$. The cylindrical telescope is mounted on a translation stage which allows a fine adjustment of the focus.

The dipole trap is characterised by measuring the trapping frequencies in three directions. Trapping frequencies can be measured by either applying a magnetic field gradient or moving one of the dipole trap beams for a very short time. Both methods introduce oscillations of the atomic cloud within the trap. By holding the cloud in the trap and imaging the cloud after a fixed time of flight, the trapping frequencies are measured using the piezoelectric mirrors, with the cloud oscillations being induced by the mirror's movement. The position of the cloud can be extracted from the images and the frequency of the trap can be calculated by fitting a damped sine wave as shown in Fig. 4.18. The trapping frequencies in the x-y plane perpendicular to the direction of the gravity are measured using the main imaging path and the Retiga EXi camera. To measure the trapping frequency along the direction of gravity, a separate camera located next to the front MOT beam is used.

Before the dipole laser is changed, the trapping frequencies in Hz are given in the following [47]

$$\omega_x = 2\pi \times (243.7 \pm 1.5) \quad (4.8)$$

$$\omega_y = 2\pi \times (179.6 \pm 0.4) \quad (4.9)$$

$$\omega_z = 2\pi \times (410.4 \pm 6.5) \quad (4.10)$$

As more power is used in both dipole trap beams, higher trapping frequencies are expected. The current measurements for the trapping frequencies are shown

in Fig. 4.18 and the values obtained are listed below,

$$\omega_x = 2\pi \times (331.4 \pm 2.1) \quad (4.11)$$

$$\omega_y = 2\pi \times (243.2 \pm 1.3) \quad (4.12)$$

$$\omega_z = 2\pi \times (566.1 \pm 6.4) \quad (4.13)$$

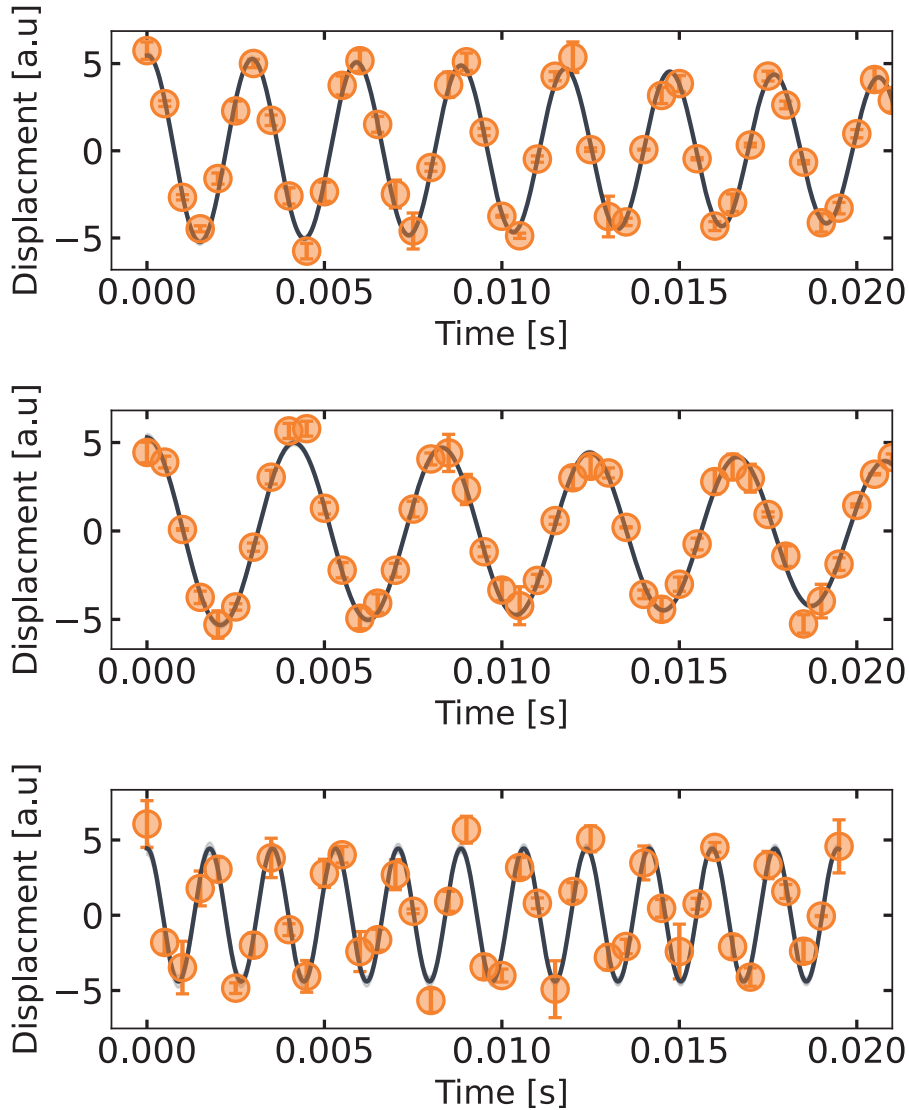


Figure 4.18. The trapping frequencies of the dipole trap with the new 50 W laser. The trapping frequencies in x (**Top**), y (**Middle**), z (**Bottom**) directions are extracted by fitting a damped sine wave to the positions of the cloud.

4.5.3 Power stabilisation of the trap

Both beams are power stabilised using 80 MHz AOMs. A small proportion of each beam near the science cell is reflected by a pick-off plate onto a photodiode. The

photodiode signal, along with a set-point given by the experimental control, is used by a PID controller to stabilise the intensity of the dipole beam. The power stabilisation provides a stable trap with a constant trap depth which is crucial for further cooling of the atoms in the dipole trap. During the change of the laser, the optical paths are realigned by using signals on the photodiode as an initial reference. Once the error signal approaches zero, the piezoelectric mirrors can be turned manually while looking for the initial signal of the atoms. After obtaining the first signal, fine scans can be carried out to optimise the signal. An example of atoms in the waveguide is given in Fig. 4.19.

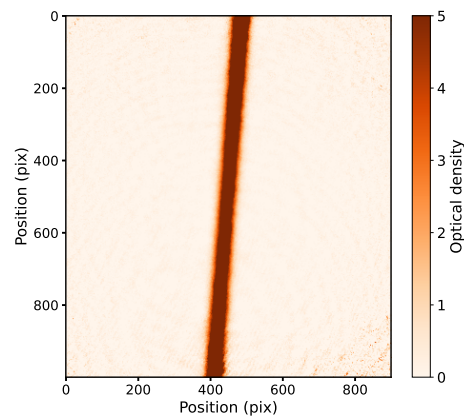


Figure 4.19. An example of around 2.3×10^6 atoms in the waveguide after the optimisation of the dipole trap.

4.6 Microwave and radio setup

The setup of the microwave (MW) and radio frequencies (RF) plays a key role in both achieving quantum degeneracy of both species and utilising the spin degrees of freedom. The setup has an output frequency range between 5 kHz and 4.4 GHz with 10 W maximum output power. A detailed description of the setup can be found in [95].

4.6.1 Frequency sources

Precise frequencies are needed to manipulate atoms in different hyperfine states, therefore a 10 MHz rubidium frequency reference is used as the frequency standard for the setup. As the main frequency sources for the setup, two DDS (Direct Digital Synthesis) boards and an adjustable microwave source based on a PLL (Phase Lock Loop) board are used. Both DDS boards are connected to a function generator

which outputs a 500 MHz signal. Both DDS boards can output between 300 kHz and 200 MHz with a frequency resolution below 1 Hz and a 14 bit phase resolution. One board has two outputs and the other one has four, which can all be controlled independently in terms of frequency, phase and power. The PLL board is used to synchronise the frequencies across the setup.

4.6.2 I/Q mixers

The limited bandwidth (200 MHz) of the DDS boards leads to an I/Q mixing scheme for higher frequency generation. A standard I/Q mixer takes in a fixed frequency f_0 and a changeable intermediate frequency f_1 , resulting in four output frequencies f_0 , f_1 , $f_- = f_0 - f_1$ and $f_+ = f_0 + f_1$. Different techniques can be implemented to suppress unwanted frequencies. In the scheme, two separate I/Q mixers are used for different frequency ranges, one for RF (50 MHz - 500 MHz) and the other for MW (800 MHz - 2000 MHz). The output power of the mixers are limited by the output power of the DDS boards, which is not sufficient to directly drive the transitions of atoms. To amplify the output for both channels, a two-stage amplification is implemented with a pre-amplifier and a final-stage amplifier. The amplifiers used on each channel are different due to the different frequency range. For frequencies below 50 MHz, a direct output of one of the DDS boards is used without the I/Q mixing scheme.

4.6.3 Antennas

To drive the atomic transitions, two separate loop antennas are used for RF and MW pulses respectively. An antenna is a loop of bare solid copper wires used in coaxial cables soldered with a connector which connects to an amplifier via coaxial cables. A large part of the power is reflected due to the antenna's impedance not being matched. The RF antenna is a rectangular loop with two windings which is placed at the top of the science cell against gravity. Direct couplings between the Zeeman sublevels are usually around 5 MHz which is realised using the RF antenna. The MW antenna on the other hand only has a single winding and a circular shape. The position of the MW antenna is also different from the RF one, at the front of the science cell perpendicular to gravity. The MW antenna plays a big role in cooling as well as coupling between different hyperfine states.

The position of the MW antenna is crucial for reliably producing Bose-Einstein condensates of both species during the evaporative cooling stage in the magnetic

trap. Small movements on the level of 1 mm would result in a difference in atom number in the magnetic trap by a factor of 10. The initial rough alignment of the MW antenna is usually carried out by moving the antenna incrementally and monitoring the atom number in the magnetic trap after the evaporative cooling. Further optimisation can be done using atoms in an optical lattice. Driving Rabi oscillations for atoms between $|1, 1\rangle$ and $|2, 2\rangle$ to maximise the Rabi frequency can be carried out by moving the position of the MW antenna.

4.6.4 Controlling the pulses

With all the necessary tools to generate the pulses with various frequencies, an Arduino DUE is used to control the setup. Each frequency ramp is written in ASCII format with four parameters, duration(μ s), start frequency (Hz), stop frequency (Hz) and amplitude (0-1000). As an example, a frequency sweep from 1900 MHz to 1800 MHz for 9 s with maximum output power is written as

```
rt900000F19000000000f18000000a1000z
```

where **r** and **z** are identified as the start and end of the ramp. All the ramps are pre-calculated and programmed at the beginning of each run by the Arduino. After the run is finished, the Arduino will reset automatically.

4.7 Imaging system

4.7.1 Absorption imaging

A commonly used technique for atomic detection is absorption imaging [96]. The idea behind absorption imaging is to let light which is on resonance with one of the atomic transitions pass through an atomic sample and then record the signal on a CCD camera. Since the light is on resonance, a certain amount of photons will be absorbed by the sample which results in a reduction in the intensity of the light in the region where the atomic sample is. The signal then can be used to calculate the properties such as atom number, temperature and density. For spinor gases used on the platform, both hyperfine ground states $F = 1$ and $F = 2$ can be detected by shining the repumping light for a very short amount of time. In the absence of the repumping light, only atoms in $F = 2$ are detected.

In total, 3 images are taken during a typical imaging sequence. The first image I_{atom} consists of the imaging beam, atoms and the background. The second image

I_{ref} consists of the imaging beam and background only. The last image I_{bg} only includes the background. The third picture is subtracted from the first and the second picture to remove the background noise,

$$I_1 = I_{atom} - I_{bg} \quad I_2 = I_{atom} - I_{bg} \quad (4.14)$$

The optical density is calculated using the two images I_1 and I_2 , along with the resonant scattering cross section σ_0 , the saturation intensity I_0^{sat} and the imaging constant α^* . The formula used to calculate the optical density is as follows,

$$OD(x, y) = -\frac{1}{\sigma_0} \left[\alpha^* \ln \left(\frac{I_2(x, y)}{I_1(x, y)} \right) + \frac{I_1(x, y) - I_2(x, y)}{I_0^{sat}} \right] \quad (4.15)$$

where $\sigma_0 = \frac{3\lambda^2}{2\pi}$. The imaging constant α^* is determined from experimental imperfections, polarisation, residual detuning etc. In the case of $I_1 \ll I_{sat}$, the optical density is dominated by the \ln term, therefore the second term can be neglected. When $I_1 \gg I_{sat}$, the intensity correction from the second term becomes significant and should be included in the calculation. Both α^* and I_{sat} have to be calibrated experimentally for each imaging system, and the calibration for the platforms are provided in [47]. The values obtained are given in table 4.3. The atom number for both species in the optical dipole trap can then be determined by summing the optical density in the corresponding regions.

specie	Saturation intensity I_0^{sat}	Magnification, M	Imaging constant α^*
Sodium	20.3/pix/ μ s	6.54 ± 0.04	3.6
Lithium	11.2/pix/ μ s	15.44 ± 0.12	3.1

Table 4.3. The obtained values from the imaging calibration carried out in [47] on the platform.

4.7.2 Optical setup

Atoms are imaged in the direction of gravity in the platform as the imaging light is shone from the top of the science cell. After passing through the atoms, the light is collected using an objective system built in-house before being recorded on a CCD camera. Both species share a common imaging path up to a dichroic mirror, where the imaging light for lithium passes through, and the imaging light for sodium is reflected, as shown in Fig. 4.20. Two independent CCD cameras are used on the platform, a Q-Imaging Retiga EXi for sodium and a HNü 512 EMCCD for lithium. The details of the setup can be found in [97].

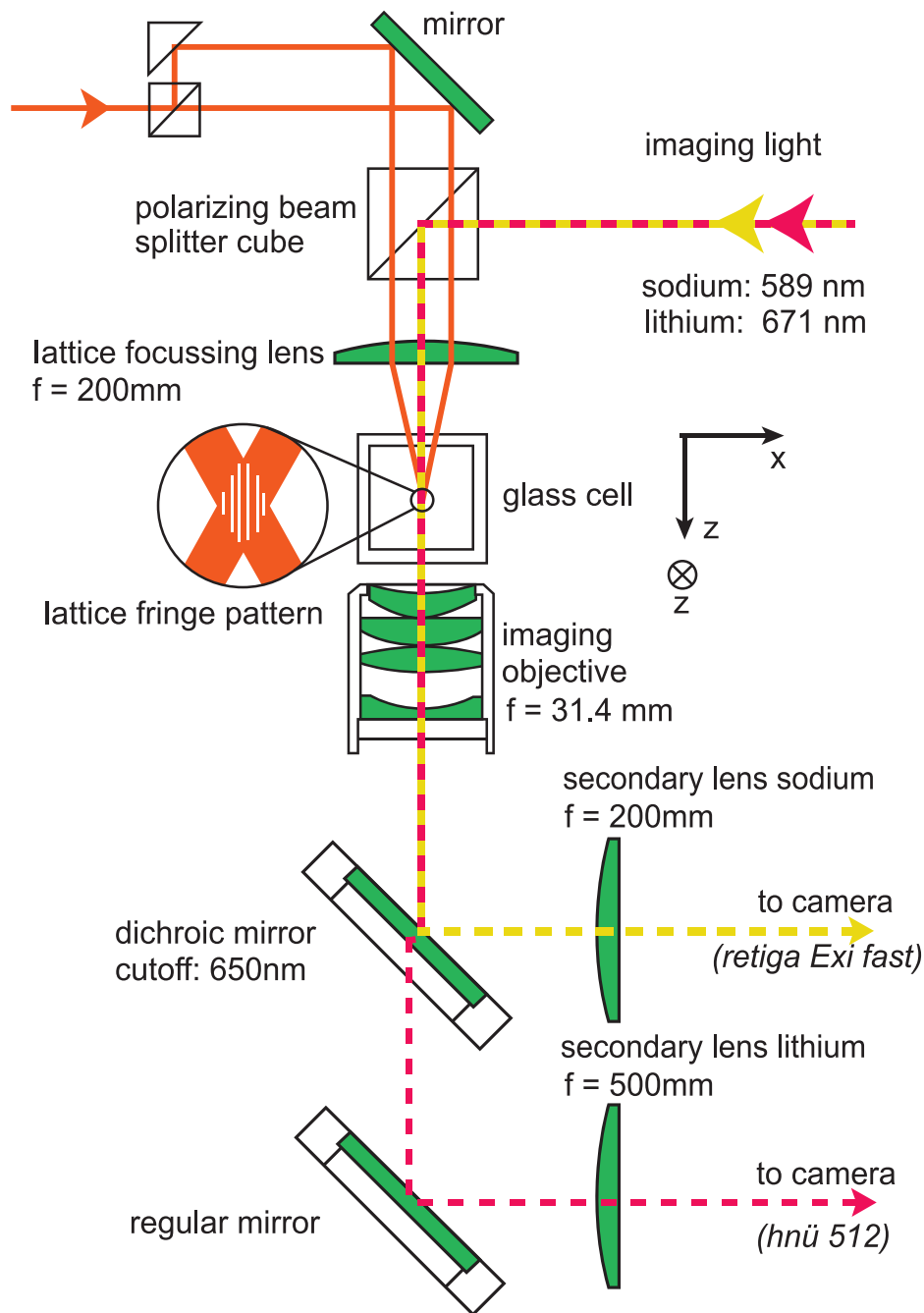


Figure 4.20. A schematic of the imaging setup used on the platform. Adapted from [47].

4.8 Experimental control system

4.8.1 Hardware for control

Four analogue output modules from National Instruments (NI) are used to control the experiment. Three PXI-6733 modules provide 24 analogue channels and 24 digital channels. The other PXI-6733 provides another 24 digital channels. Each ana-

logue channel can output between -10 and 10 V and each digital channel can output either 0 V or 5 V. Two-state (on/off) controlled devices like shutters and switches, which only take binary inputs, are controlled using digital channels. Other devices such as power supplies are controlled using analogue voltages. The four modules sit in a PXI-1033 chassis which provides all the necessary power and cooling. The communication between the control computer and the chassis is established using the Data Acquisition (DAQ) software from NI.

4.8.2 Software for control

Experiments on the platform are usually carried out in a series of stages. Each stage involves different components of the experiment at a specific time, therefore sequences need to be pre-programmed to accomplish the tasks. Moreover, a clock is needed to synchronise each module in the chassis. The control software used was based on MATLAB. All the instructions for controlling the experiment are edited and compiled using a self-developed editor known as SDFF. The details of SDFF can be found in [98]. The control system provided all the necessary features needed for controlling the platform, with some drawbacks. The clock used for the control system has a constant rate which makes compiling the experimental sequence very slow when pulses with a very short duration are needed. In order to reduce the turnover time between the shots, a new experimental control system known as the labscript suite was implemented.

The labscript suite was developed for controlling ultracold quantum gas experiments [99–101]. The framework is based on Python and consists of six modules which can be divided into three categories, preparation, execution and analysis as shown in Fig. 4.21. An FPGA based pseudoclock clock (Opal Kelly XEM3001) serves as the master clock of the system which reduces the compiling time of the sequence significantly compared to the old control system.

For the preparation, the connection table defines all the necessary connections between the hardware and the control system. The experimental sequence is placed in a python file named `Experimental.py` which can be modified to accommodate different needs. Runmanager serves as a graphical user interface for changing the values of global parameters quickly without modifying the experimental sequence file every time. The files for the experimental sequence and the connection table are compiled before being sent to BLACS for execution.

BLACS is the bridge that connects the experimental sequence and the hardware. One advantage of the labscript suite is the ability to integrate new devices

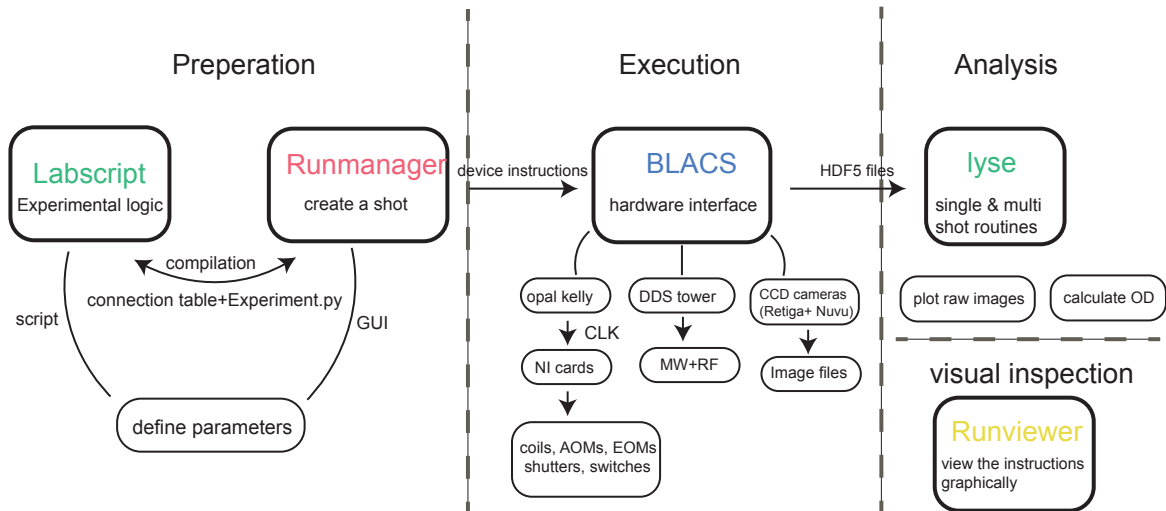


Figure 4.21. The modules involved in the labscript suite framework. Taken from [91].

such as arbitrary waveform generators and cameras into BLACS. The microwave and RF system and two cameras have been integrated into BLACS over the course of this thesis. Users can also manually change the output of each individual channel via BLACS for debugging.

The data acquired on the platform via cameras saved in the form of HDF5 is transmitted to Lyse for visual inspection. Lyse is used to plot the quantities of interest for users to carry out the necessary data analysis. For debugging, it is often useful to check the values of certain channels during a shot which can be seen using Runviewer.

4.9 Experimental sequence for double BECs

A typical sequence used in the platform to generate two BECs for sodium and lithium is given below. Roughly 50 s is needed for both species to reach quantum degeneracy.

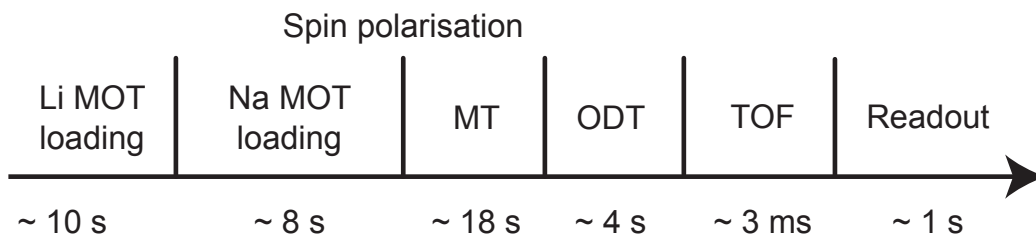


Figure 4.22. The stages involved to achieve quantum degeneracy in the platform.

4.9.1 MOT stage

During this stage, the Zeeman slower is switched on to slow down the atoms from the atomic source. The lithium MOT is loaded for 10 s before the sodium MOT gets loaded for 8 s while the laser light for lithium is kept on. The magnetic fields needed for the MOTs are provided through a combination of the curvature and offset coils. Once the loading stage is finished, the atomic beam shutter next to the atomic source is closed to reduce the pressure in the science cell region, and the light for the Zeeman slower is also blocked by the optical table.

In order to monitor the MOTs loading during a shot, a MAKO G-030B camera from Allied Vision is mounted around 30 cm above the science cell. The camera is integrated into BLACS so that it takes a picture during the loading stage. The image is saved in the corresponding HDF5 file which can be used for analysis. The image of the MOT is also plotted along with the usual atom image for a quick visual inspection when the experimental run is finished, as shown in Fig. 4.23

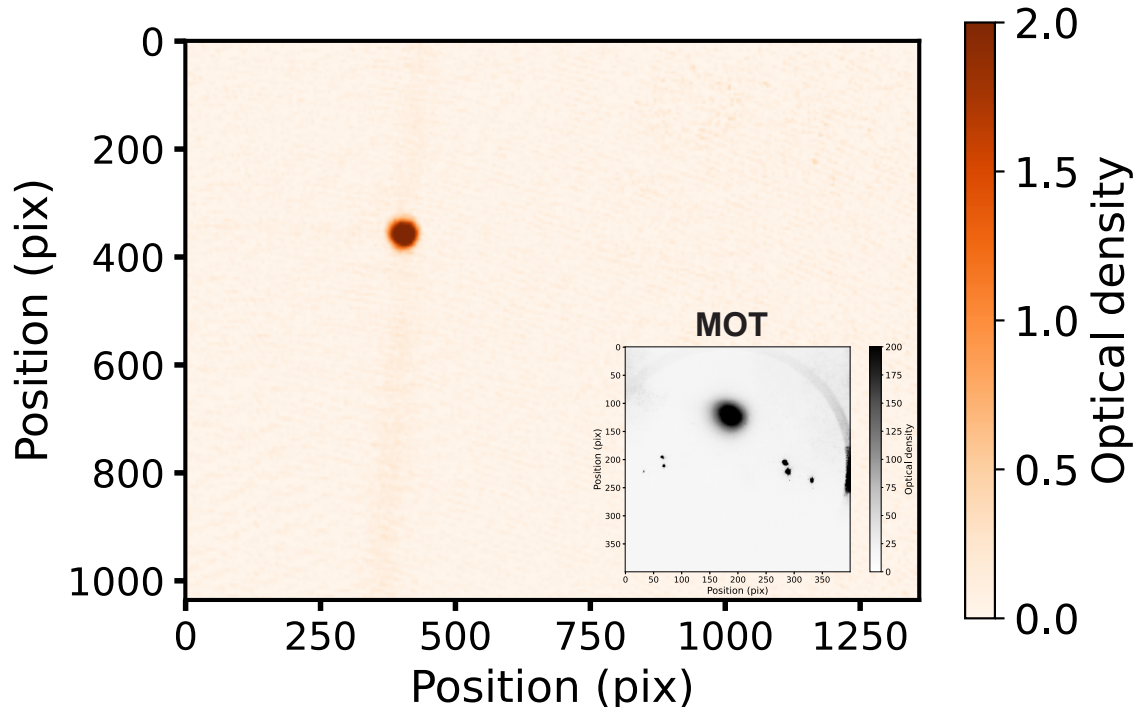


Figure 4.23. A typical shot of sodium obtained on the platform. During the MOT loading stage, an image of the MOT is taken by a MAKO camera.

4.9.2 Spin-polarisation stage

After both MOTs are loaded, a spin polarisation scheme is used to transfer most atoms into $|2, 2\rangle$ for both sodium and lithium. This is carried out by ramping the magnetic field up to 20 G using the bias coils and applying an optical pumping scheme using the umpump light and umpump repumper light. The process usually takes $600 \mu\text{s}$.

4.9.3 Magnetic trap and evaporative cooling stage

Atoms are then transferred into the magnetic trap by ramping up the currents of the curvature, gradient and bias coils. The transfer takes 3 ms. The magnetic fields are set to trap the atoms in $|2, 2\rangle$ for both species. There is still an amount of atoms in $|2, 1\rangle$ which leads to heating of the sample. A microwave pulse is used to clean the unwanted atoms in the state of $|2, 1\rangle$ by coupling them into untrapped states $|1, 1\rangle$ and $|1, 0\rangle$. The microwave pulses sweeps from 1870 MHz to 1810 MHz for 500 ms.

To further cool atoms down in the magnetic trap, two evaporative cooling pulses are provided consecutively. The transition used is from $|2, 2\rangle$ to $|1, 1\rangle$. The first pulse sweeps from 1900 MHz to 1800 MHz and the second one is from 1800 MHz to 1776 MHz. Each pulse lasts 9 s. The end point of the second pulse needs to be adjusted on a daily basis due to the fluctuation of the magnetic field. After the cooling, atoms are around $1 \mu\text{K}$ in the magnetic trap.

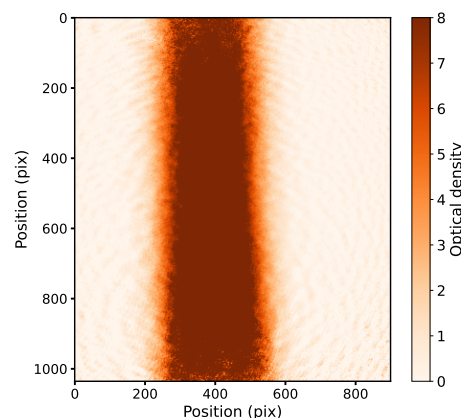


Figure 4.24. An example of the magnetic trap with 1.6×10^7 atoms after evaporative cooling. Only a part of the magnetic trap is imaged due to the high magnification of the imaging system.

4.9.4 Optical dipole trap stage

Atoms are first loaded into the waveguide path of the dipole trap by reducing the confinement from the magnetic trap and increasing the power of the waveguide beam to 10 W. The waveguide is located slightly below the magnetic trap so that atoms can fall into the waveguide. Atoms in $|2, 2\rangle$ have a much higher three-body loss rate which leads to a short lifetime in the trap [102]. Atoms are then transferred to $|1, 1\rangle$ using rapid adiabatic passage [103]. A microwave sweep is applied for 500 ms with a frequency of 1778 MHz and a range of 1 MHz. The frequency is calculated for a magnetic field of 2 G using the Breit-Rabi formula and the magnetic field is provided by using the offset coils and is actively stabilised through a feedback loop. The transfer efficiency is around 70 % for the process.

The dimple beam is then switched on to form a cross dipole trap and the atoms are trapped in the intersection region of both beams. To finally condense the trapped atoms, evaporative cooling occurs by reducing the intensity of the waveguide beam slowly from 10 W to 800 mW in 5 s.

4.9.5 TOF and readout stage

To image BECs, absorption imaging is used with the setup described in Section 4.20. In-situ profiles are usually not reliable for measuring properties of BECs due to the high optical density. Time of flight (TOF) measurements are carried out by switching off the dipole trap which leads to the free expansions of atomic clouds. Properties such as atomic density and temperature can be obtained through TOF measurements.

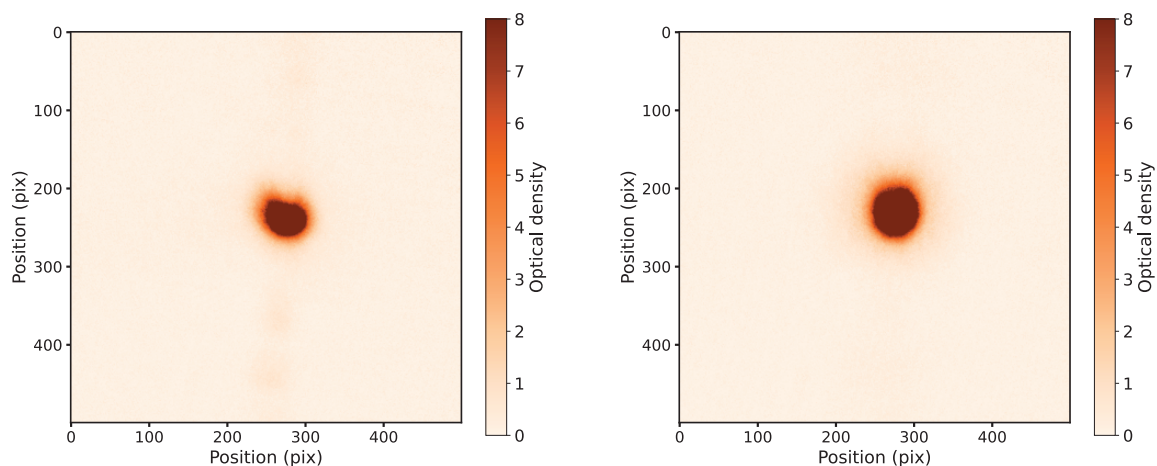


Figure 4.25. A comparison between two profiles of a sodium BEC. **Left:** An in-situ profile of a BEC. **Right:** A TOF profile (3 ms) of a BEC with 6.27×10^5 atoms.

The cloud is imaged after TOF with absorption imaging. Three pictures are taken during the process. The duration of the imaging pulse can be varied depending on the atomic cloud, typically $25\ \mu\text{s}$ is used to image BECs in the platform. The intervals between the pictures are given by 200 ms and 400 ms.

5 Characterisation of the platform

This chapter describes the main improvements carried out on the platform in the course of this thesis. The stability of producing BECs consistently is improved by improving several different stages of the cooling sequence. In order to be able to manipulate atoms in different magnetic substates, a new magnetic field stabilisation setup was installed on the system. For a tighter confinement and local control, an optical lattice setup described in [84, 104] was modified and the coherent manipulation of atoms inside the lattice is managed. Work towards single atom counting in a MOT with fluorescence imaging was also carried out.

5.1 Stability of atomic sample production

To be able to produce Bose-Einstein condensates reliably for both species is beneficial for simulating new physics as well as improving the existing setup. Given lithium atoms are sympathetically cooled in the magnetic trap via collisions with sodium atoms, a relatively small fluctuation in sodium atom number leads to a drastic change in lithium atom number in condensates. Moreover, an extensive statistical analysis was carried out on the project of the dynamic gauge field which indicates a dependence on the atom number of the model [91]. Given the cooling process is divided into several stages, it is intuitive to evaluate each stage separately.

The fluctuation of a sample can be quantified by using the coefficient of variation which is defined as the following,

$$c_v = \frac{\sigma}{\mu} \quad (5.1)$$

where μ and σ is the mean and standard deviation of the sample.

Given the high optical density of a sodium MOT on the platform, it is difficult to evaluate the atom number precisely with absorption imaging, therefore the fluorescence of the MOT is measured using the MAKO camera mounted on top of the science cell. The magnetic trap is chosen to be the starting point of the optimisation. The improvement both on the atom number and fluctuations can be seen in

Fig. 5.1. The main changes include the realignments of several optical paths such as the Zeeman slower beam and spectroscopy setup. The intensity stabilisation of the MOT path is also introduced which reduces the fluctuations. The 1.7 GHz frequency-shifter remains one of the bottlenecks of the experiment. The first order diffraction efficiency is around 5 % and reduces on a daily basis which worsens the performances of the MOT and spin-polarisation. Given the small aperture (75 μm) of the frequency-shifter, a 75 mm lens was used to focus the beam onto the aperture. This lens has been replaced by a 150 mm lens to reduce the sensitivity of the alignment which helps to improve the efficiency by up to 8 %. As a result, the average atom number in the magnetic trap is increased by 30 % and the fluctuations (c_v) are reduced from 25 % to 15 %.

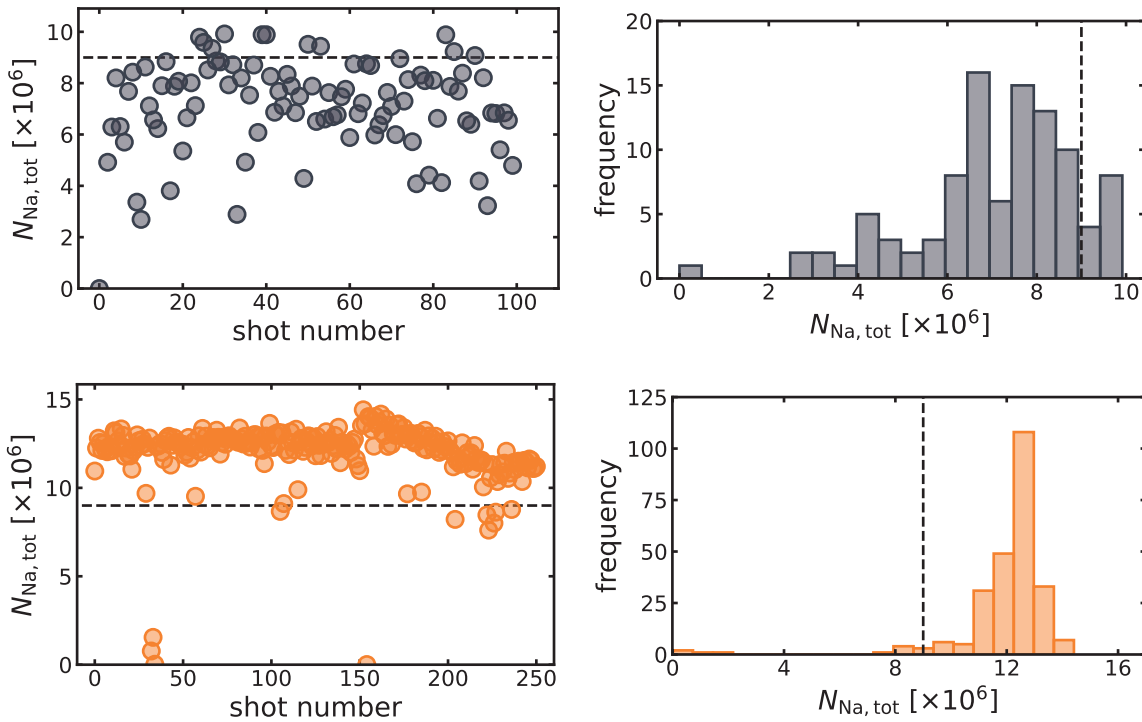


Figure 5.1. The atom number fluctuations in the magnetic trap before (**Top**) and after (**Bottom**) the optimisation. The fluctuations quantified by c_v is 25 % and 15 % before and after the optimisation. The dashed lines indicate the minimum amount of atoms required for loading into the optical dipole trap.

The next stage is the waveguide path of the dipole trap. Given the dipole laser was changed over the course of this thesis, the optical alignment was redone while keeping the same beam waists as before for both beams. However, the power of both the laser beams increased by 50 % which led to an increase in trapping frequencies by 20 %.

The increase in power leads to a higher stability of loading in the waveguide with a reduction of the coefficient of variation from 50 % to 15 %, as shown in Fig. 5.2. Atoms can be condensed in the waveguide alone after the optimisation with a typical condensate fraction η of 0.7 compared to a thermal cloud before the optimisation. To extract the condensate fraction, the density profiles are fitted with a Thomas–Fermi profile, the thermal profile and a sum of both which can be seen in Fig. 5.3.

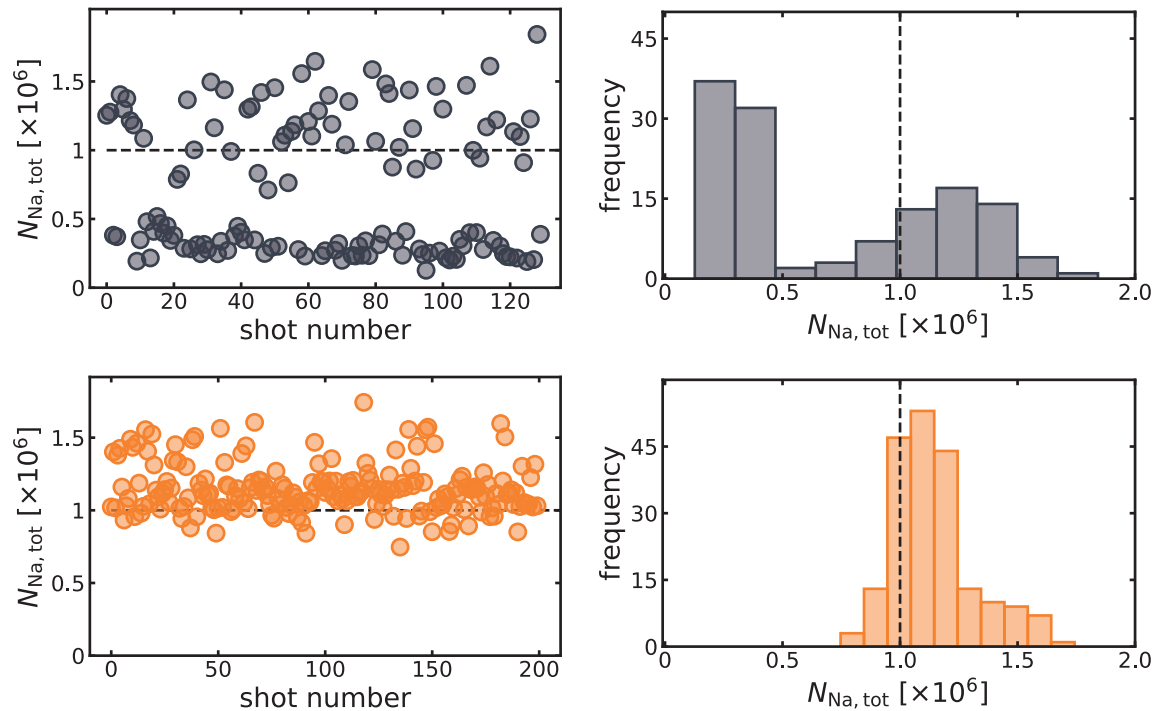


Figure 5.2. The atom number fluctuations in the waveguide before (**Top**) and after (**Bottom**) the optimisation. The fluctuations quantified by c_v are 50 % and 15 % before and after the optimisation. The dashed lines indicate the minimum amount of atoms required for crossing the dipole beams.

The last stage is managed by ramping up the second dimple beam of the dipole trap; given atoms are already reasonably cold in the waveguide, the additional beams help to increase the condensate fraction even further to $\eta = 0.81$. Similarly, the atom number in the cross-dipole trap is improved with the mean atom number increased from 3.05×10^5 to 4.1×10^5 . The fluctuation (c_v) on the other hand is reduced from 18.6 % to 9 %.

5.2 Internal states manipulation

Coherent manipulation of both species via their internal states is an important tool for the platform. To fully utilise the spin degree of freedom with the Zeeman shift,

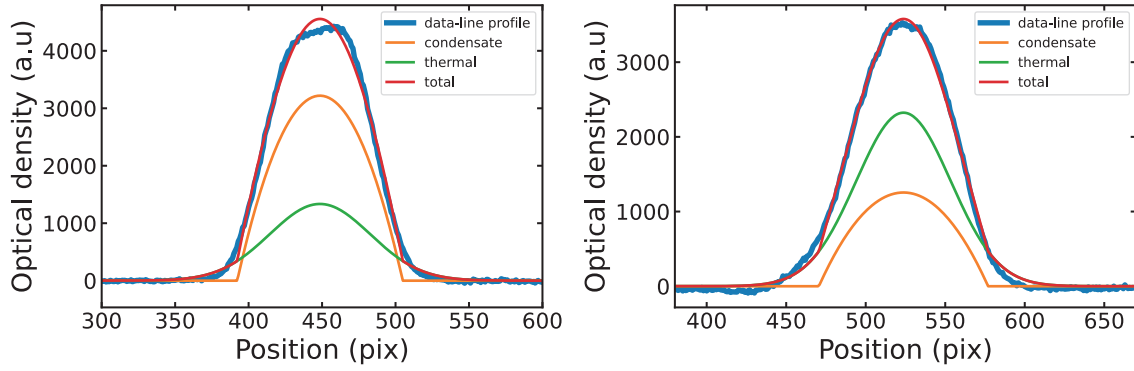


Figure 5.3. The density profiles of atoms in the waveguide. A condensate fraction η of 0.71 (**Left**) is achieved after the optimisation compared to $\eta = 0.32$ before (**Right**).

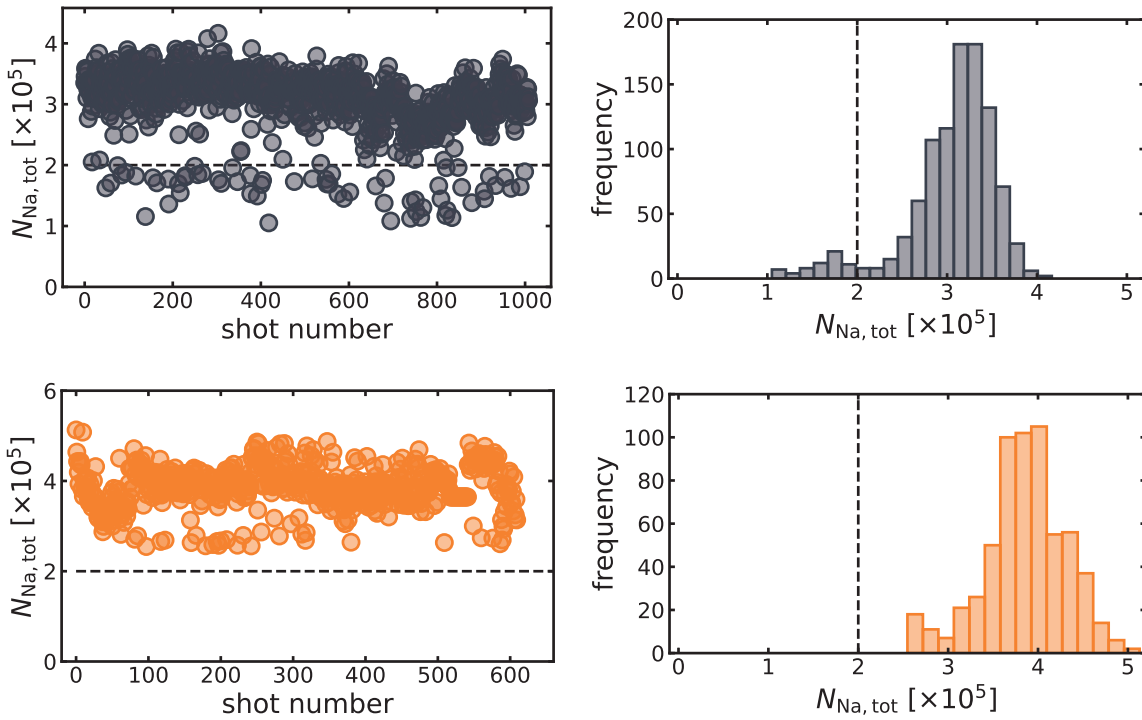


Figure 5.4. The atom number fluctuations in the cross-dipole trap before (**Top**) and after (**Bottom**) the optimisation. The fluctuations quantified by c_v is 18.6% and 9% before and after the optimisation. The dashed lines indicate the minimum amount of atoms required for carrying out simulation or computation tasks.

precise control of the offset magnetic field is needed. By applying an offset magnetic field, the energy differences between magnetic substates can be calculated using Eqn. 3.8. Sodium atoms are used to understand the magnetic field fluctuations on this platform given there are fewer atom number fluctuations compared to lithium. For sodium atoms in $|F = 1\rangle$ and $|F = 2\rangle$ hyperfine manifolds, the Zeeman shift due

to a small magnetic field \mathbf{B} up to the second order is given by,

$$\Delta E \approx pm_F |\mathbf{B}| + q(4 - m_F^2) |\mathbf{B}|^2 \quad (5.2)$$

where

$$p = \pm \left(\frac{g_J - g_I}{4} \pm g_I \right) \mu_B \approx \begin{cases} +699.583 \text{ kHz G}^{-1} & F = 2 \\ -702.369 \text{ kHz G}^{-1} & F = 1 \end{cases} \quad (5.3)$$

$$q = \pm \left(\frac{g_J - g_I}{4} \right)^2 \frac{\mu_B^2}{E_{hfs}} \approx \pm 138.65 \text{ Hz/G}^2 \quad (5.4)$$

For hyperfine transitions between $|F = 1, m_F\rangle$ and $|F = 2, m'_F\rangle$, the change in the transition frequency due to the Zeeman shift is given by

$$\Delta f = 2\pi \times (m_F + m'_F) \times 0.71 \frac{\text{kHz}}{\text{mG}} \quad (5.5)$$

Given the transition between $|1, 1\rangle$ and $|2, 2\rangle$ is 3 times more sensitive to magnetic field fluctuations compared to the transition between $|1, 1\rangle$ and $|2, 0\rangle$, the transition is used to calibrate the offset magnetic field of the platform.

On the platform, different magnetic substates can be coupled via microwave or RF pulses. By applying a microwave pulse of certain duration, a certain amount of atoms is transferred to the other state, Rabi oscillations between $|1, 1\rangle$ and $|2, 2\rangle$ can be observed by varying the pulse duration t_{Rabi} as shown in Figure.5.5. The ratio of the population difference between the two coupled states N_{diff} and population sum N_{total} is plotted as a function of the microwave duration t_{Rabi} . To quantify the oscillations, a function $f(t)$ is used to fit the experimental data.

$$f(t) = O + A \times \cos(\Omega' t + \phi) \times e^{-t/\tau} \quad (5.6)$$

where $A = \frac{\Omega^2}{\Omega'^2}$ is the amplitude of the oscillation, Ω' is the effective Rabi frequency and ϕ is the phase. Factors such as fluctuations in the offset magnetic field and microwave power contribute to the dephasing process, therefore an exponential decay function with a decay constant τ is used to quantify the effect of dephasing. The Rabi frequency Ω and detuning Δ can be calculated using the following equations,

$$\Omega = \sqrt{A \times \Omega'^2} \quad (5.7)$$

$$\Delta = \sqrt{\Omega'^2 - \Omega^2} \quad (5.8)$$

In the ideal case without any technical fluctuations, the Rabi oscillations can be characterised using the Rabi frequency Ω and the detuning Δ which stay constant during the oscillations. The magnetic field and the microwave power fluctuations

play as the two main parts in the dephasing of the Rabi oscillations on the platform. As Rabi frequencies Ω are proportional to the square root of MW power, the fluctuations in power result the Rabi frequencies changing. On the other hand, fluctuations in magnetic fields shift resonance frequencies according to Equation 5.5, leading to changes in the detuning Δ . Fluctuations in both parameters contribute to the dephasing of the Rabi cycles with a reduced decay constant τ . Typical free Rabi oscillations between $|F = 1, m_F = 1\rangle$ and $|F = 2, m_F = 2\rangle$ without any stabilisation are presented with a dephasing time of $0.43(12)$ ms in Figure.5.5.

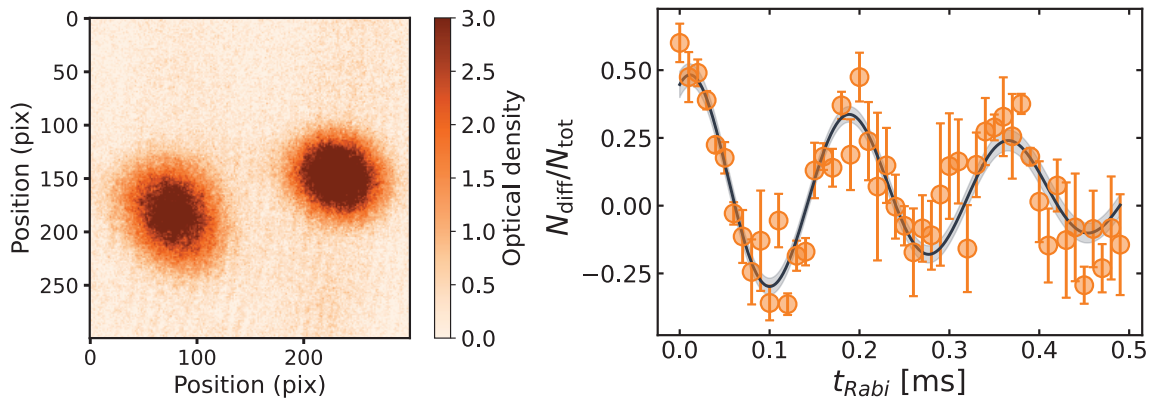


Figure 5.5. Left: a single realisation of Rabi Oscillations between $|F = 1, m_F = 1\rangle$ and $|F = 2, m_F = 2\rangle$. Atoms in the two different states are separated by using a Stern Gerlach pulse. **Right:** The population difference Rabi oscillations between $|F = 1, m_F = 1\rangle$ and $|F = 2, m_F = 2\rangle$ without activate magnetic stabilisation. The ratio of the population difference between the two coupled states N_{diff} and population sum N_{total} is plotted as a function of the microwave duration t_{Rabi} . A dephasing time of $0.43(12)$ ms can be obtained by fitting the data.

It is also important to distinguish between the different timescales of the fluctuations of the parameters. These can be categorised into shot-to-shot fluctuations and long-term drifts due to effects such as the temperature. A simple toy model is used to help understand the effects of shot-to-shot fluctuations in magnetic fields and microwave and radio power on the Rabi cycles. Long term drifts can be characterised by preparing a coherent spin state with an equal-superposition of $|F = 1, m_F = 1\rangle$ and $|F = 2, m_F = 2\rangle$ and measuring the population imbalance for several hours.

5.2.1 A toy model for magnetic field fluctuations

The toy model uses Monte Carlo methods which rely on repeated random sampling from certain distributions for both the Rabi frequency Ω and the detuning Δ . The

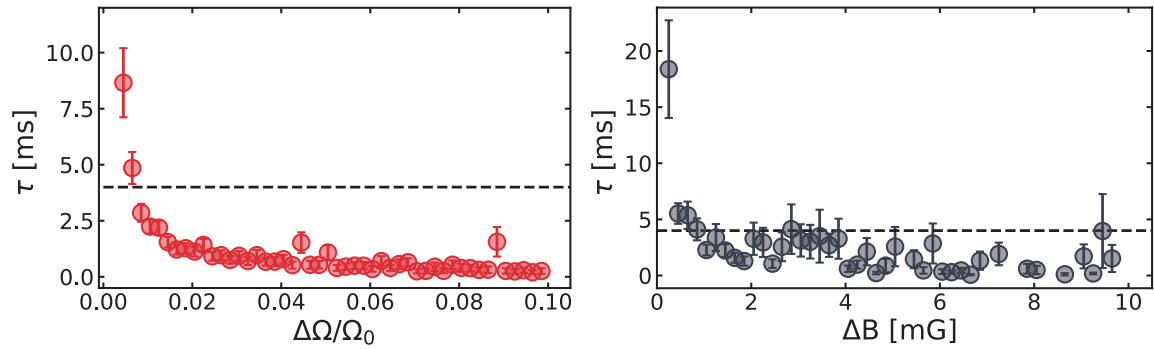


Figure 5.6. The dephasing time τ extracted as a function of both the magnetic field fluctuations (black) and MW power fluctuations (red) respectively. The data used to extract the dephasing time τ is generated using the toy model with the Rabi frequency $\Omega = 2\pi \times 8$ kHz and the detuning $\Delta = 2\pi \times 0$ kHz. The dashed lines indicates the dephasing time extracted from the experimental platform.

output data from the model is fitted with Equation 5.6.

To understand the effect of MW power fluctuations qualitatively, it is assumed the Rabi frequency follows a Gaussian distribution $\Omega \sim \mathcal{N}(\Omega_0, \sigma^2)$, with $\Omega_0 = 2\pi \times 8$ kHz and σ varies from 0.1% to 5% Ω_0 . Similarly, magnetic fluctuations can be simulated by assuming $\Delta \sim \mathcal{N}(\Delta_0, \sigma^2)$, with $\Delta_0 = 2\pi \times 0$ kHz and σ varies from $2\pi \times 0.1065$ kHz (50 μ G) to $2\pi \times 10.65$ kHz (5 mG). Rabi oscillations are simulated up to 5 ms for each parameter independently while setting the fluctuations in the other parameters to zero. 1×10^4 samples are generated for each value of the parameter with a step size of 0.02 ms (Fig.5.7).

Qualitatively, the dephasing time decreases as the fluctuations increase for both parameters. However, the Rabi oscillations behave differently at longer timescales (5 ms) for the two parameters. To gain a more intuitive idea of the contribution to the dephasing process from different levels of fluctuations in each parameter, the dephasing time is extracted from the Rabi oscillations with different levels of fluctuations in each parameter. At each fluctuation level, 1×10^4 samples of the Rabi cycles up to 5 ms was simulated and fitted to obtain the dephasing time. The results obtained are shown in Fig.5.6. For MW power fluctuations, a clear trend of reduction in the dephasing time can be observed as the fluctuation increases. The same overall trend can also be observed in the case of magnetic field fluctuations but with larger standard errors.

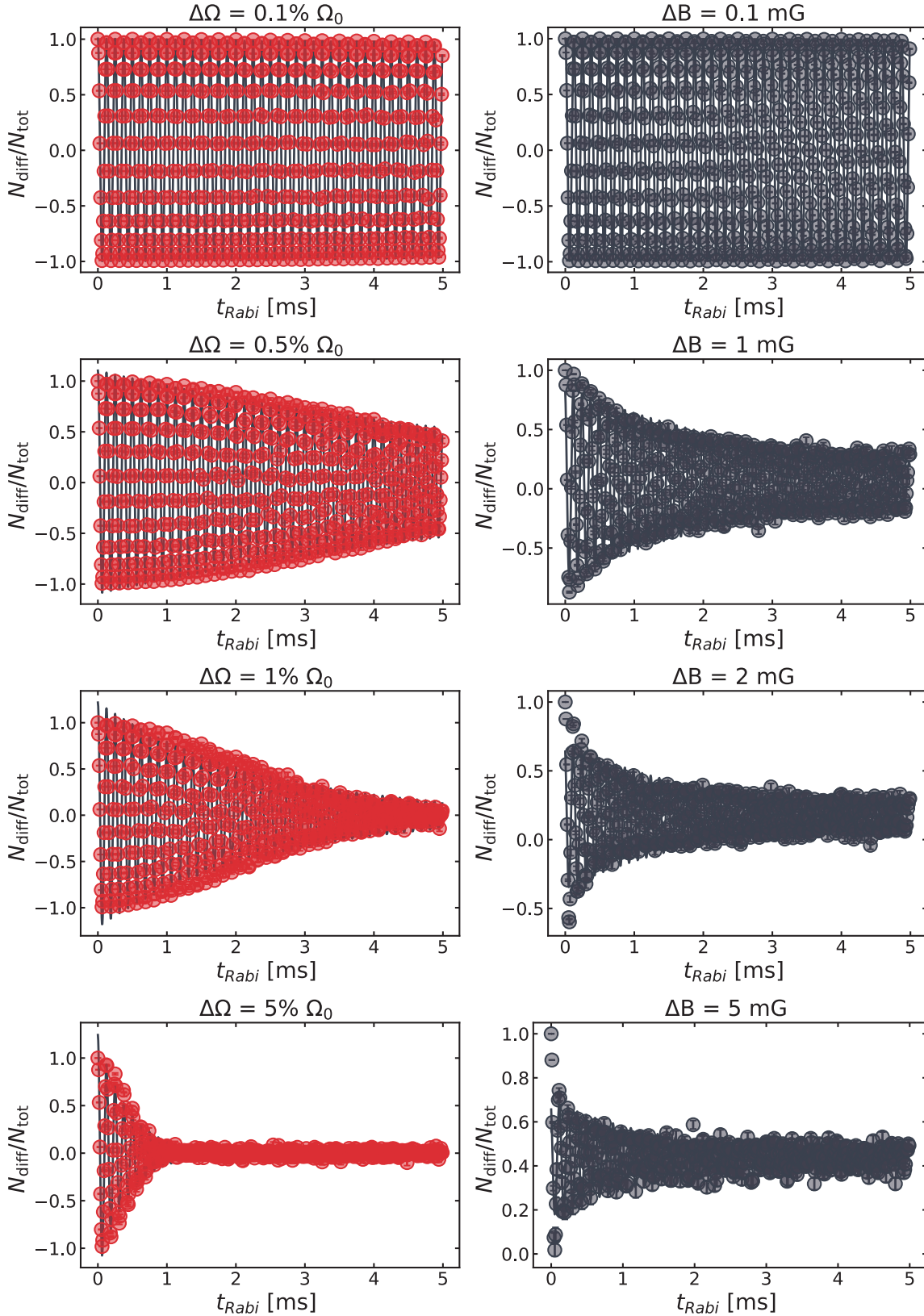


Figure 5.7. Simulated Rabi oscillation between $|F = 1, m_F = 1\rangle$ and $|F = 2, m_F = 2\rangle$ for both the magnetic field fluctuations (**black**) and MW power fluctuations (**red**). To generate both sets of data, the Rabi frequency is set to be $\Omega = 2\pi \times 8$ kHz and the detuning is set to be $\Delta = 2\pi \times 0$ kHz

5.2.2 Stabilisation scheme

The general idea behind the stabilisation scheme is demonstrated in Fig.5.8. The input signal from the fluxgate sensor is subtracted by a reference voltage and then amplified using a home-built circuit. The amplified signal is then fed into a PID controller along with a set-point provided externally via the experimental control, and the output of the PID is used to control the power supply which regulates the magnetic field.

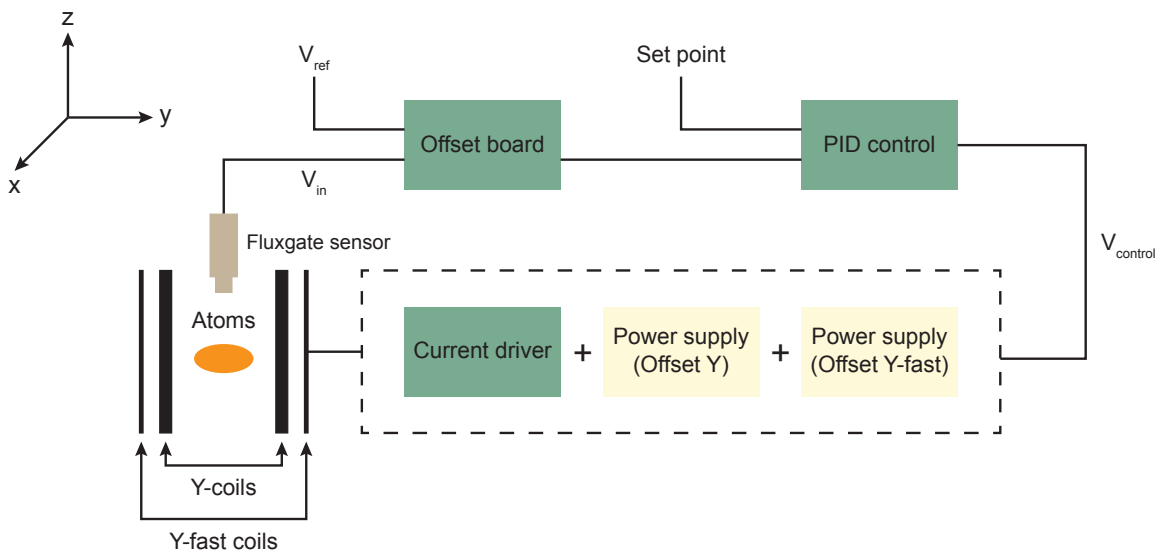


Figure 5.8. The magnetic field stabilisation scheme used in the platform. Adapted from [91].

The magnetic field required is generated by three sets of offset coils. Two sets are responsible for the magnetic field in the direction of the Zeeman slower beam, the Y-coil and Y-fast-coil. The other set is responsible for the magnetic field in the direction of gravity, known as the Z-coil. Each pair of coils are connected to a power supply which can be controlled using an analogue voltage provided by the experimental control. The offset magnetic field is generated by using a combination of Y and Z-coils, and the Y-fast coil is used to actively regulate the magnetic field.

To measure the magnetic field next to the science cell, a three-axis magnetic field sensor (Bartington MAG-03MS1000) is placed directly in front of the glass cell. The sensor can measure the magnetic field in three perpendicular axes with a range between -10 and 10 G, with an extremely low measurement noise floor $60 \text{ nG}/\sqrt{\text{Hz}}$ at 1 Hz. The fluxgate sensor outputs three separate voltages which scales linearly with the magnetic fields in the corresponding directions, with the scaling factor being 1 V G^{-1} for the model used in the platform. Only the magnetic field in the Zeeman

slower (Y) direction is measured and regulated.

The regulating bandwidth of a set of coils connected to a power supply is limited by the inductance of the coil and the output capacity of the power supply. For the Y and Y-fast coils, the bandwidths are measured to be around 30 Hz and 90 Hz respectively. To regulate high-frequency noises away, the output capacity of the power supply needs to be reduced. A circuit serving as a voltage controlled current source is used for this purpose, with the design based on the work in [105, 106].

The current source regulates the current through a feedback loop by using an operational amplifier (OP 27). The OP 27 takes a control voltage as the set-point and the measured signal is provided by the voltage drop across a high power resistor (R5) which acts like a shunt resistor. The output of the OP 27 flows through a Darlington transistor (MJ11032) which regulates the current flowing through the coils. The value of the shunt resistor (R5) determines the conversion factor between voltage and current which is chosen to be 1Ω .

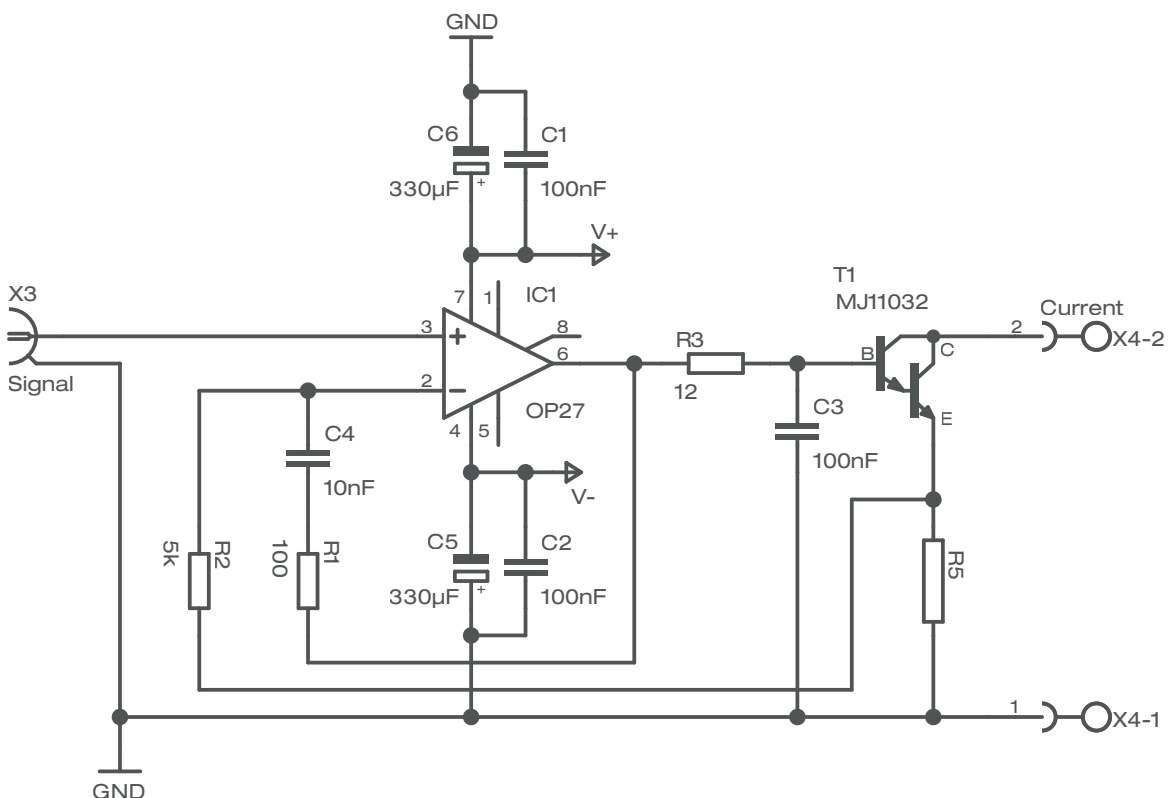


Figure 5.9. The circuit diagram of the voltage controlled current source used in the platform. Taken from [105].

The bandwidth of the current controller is set by a low pass filter which consists of a resistor (R3) and a capacitor (C3). The maximum regulating current of a single current controller is 10 A. For applications requiring a higher current, several

identical controllers can be connected.

The old stabilisation scheme was implemented as described in [107]. The reference voltage is provided using a 20 bit digital-to-analog converter (AD5791). The amplification is provided by a single-channel, 1024-position digital potentiometer (AD5293). Both the reference voltage and the amplification factor can be controlled using an Arduino. Additionally, an opto-isolator is also included in the setup to protect the high-precision components. A PCB board is used to host all the components mentioned above.

Soldering and debugging of the PCB board, however, is difficult due to the compact size and complexity of the layout. Therefore, a simplified circuit is used to replace the old setup in the experimental platform while keeping the same overall stabilisation scheme. In the new setup shown in Fig.5.10, the measured voltage from the fluxgate sensor is subtracted by a reference voltage. The reference voltage is provided by a high precision, dual-tracking reference (AD588) and a 25-turn manual potentiometer is used to vary the reference voltage. The amplification is carried out by a precision instrumentation amplifier (AD-524N). The amplification factor of the amplifier is fixed to either 10, 100 or 1000 by moving the jumper at SV3. The new design reduces the complexity of the board for easy assembling and debugging, and can also be used for other high-precision applications such as microwave and radio power stabilisation.

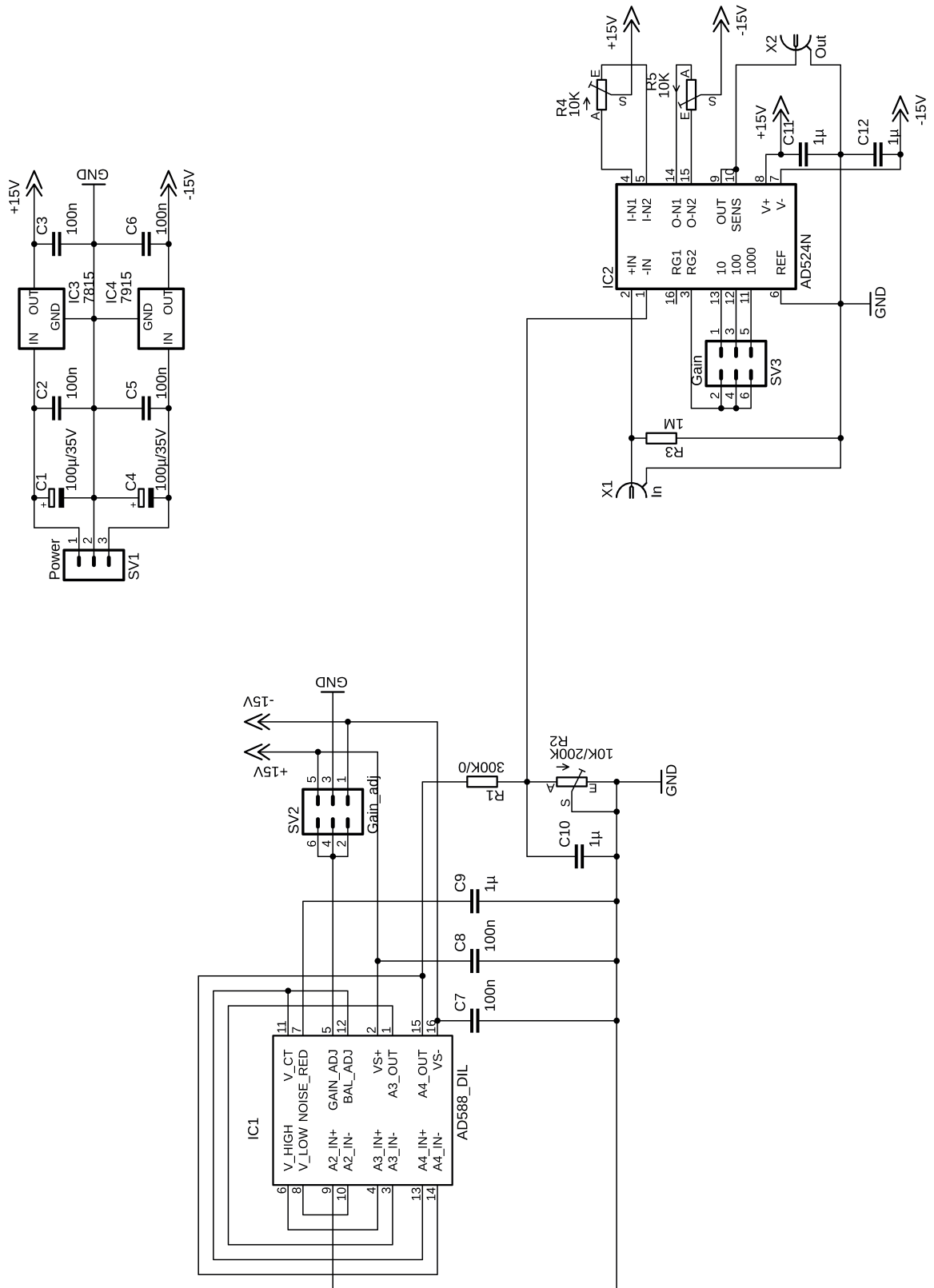


Figure 5.10. The circuit diagram of the new stabilisation board. The reference voltage provided by AD588 can be varied using the manual potentiometer (R2). The amplification is managed by AD542N. The amplification factor can be changed from 10, 100 and 1000 by changing the jumper at SV3

5.2.3 Rabi oscillations with stabilisation

To compare the old and new stabilisation setup, Rabi cycles were carried out using the same transition ($|F = 1, m_F = 1\rangle$ to $|F = 2, m_F = 2\rangle$) around 2 G as shown in Fig.5.11. The dephasing time is increased by a factor of 2 with the new setup. By assuming the fluctuation is from the MW power or the magnetic field only, estimations can be made of the magnitude of the fluctuations using the simple toy model. If the dephasing is caused by the MW power fluctuations only, by comparing a dephasing time of 3.36(62) ms obtained from the experiment to the simulation, the power fluctuation of the MW setup can be bounded between 0.5 % and 1 %. However, no estimation of the magnetic field fluctuations is feasible due to the large standard errors predicted by the toy model on the transition alone.

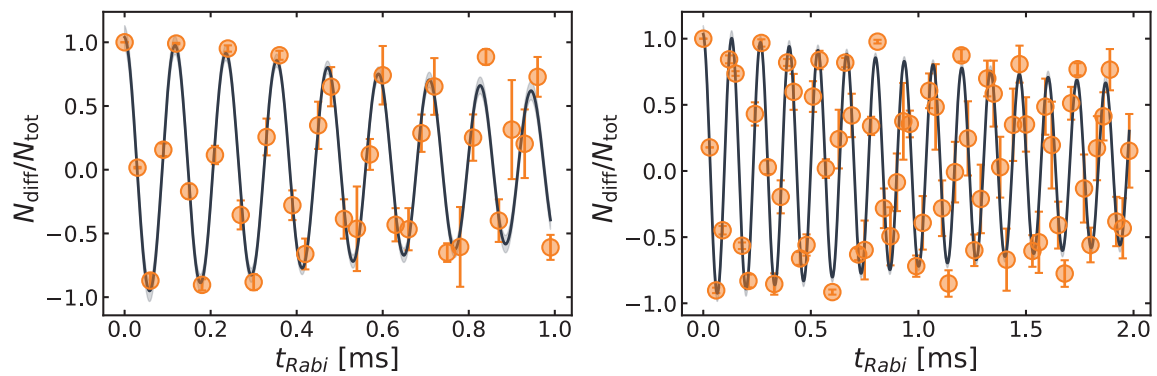


Figure 5.11. Rabi oscillations between $|F = 1, m_F = 1\rangle$ and $|F = 2, m_F = 2\rangle$ with activate magnetic stabilisation. **Left:** fringes obtained with the old setup with a dephasing time of 1.72(26) ms. **Right:** fringes obtained with the new setup with a dephasing time of $2\pi \times 3.36(62)$ ms.

A second transition from $|1, 1\rangle$ to $|2, 0\rangle$ is used to help estimate the magnetic field fluctuations. The change in frequency $\Delta f = 2\pi \times 0.71 \text{ kHz mG}^{-1}$ is a factor of 3 smaller than $|1, 1\rangle$ to $|2, 2\rangle$ ($2\pi \times 2.13 \text{ kHz mG}^{-1}$). By repeating the Rabi cycle using this transition, a dephasing time of 10.2(34) ms is obtained. A similar simulation based on the toy model with the same transition is carried out, taking into consideration the lifetime of $|2, 0\rangle$ which is measured to be 15.3(21) ms. As shown in Fig.5.13, a similar bound can be obtained for the magnetic field fluctuation which is given as $\Delta B \in [0.7 \text{ mG}, 0.9 \text{ mG}]$.

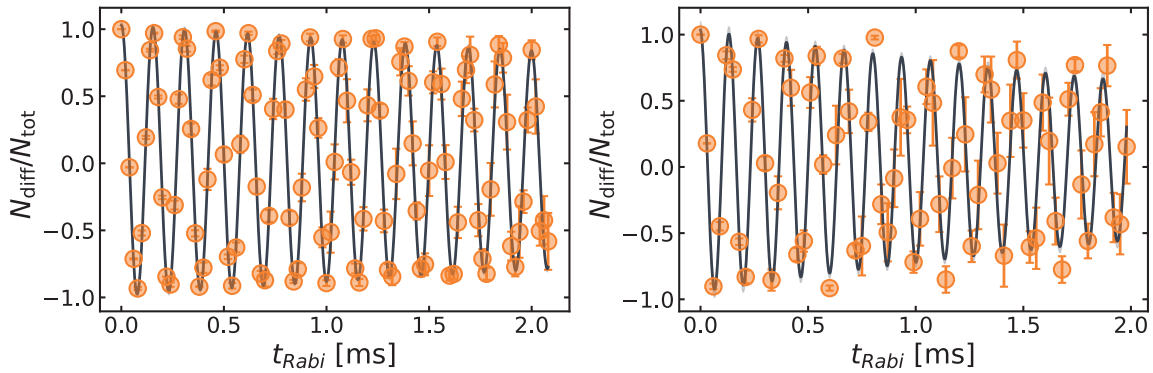


Figure 5.12. Rabi oscillations with different transitions. **Left:** oscillations between $|F = 1, m_F = 1\rangle$ and $|F = 2, m_F = 0\rangle$ with a dephasing time of $10.2(34)$ ms. **Right:** oscillations between $|F = 1, m_F = 1\rangle$ and $|F = 2, m_F = 2\rangle$ with a dephasing time of $3.36(62)$ ms.

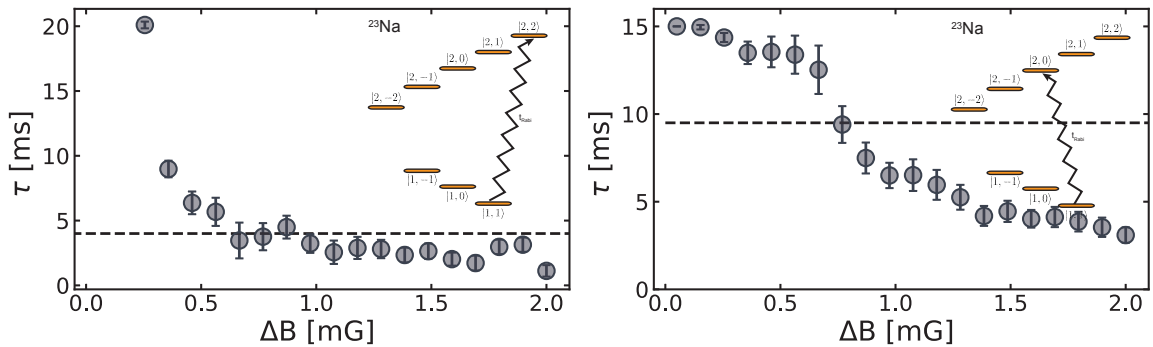


Figure 5.13. Dephasing time as a function of the magnetic field fluctuations for two different transitions. **Left:** The transition $|1, 1\rangle$ to $|2, 2\rangle$ is used. **Right:** The transition $|1, 1\rangle$ to $|2, 0\rangle$ is used whilst taking into account the lifetime of $|2, 0\rangle$. The dashed lines indicate the dephasing time obtained from the experiment using each transition respectively. The dashed lines indicates the dephasing time extracted from the experimental platform.

5.3 Local confinement

5.3.1 Optical lattice

The local confinement is achieved in the platform using a one-dimensional lattice as described in [84, 104]. The lattice is created by focusing two parallel beams using a lens with focal length of 200 mm, as can be seen in Fig.4.20. The distance between the two lattice beams before the lens is given by 10 mm, therefore the lattice spacing a_L for a given wavelength λ can be calculated using the following equation,

$$a_L = \frac{\lambda f}{d} \quad f \gg d \quad (5.9)$$

where λ is the wavelength of the lattice beams, f is the focal length of the lens and d is the distance between the two parallel lattice beams. The simplest way of changing the lattice spacing is to change the wavelength of the lattice beams. For this reason, the lattice laser is changed from a coherent Verdi V10 (532 nm) to a tunable Ti:sapphire laser system (520 nm to 1030 nm) from Sirah Lasertechnik. The wavelength of the lattice is set to be 610 nm which makes it red-detuned for sodium atoms and the lattice spacing is given by 11.6(6) μm in this case. Given 5 mW in each lattice beam, the trapping frequency is around 2 kHz, therefore the tunnelling effect between different lattice wells can be ignored in this regime [94, 108] and each lattice well can be assumed to be an independent system.

5.3.2 Spatial inhomogeneity of one-photon coupling

Rabi cycles inside the optical lattice are used to understand the system locally. After sodium atoms are condensed in the cross dipole trap, the lattice is ramped up adiabatically in 200 ms to confine the atoms locally. The coupling between $|1, 1\rangle$ and $|2, 2\rangle$ is carried out using the MW field at 2 G, as in the dipole trap without any local confinement. For detection, atoms are first separated using a magnetic field gradient (Stern Gerlach) while keeping both the dipole beams on. The Stern Gerlach pulse used is optimised such that the separation is along the direction of the lattice. Absorption imaging is used to image the atoms inside the lattice. By varying the duration of the MW field, the Rabi oscillations can be observed as shown in Fig. 5.15.

Rabi frequencies can be extracted locally by measuring the population imbalance in each lattice well as shown in Fig.5.16. Assuming the magnetic field gradient across the cloud is negligible, and given the Rabi frequency is proportional to

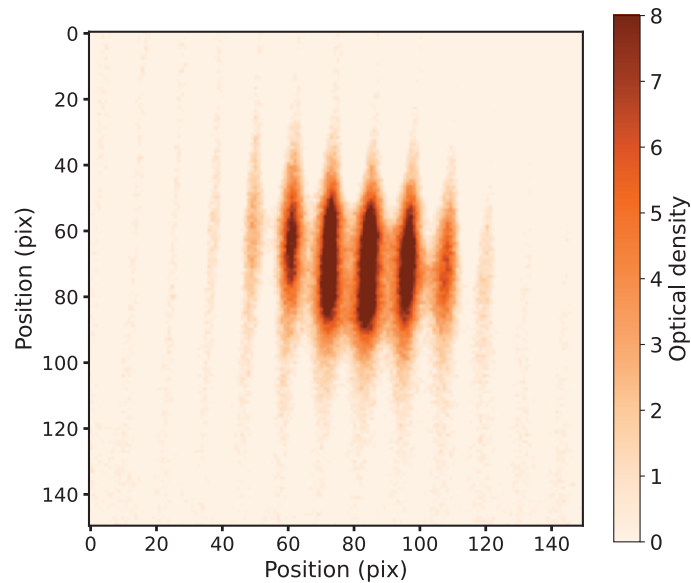


Figure 5.14. An in-situ image of sodium atoms inside a 610 nm optical lattice. Each lattice beam has a power of 5 mW. Atoms are trapped at intensity maximums.

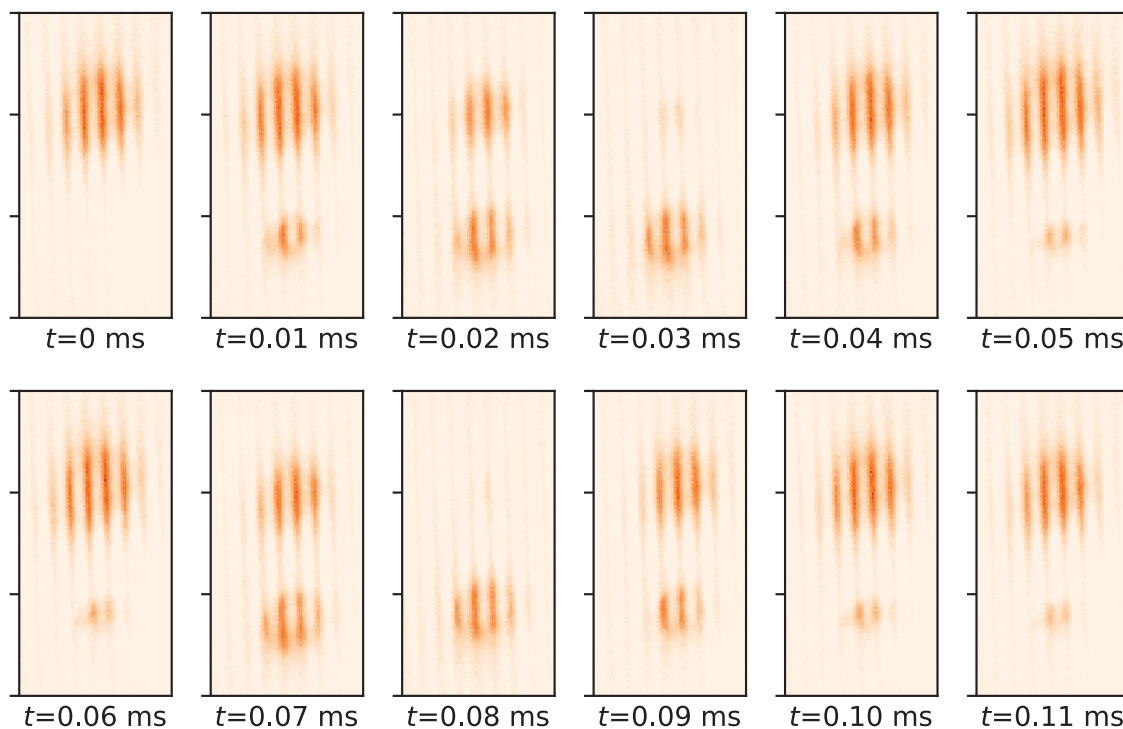


Figure 5.15. Rabi oscillations between $|F = 1, m_F = 1\rangle$ and $|F = 2, m_F = 2\rangle$ inside an optical lattice. The two states are separated using a Stern Gerlach pulse before imaging.

square root of the MW power, the incident field gradient across the atomic cloud can be deduced from the Rabi frequencies as shown in Fig.5.16. Due to the limited amount of data available caused by the vacuum issue, more measurements are needed for the MW field gradient analysis.

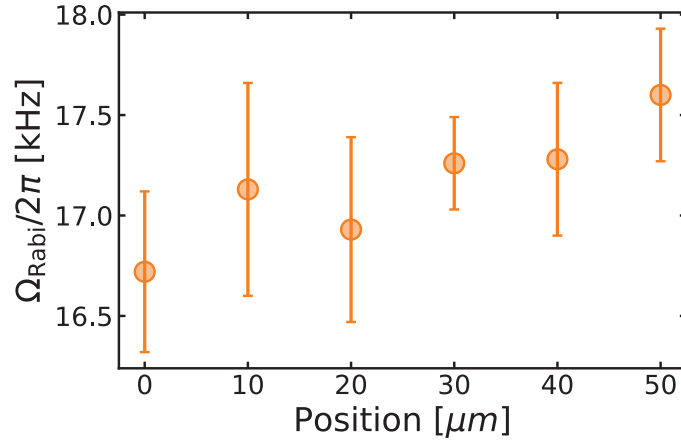


Figure 5.16. The local Rabi frequencies obtained from each well of the lattice. The Rabi frequency ranges from 16.80(82) kHz to 17.60(75) kHz. The large standard errors can be attributed mainly to the limited amount of data points available for the measurement.

5.3.3 Detection noise of the imaging system

By taking advantage of the local confinement achieved by the lattice, the detection limit of the current imaging system can be calibrated. The calibration method makes use of a coherent spin state which follows a binomial probability distribution [109]. By carrying out statistical analysis of N independent particles in a superposition state of $|\psi\rangle = \sqrt{1-p}|1\rangle + \sqrt{p}|2\rangle$, the probability of finding N_2 particles in state $|2\rangle$ is given as follows

$$P(N_2; N, p) = \frac{N!}{N_2!(N - N_2)!} p^{N_2} (1 - p)^{N - N_2} \quad (5.10)$$

Similarly the variance and covariance are given by the following,

$$\text{Var}(N_2; N, p) = \text{Var}(N_1; N, 1 - p) = Np(1 - p) \quad (5.11)$$

$$\text{Cov}(N_1, N_2; p) = -Np(1 - p) \quad (5.12)$$

Combining Eq.5.11 and 5.12, the variance of the difference of the atom number in the two states $|1\rangle$ and $|2\rangle$ for a coherent spin state can be expressed as

$$\text{Var}(\Delta N)_{\text{CSS}} = \text{Var}(N_1) + \text{Var}(N_2) - 2\text{Cov}(N_1, N_2) = 4Np(1 - p) \quad (5.13)$$

where $\Delta N = N_1 - N_2$ is the population difference between the two states. The fluctuation is maximised ($\text{Var}(\Delta N)_{CSS} = N$) for an equal superposition ($p = 0.5$) and minimised ($\text{Var}(\Delta N)_{CSS} = 0$) for fully polarised states ($p = 0, 1$). Given the population imbalance is defined as $z = \Delta N/N$, the fluctuations of z known as the quantum projection noise, or shot noise, can be expressed as

$$\text{Var}(z)_{CSS} = \frac{4p(1-p)}{N} = \frac{1 - \langle z \rangle^2}{N} \quad (5.14)$$

Experimentally, quantum projection noise of a coherent spin state can be used to calibrate the imaging system [110]. An equal superposition of sodium atoms in $|1, 1\rangle$ and $|2, 2\rangle$ can be prepared using the MW field. The sum $N = N_1 + N_2$ and difference $\Delta N = N_1 - N_2$ of atom number for the two states can then be calculated. For such a coherent spin state, the variance of the difference in atom number is given by $\text{Var}(\Delta N)_{CSS} = N + \text{Var}[Det(I)]$. The term $\text{Var}[Det(I)]$ corresponds to the detection noise, which depends on intensity of the imaging light. The measurement was carried out for sodium atoms inside the lattice and the results are given in Fig.5.17. As the imaging calibration was performed on the platform as described in [47], a function $y = N + \delta_{tech}^2 N^2 + \Delta_{Det}$ is fitted by taking the technical noise $\Delta_{tech}^2 = \delta_{tech}^2 N^2$ into account. The technical noise can arise from fluctuations in either the Rabi coupling strength or magnetic field. A detection noise of $\Delta_{Det} = 331(37)$ is extracted from the experimental data.

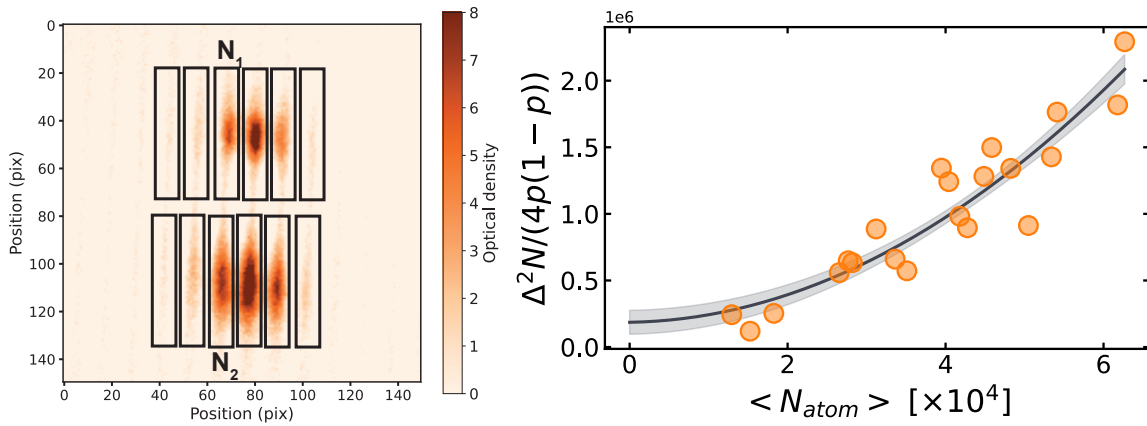


Figure 5.17. Shot-noise measurements using an optical lattice. **Left:** A realisation of a coherent spin state prepared in the lattice. The atom number in 6 lattice wells are measured separately. **Right:** The detection noise extracted from the fit is $\Delta_{det} = 331(37)$ atoms.

Given the quadratic dependence presented in the experimental data, technical noise is a dominating factor for the measurements. Fluctuations in the MW power

can be reduced by actively stabilising the MW power as described in [111]. The imaging path on the experimental table could be optimised by using an AOM double path as well as actively stabilising the imaging beam intensity. After reducing the technical noises, the imaging calibration should be carried out again by varying the intensity of the imaging beam and looking for the linear dependence between the variance in ΔN and atom number N with the gradient equal to 1.

5.4 Fluorescence imaging

Due to the issues related to the vacuum system during the last stage of this thesis, as well as working towards non-destructive detection on the platform, effort has been put in to achieve single atom counting in a sodium MOT with fluorescence imaging. Fluorescence imaging at the level of a single atom has been demonstrated on similar platforms [112, 113].

5.4.1 A toy model for atom number dynamics

To understand the loading process, a simple toy model is developed. At each time step, there are three processes involved in the model which are loading an atom, losing one atom due to collisions with the background gas and losing two atoms due to light-assisted collisions. The probability of losing one atom is given by p_1 and the probability of losing one atom in a MOT with N atoms due to collisions with background gas is given by the following,

$$P(1; N, p_1) = \frac{N!}{1!(N-1)!} p_1 (1 - p_1)^{N-1} \quad (5.15)$$

Similarly, the probability of losing two atoms from the trap due to light-assisted collisions can be described using Eqn. 5.16, where N_{pair} is the number of pairs of atoms inside the trap.

$$P(1; N_{pair}, p_2) = \frac{N!}{1!(N_{pair}-1)!} p_2 (1 - p_2)^{N_{pair}-1} \quad (5.16)$$

Integrating the three processes into the toy model in the continuum limit gives a basic understanding of the dynamics of the sodium MOT loading process on the platform.

An example of time traces generated using the toy model is shown in Fig. 5.18. Light-assisted collision has been studied extensively both theoretically and experimentally [114–116], which could lead to sub-Poissonian loading of atoms in traps [117]. A similar behaviour can also be observed using the toy model by looking at the variance of each atom number as shown in Fig. 5.19

5.4.2 Experimental observations

The experimental sequence used for atom counting is similar to the one used in [113]. During each experimental run, 200 images are taken before switching on the magnetic field to load the atoms. During the loading process, another 200 images

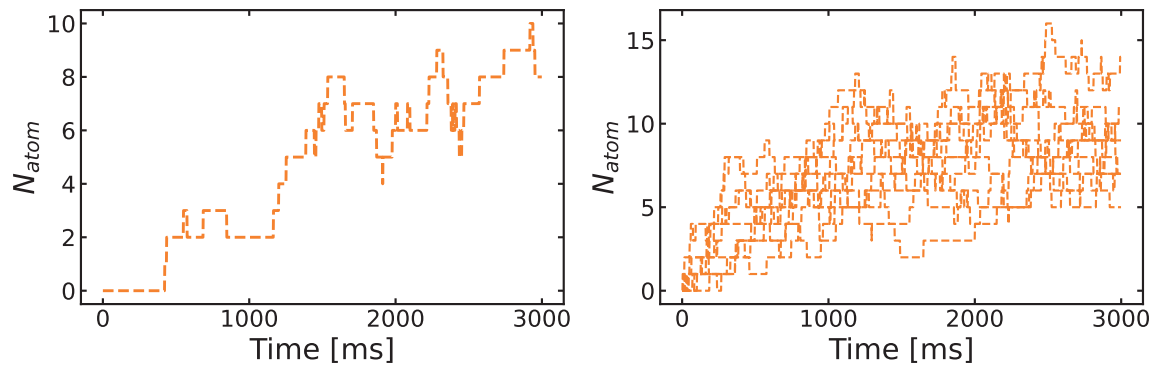


Figure 5.18. A single time trace (**left**) and 100 (**right**) time traces of loading dynamics up to $T = 3$ s generated using the toy model.

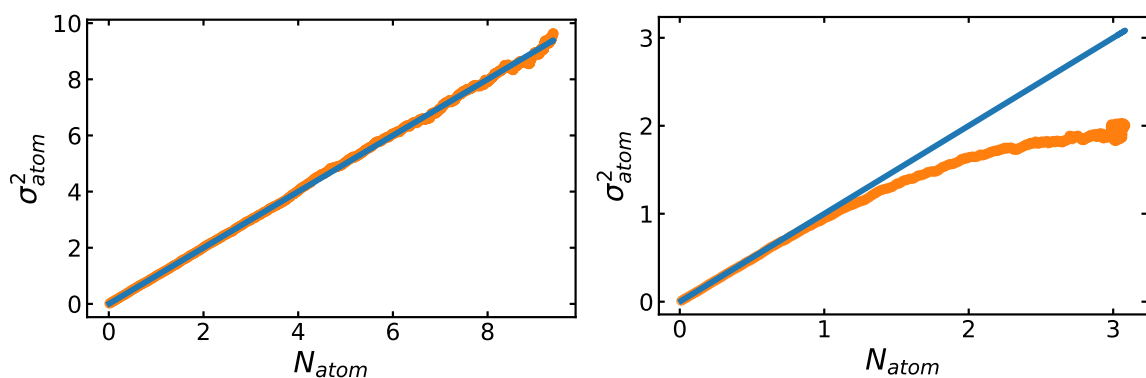


Figure 5.19. Sub-Poissonian loading due to light-assisted collisions observed using the toy model. The orange line indicates the mean and variance computed from the time traces and the blue line indicates the Poissonian limit. **Left:** Light-assisted collisions are switched off. **Right:** Light-assisted collisions are switched on.

are taken for the purpose of counting and finally another 100 images are taken after the magnetic field is switched off. The MOT beams are kept on during the whole sequence and the exposure time of each image can be varied by changing the trigger pulse length of the camera.

In order to observe a single sodium atom in the MOT, the experimental platform has been modified. Firstly, the imaging magnification has been reduced from 6 to 0.75 to reduce the size of the MOT on the camera, which reduces the number of pixels needed to image the MOT. Given the platform was optimised for fast loading, the diameter of the MOT and repumper beams were reduced from 2.54 cm to roughly 2 mm. The valve to the science cell was also closed to reduce the number of atoms entering the science cell as well as actively cooling the ion pump of the science cell. Despite all the efforts to reduce the loading rate of the MOT, the minimal loading

rate is still around 20 atom/s.

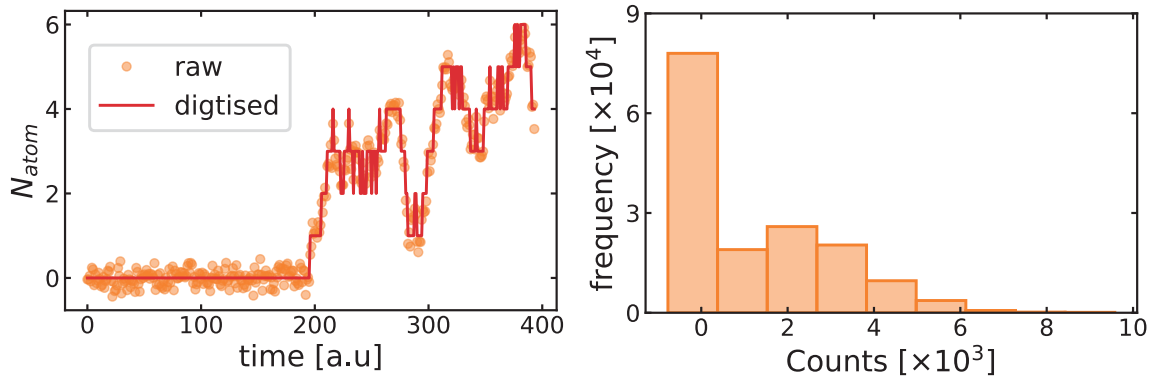


Figure 5.20. The single atom signal obtained on the platform. **Left:** A single time trace before (orange) and after (red) digitisation using the calculated calibration factor. **Right:** A histogram of the camera counts during the MOT loading for 100 time traces. Clear separation due to single atom dynamics cannot be observed from the histogram.

For data analysis, the number of counts in a selected region of interest seen on the camera is summed up for each image. The first and last 100 images serve as the reference images which are subtracted from the 200 images with loading. Typically, the camera has a dead time of 12 ms for the external acquisition mode used, and an exposure time of 20 ms is used for each image. To extract the atom number from the counts measured on the camera, clear jumps should be observed in the time traces as well as in the histogram of the camera counts. However, clear jumps are not able to be observed in the histogram due to the fast loading rate and short lifetime of the atoms inside the trap as shown in Fig. 5.20. As a result, an estimation of imaging efficiency is carried out by taking into account factors such as the numerical aperture of the imaging system, the quantum efficiency of the camera and the transmission of the optical elements in the imaging path which yields a value of 0.9%. The scattering rate of an atom is given by the following [118],

$$R_{sc} = \frac{\Gamma}{2} \frac{I/I_{sat}}{1 + 4(\Delta/\Gamma)^2 + (I/I_{sat})} \quad (5.17)$$

where $\Gamma = 2\pi \times 9.795(13)$ MHz is the natural line width of the D_2 transition, $I_{sat} = 6.26$ mW/cm² is the saturation intensity, and Δ and I are the detuning and intensity of the MOT beams. For $I = 13.8$ mW/cm² and $\Delta = 1.3\Gamma$, the scattering rate is given by 6.8×10^6 s⁻¹. For 20 ms exposure time, around 1300 photons are expected to be collected by the camera for an atom. Using the calibration number obtained from the estimation, the raw data is digitised to extract the atom number as shown in Fig.5.20.

To summarise, single atom dynamics could be observed on the platform from the time traces after digitisation of the raw data. However, factors such as fast loading and the short lifetime of the atoms inside the trap smear out individual jumps in the histogram. Further work needs to be carried out to reduce the loading rate and improve the lifetime of the MOT.

6 Outlook

Ultracold mixture platforms have shown great potential for both quantum simulation and computation, but the stability and reliability of such platforms still remain a challenge. In the platform described in this thesis, progress has been made in various aspects of the experiment. Stable production of sodium BECs with around 460×10^3 atoms has been achieved. More precise control of the internal spin states via Rabi oscillations could be achieved with a more precise magnetic field stabilisation scheme down to $750 \mu\text{G}$. The local confinement of the system has been achieved by using a 1D optical lattice where Rabi oscillations were made possible. For state detection, the imaging system is characterised using the quantum projection noise of a coherent spin state inside the lattice. The detection limit is given by $\Delta_{det} = 331(37)$ atoms. Additionally, to prepare for non-destructive detection inside the lattice, progress has been made towards single atom resolution in a sodium MOT with fluorescence imaging.

To further improve both the stability and control of the platform, further work can be carried out. The stability of BEC production can be improved by simplifying the current laser table setup, such as replacing the 1.7 GHz frequency AOM with a 350 MHz AOM in a quadruple path configuration. The diffraction efficiency could be improved from 5 % up to 40 % in a similar sodium potassium mixture platform in the same lab. For spin manipulation, a stabilisation scheme needs to be implemented on the MW power setup, as a small change in MW power reduces the dephasing time significantly. More involved state manipulation sequences such as Ramsey spectroscopy and spin echoes can also be carried out on the platform. Long term stability of spin control can be achieved by activate temperature stabilisation of the microwave and magnetic field control setup. To improve the detection, the imaging system needs to be re-calibrated using the lattice implemented in the platform. Moreover, work towards a non-destructive detection of atoms inside the optical lattice can also be carried out based on the knowledge obtained implementing the sodium MOT.

Bibliography

- [1] M. H. Anderson, J. R. Ensher, M. R. Matthews, C. E. Wieman, and E. A. Cornell. Observation of bose-einstein condensation in a dilute atomic vapor. *Science*, 269(5221):198–201, 1995.
- [2] C. C. Bradley, C. A. Sackett, J. J. Tollett, and R. G. Hulet. Evidence of bose-einstein condensation in an atomic gas with attractive interactions. *Phys. Rev. Lett.*, 75:1687–1690, Aug 1995.
- [3] K. B. Davis, M. O. Mewes, M. R. Andrews, N. J. van Druten, D. S. Durfee, D. M. Kurn, and W. Ketterle. Bose-einstein condensation in a gas of sodium atoms. *Phys. Rev. Lett.*, 75:3969–3973, Nov 1995.
- [4] E. A. Cornell and C. E. Wieman. Nobel lecture: Bose-einstein condensation in a dilute gas, the first 70 years and some recent experiments. *Rev. Mod. Phys.*, 74:875–893, Aug 2002.
- [5] Wolfgang Ketterle. Nobel lecture: When atoms behave as waves: Bose-einstein condensation and the atom laser. *Rev. Mod. Phys.*, 74:1131–1151, Nov 2002.
- [6] Immanuel Bloch, Jean Dalibard, and Wilhelm Zwerger. Many-body physics with ultracold gases. *Rev. Mod. Phys.*, 80:885–964, Jul 2008.
- [7] D Jaksch. Optical lattices, ultracold atoms and quantum information processing. *Contemporary Physics*, 45(5):367–381, 2004.
- [8] Immanuel Bloch. Quantum coherence and entanglement with ultracold atoms in optical lattices. *Nature*, 453:1016–22, 07 2008.
- [9] Igor B Mekhov and Helmut Ritsch. Quantum optics with ultracold quantum gases: towards the full quantum regime of the light–matter interaction. *Journal of Physics B: Atomic, Molecular and Optical Physics*, 45(10):102001, may 2012.

- [10] Immanuel Bloch. Ultracold quantum gases in optical lattices. *Nat. Phys.*, 1:23–30, 10 2005.
- [11] Maciej Lewenstein, Anna Sanpera, Veronica Ahufinger, Bogdan Damski, Aditi Sen de, and Ujjwal Sen. Ultracold atomic gases in optical lattices: Mimicking condensed matter physics and beyond. *Advances in Physics*, 56, 07 2006.
- [12] Peter K. Molony, Philip D. Gregory, Zhonghua Ji, Bo Lu, Michael P. Köppinger, C. Ruth Le Sueur, Caroline L. Blackley, Jeremy M. Hutson, and Simon L. Cornish. Creation of ultracold $^{87}\text{Rb}^{133}\text{Cs}$ molecules in the rovibrational ground state. *Phys. Rev. Lett.*, 113:255301, Dec 2014.
- [13] Mingwu Lu, Nathaniel Q. Burdick, Seo Ho Youn, and Benjamin L. Lev. Strongly dipolar bose-einstein condensate of dysprosium. *Phys. Rev. Lett.*, 107:190401, Oct 2011.
- [14] J. Stenger, S. Inouye, D. M. Stamper-Kurn, H. J. Miesner, A. P. Chikkatur, and W. Ketterle. Spin domains in ground-state Bose-Einstein condensates. *Nature*, 396(6709):345–348, November 1998.
- [15] A. M. Kaufman, B. J. Lester, and C. A. Regal. Cooling a single atom in an optical tweezer to its quantum ground state. *Phys. Rev. X*, 2:041014, Nov 2012.
- [16] Markus Greiner, Immanuel Bloch, Olaf Mandel, Theodor W. Hänsch, and Tilman Esslinger. Bose–einstein condensates in 1d- and 2d optical lattices. *Applied Physics B*, 73:769–772, 2001.
- [17] Markus Greiner, Immanuel Bloch, Olaf Mandel, Theodor W. Hänsch, and Tilman Esslinger. Exploring phase coherence in a 2d lattice of bose-einstein condensates. *Phys. Rev. Lett.*, 87:160405, Oct 2001.
- [18] C Becker, P Soltan-Panahi, J Kronjäger, S Dörscher, K Bongs, and K Sengstock. Ultracold quantum gases in triangular optical lattices. *New Journal of Physics*, 12(6):065025, jun 2010.
- [19] Gyu-Boong Jo, Jennie Guzman, Claire K. Thomas, Pavan Hosur, Ashvin Vishwanath, and Dan M. Stamper-Kurn. Ultracold atoms in a tunable optical kagome lattice. *Phys. Rev. Lett.*, 108:045305, Jan 2012.
- [20] Bel'en Paredes, Artur Widera, Valentin Murg, Olaf Mandel, Simon Fölling, Ignacio I. Cirac, Gora V. Shlyapnikov, Theodor W. Hänsch, and Immanuel

- Bloch. Tonks–girardeau gas of ultracold atoms in an optical lattice. *Nature*, 429:277–281, 2004.
- [21] Thilo Stöferle, Henning Moritz, Christian Schori, Michael Köhl, and Tilman Esslinger. Transition from a strongly interacting 1d superfluid to a mott insulator. *Phys. Rev. Lett.*, 92:130403, Mar 2004.
- [22] S. Nascimbène, Y.-A. Chen, M. Atala, M. Aidelsburger, S. Trotzky, B. Paredes, and I. Bloch. Experimental realization of plaquette resonating valence-bond states with ultracold atoms in optical superlattices. *Phys. Rev. Lett.*, 108:205301, May 2012.
- [23] Olaf Mandel, Markus Greiner, Artur Widera, Tim Rom, Theodor W. Hänsch, and Immanuel Bloch. Coherent transport of neutral atoms in spin-dependent optical lattice potentials. *Phys. Rev. Lett.*, 91:010407, Jul 2003.
- [24] Simon Fölling. *Probing strongly correlated states of ultracold atoms in optical lattices*. PhD thesis, Mainz, 2008.
- [25] R. Meppelink, R. A. Rozendaal, S. B. Koller, J. M. Vogels, and P. van der Straten. Thermodynamics of bose-einstein-condensed clouds using phase-contrast imaging. *Phys. Rev. A*, 81:053632, May 2010.
- [26] Karl Nelson, Xiao Li, and David Weiss. Imaging single atoms in a three-dimensional array. *Nature Physics*, 3, 06 2007.
- [27] Y. Miroshnychenko, D. Schrader, S. Kuhr, W. Alt, I. Dotsenko, M. Khudaverdyan, A. Rauschenbeutel, and D. Meschede. Continued imaging of the transport of a single neutral atom. *Opt. Express*, 11(25):3498–3502, Dec 2003.
- [28] Tsung-Yao Wu, Aishwarya Kumar, Felipe Giraldo, and David S. Weiss. Stern–gerlach detection of neutral-atom qubits in a state-dependent optical lattice. *Nature Physics*, 15:538–542, 2019.
- [29] Philipp M. Preiss, Ruichao Ma, M. Eric Tai, Jonathan Simon, and Markus Greiner. Quantum gas microscopy with spin, atom-number, and multilayer readout. *Phys. Rev. A*, 91:041602, Apr 2015.
- [30] Martin Boll, Timon A. Hilker, Guillaume Salomon, Ahmed Omran, Jacopo Nespolo, Lode Pollet, Immanuel Bloch, and Christian Gross. Spin- and density-resolved microscopy of antiferromagnetic correlations in fermi-hubbard chains. *Science*, 353(6305):1257–1260, 2016.

- [31] C. J. Myatt, E. A. Burt, R. W. Ghrist, E. A. Cornell, and C. E. Wieman. Production of two overlapping bose-einstein condensates by sympathetic cooling. *Phys. Rev. Lett.*, 78:586–589, Jan 1997.
- [32] Andrew G. Truscott, Kevin E. Strecker, William I. McAlexander, Guthrie B. Partridge, and Randall G. Hulet. Observation of Fermi Pressure in a Gas of Trapped Atoms. *Science*, 291(5513):2570–2572, March 2001.
- [33] Z. Hadzibabic, C. A. Stan, K. Dieckmann, S. Gupta, M. W. Zwierlein, A. Görlitz, and W. Ketterle. Two-species mixture of quantum degenerate bose and fermi gases, Apr 2002.
- [34] G. Roati, F. Riboli, G. Modugno, and M. Inguscio. Fermi-bose quantum degenerate ^{40}K – ^{87}Rb mixture with attractive interaction. *Phys. Rev. Lett.*, 89:150403, Sep 2002.
- [35] G. Modugno, M. Modugno, F. Riboli, G. Roati, and M. Inguscio. Two atomic species superfluid. *Phys. Rev. Lett.*, 89:190404, Oct 2002.
- [36] C. Silber, S. Günther, C. Marzok, B. Deh, Ph. W. Courteille, and C. Zimmermann. Quantum-degenerate mixture of fermionic lithium and bosonic rubidium gases. *Phys. Rev. Lett.*, 95:170408, Oct 2005.
- [37] M. Zaccanti, C. D’Errico, F. Ferlaino, G. Roati, M. Inguscio, and G. Modugno. Control of the interaction in a fermi-bose mixture. *Phys. Rev. A*, 74:041605, Oct 2006.
- [38] S. Ospelkaus, C. Ospelkaus, L. Humbert, K. Sengstock, and K. Bongs. Tuning of heteronuclear interactions in a degenerate fermi-bose mixture. *Phys. Rev. Lett.*, 97:120403, Sep 2006.
- [39] S. B. Papp, J. M. Pino, and C. E. Wieman. Tunable miscibility in a dual-species bose-einstein condensate. *Phys. Rev. Lett.*, 101:040402, Jul 2008.
- [40] M. Taglieber, A.-C. Voigt, T. Aoki, T. W. Hänsch, and K. Dieckmann. Quantum degenerate two-species fermi-fermi mixture coexisting with a bose-einstein condensate. *Phys. Rev. Lett.*, 100:010401, Jan 2008.
- [41] Alexander Mil, Torsten Zache, Apoorva Hegde, Andy Xia, Rohit Bhatt, Markus Oberthaler, Philipp Hauke, Jürgen Berges, and Fred Jendrzejewski. A scalable realization of local $u(1)$ gauge invariance in cold atomic mixtures. *Science*, 367:1128–1130, 03 2020.

- [42] Wolfgang Niedenzu, Igor Mazets, Gershon Kurizki, and Fred Jendrzejewski. Quantized refrigerator for an atomic cloud. *Quantum*, 3:155, June 2019.
- [43] Valentin Kasper, Daniel González-Cuadra, Apoorva Hegde, Andy Xia, Alexandre Dauphin, Felix Huber, Eberhard Tiemann, Maciej Lewenstein, Fred Jendrzejewski, and Philipp Hauke. Universal quantum computation and quantum error correction with ultracold atomic mixtures. *Quantum Science and Technology*, 7(1):015008, nov 2021.
- [44] Luigi De Marco, Giacomo Valtolina, Kyle Matsuda, William G. Tobias, Jacob P. Covey, and Jun Ye. A degenerate fermi gas of polar molecules. *Science*, 363:853 – 856, 2019.
- [45] Dan M. Stamper-Kurn and Masahito Ueda. Spinor bose gases: Symmetries, magnetism, and quantum dynamics. *Rev. Mod. Phys.*, 85:1191–1244, Jul 2013.
- [46] Tin-Lun Ho. Spinor bose condensates in optical traps. *Phys. Rev. Lett.*, 81:742–745, Jul 1998.
- [47] Alexander Mil. *Experimental realization of $U(1)$ gauge invariance in ultracold atomic mixtures*. PhD thesis, Universität Heidelberg, 2020.
- [48] S. Inouye, M. R. Andrews, J. Stenger, H. J. Miesner, D. M. Stamper-Kurn, and W. Ketterle. Observation of Feshbach resonances in a Bose-Einstein condensate. *Nature*, 392(6672):151–154, March 1998.
- [49] Paul Langacker. *The standard model and beyond*. 2010.
- [50] F. Halzen and Alan D. Martin. *QUARKS AND LEPTONS: AN INTRODUCTORY COURSE IN MODERN PARTICLE PHYSICS*. 1984.
- [51] Patrick A. Lee, Naoto Nagaosa, and Xiao-Gang Wen. Doping a mott insulator: Physics of high-temperature superconductivity. *Rev. Mod. Phys.*, 78:17–85, Jan 2006.
- [52] Julian Schwinger. On gauge invariance and vacuum polarization. *Phys. Rev.*, 82:664–679, Jun 1951.
- [53] Owe Philipsen and Hartmut Wittig. String breaking in non-abelian gauge theories with fundamental matter fields. *Phys. Rev. Lett.*, 81:4056–4059, Nov 1998.

- [54] Gunnar S. Bali, Hartmut Neff, Thomas Düssel, Thomas Lippert, and Klaus Schilling. Observation of string breaking in qcd. *Phys. Rev. D*, 71:114513, Jun 2005.
- [55] F. Hebenstreit, J. Berges, and D. Gelfand. Real-time dynamics of string breaking. *Phys. Rev. Lett.*, 111:201601, Nov 2013.
- [56] Logan W. Clark, Brandon M. Anderson, Lei Feng, Anita Gaj, K. Levin, and Cheng Chin. Observation of density-dependent gauge fields in a bose-einstein condensate based on micromotion control in a shaken two-dimensional lattice. *Phys. Rev. Lett.*, 121:030402, Jul 2018.
- [57] Frederik Görg, Kilian Sandholzer, Joaquín Minguzzi, Rémi Desbuquois, Michael Messer, and Tilman Esslinger. Realization of density-dependent peierls phases to engineer quantized gauge fields coupled to ultracold matter. *Nature Physics*, 15:1–7, 11 2019.
- [58] Christian Schweizer, Fabian Grusdt, Moritz Berngruber, Luca Barbiero, Eugene Demler, Nathan Goldman, Immanuel Bloch, and Monika Aidelsburger. Floquet approach to \square_2 lattice gauge theories with ultracold atoms in optical lattices. *Nature Physics*, 15(11):1168–1173, 2019.
- [59] Xiaoke Li, Bing Zhu, Xiaodong He, Fudong Wang, Mingyang Guo, Zhi-Fang Xu, Shizhong Zhang, and Dajun Wang. Coherent heteronuclear spin dynamics in an ultracold spinor mixture. *Phys. Rev. Lett.*, 114:255301, Jun 2015.
- [60] Helmut Strobel, W. Muessel, Daniel Linnemann, Tilman Zibold, David B. Hume, Luca Pezzè, Augusto Smerzi, and Markus K. Oberthaler. Fisher information and entanglement of non-gaussian spin states. *Science*, 345:424 – 427, 2014.
- [61] Eike Nicklas. *A new tool for miscibility control: Linear coupling*. PhD thesis, Universität Heidelberg, 2013.
- [62] E. Timmermans. Phase separation of bose-einstein condensates. *Phys. Rev. Lett.*, 81:5718–5721, Dec 1998.
- [63] Pitaevskii L. P. and S. Stringari. *Bose-Einstein condensation and superfluidity*. Oxford University Press, 2018.
- [64] David DiVincenzo and IBM. The physical implementation of quantum computation. *Fortschritte der Physik*, 48, 03 2000.

- [65] A. Farolfi, A. Zenesini, R. Cominotti, D. Trypogeorgos, A. Recati, G. Lamporesi, and G. Ferrari. Manipulation of an elongated internal josephson junction of bosonic atoms. *Phys. Rev. A*, 104:023326, Aug 2021.
- [66] P. L. Knight, E. A. Hinds, M. B. Plenio, D. J. Wineland, M. Barrett, J. Britton, J. Chiaverini, B. DeMarco, W. M. Itano, B. Jelenković, C. Langer, D. Leibfried, V. Meyer, T. Rosenband, and T. Schätz. Quantum information processing with trapped ions. *Philosophical Transactions of the Royal Society of London. Series A: Mathematical, Physical and Engineering Sciences*, 361(1808):1349–1361, 2003.
- [67] T. Rentrop, A. Trautmann, F. A. Olivares, F. Jendrzejewski, A. Komnik, and M. K. Oberthaler. Observation of the phononic lamb shift with a synthetic vacuum. *Phys. Rev. X*, 6:041041, Nov 2016.
- [68] Fabian Grusdt and Eugene Demler. New theoretical approaches to bose polarons, 2015.
- [69] Helmut Strobel, Wolfgang Muessel, Daniel Linnemann, Tilman Zibold, David B. Hume, Luca Pezzè, Augusto Smerzi, and Markus K. Oberthaler. Fisher information and entanglement of non-gaussian spin states. *Science*, 345(6195), 2014.
- [70] C. Gross, H. Strobel, E. Nicklas, T. Zibold, N. Bar-Gill, G. Kurizki, and M. K. Oberthaler. Atomic homodyne detection of continuous-variable entangled twin-atom states. *Nature*, 480(7376), 2011.
- [71] H. J. Metcalf and P. van der Straten. Laser cooling and trapping of atoms. *J. Opt. Soc. Am. B*, 20(5):887–908, May 2003.
- [72] C. J. Pethick and H. Smith. *Bose–Einstein Condensation in Dilute Gases*. Cambridge University Press, 2001.
- [73] Samuel Francis Boys. Electronic wave functions - i. a general method of calculation for the stationary states of any molecular system. *Proceedings of the Royal Society of London. Series A. Mathematical and Physical Sciences*, 200:542 – 554, 1950.
- [74] N. N. Bogolyubov. On the theory of superfluidity. *J. Phys. (USSR)*, 11:23–32, 1947.

- [75] Franco Dalfovo, Stefano Giorgini, Lev P. Pitaevskii, and Sandro Stringari. Theory of bose-einstein condensation in trapped gases. *Rev. Mod. Phys.*, 71:463–512, Apr 1999.
- [76] M.-O. Mewes, M. R. Andrews, N. J. van Druten, D. M. Kurn, D. S. Durfee, and W. Ketterle. Bose-einstein condensation in a tightly confining dc magnetic trap. *Phys. Rev. Lett.*, 77:416–419, Jul 1996.
- [77] M. J. Holland, D. S. Jin, M. L. Chiofalo, and J. Cooper. Emergence of interaction effects in bose-einstein condensation. *Phys. Rev. Lett.*, 78:3801–3805, May 1997.
- [78] Tobias Kraemer, Jens Herbig, Michael Mark, Tino Weber, Cheng Chin, Hanns-Christoph Nägerl, and Rudolf Grimm. Optimized production of a cesium bose–einstein condensate. *Applied Physics B*, 79:1013–1019, 12 2004.
- [79] P. A. Ruprecht, M. J. Holland, K. Burnett, and Mark Edwards. Time-dependent solution of the nonlinear schrödinger equation for bose-condensed trapped neutral atoms. *Phys. Rev. A*, 51:4704–4711, Jun 1995.
- [80] Y. Castin and R. Dum. Bose-einstein condensates in time dependent traps. *Phys. Rev. Lett.*, 77:5315–5319, Dec 1996.
- [81] Jens Appmeier. Immersed quantum systems : A sodium bose-einstein condensate for polaron studies, 2010.
- [82] Marc Repp. Aufbau einer vakuumapparatur für experimente mit ultrakalten fermionischen und bosonischen quantengasen. Diploma thesis, Universität Heidelberg, 2007.
- [83] CA Stan and W. Ketterle. Multiple species atom source for laser-cooling experiments. *Rev. Sci. Instrum.*, 76:063113, 2005.
- [84] Fabián Olivares. *Towards Lattice Gauge Theories in Ultracold Mixtures of Sodium and Lithium*. PhD thesis, Universität Heidelberg, 2018.
- [85] Johannes Schindler. Characterization of an erbium atomic beam. Masterarbeit, University of Innsbruck, 2011.
- [86] Friedhelm Serwane. he setup of a magneto optical trap for the preparation of a mesoscopic degenerate. Masterarbeit, Universität Heidelberg, 2007.

- [87] H. C. W. Beijerinck and N. F. Verster. Velocity distribution and angular distribution of molecular beams from multichannel arrays. *Journal of Applied Physics*, 46(5):2083–2091, 1975.
- [88] Jens Appmeier. *Immersed Quantum Systems : A Sodium Bose-Einstein Condensate for Polaron Studies*. PhD thesis, Universität Heidelberg, 01 2010.
- [89] Tanja Behrle. Construction and characterization of a diode laser setup and spectroscopy cell for ^6Li and ^7Li . Bachelor thesis, Universität Heidelberg, 2014.
- [90] Wolfgang Ketterle, Kendall B. Davis, Michael A. Joffe, Alex Martin, and David E. Pritchard. High densities of cold atoms in a dark spontaneous-force optical trap. *Phys. Rev. Lett.*, 70:2253–2256, Apr 1993.
- [91] Apoorva Anant Hegde. *Noisy Dynamics of $U(1)$ Lattice Gauge Theory in Ultracold Atomic Mixtures*. PhD thesis, Universität Heidelberg, 2022.
- [92] K. M. R. van der Stam, A. Kuijk, R. Meppelink, J. M. Vogels, and P. van der Straten. Spin-polarizing cold sodium atoms in a strong magnetic field. *Phys. Rev. A*, 73:063412, Jun 2006.
- [93] Anton Piccardo-Selg. Degenerate quantum gases: Towards bose-einstein condensation of sodium. Diploma thesis, Universität Heidelberg, 2008.
- [94] Rudolf Grimm, Matthias Weidemüller, and Yuri Ovchinnikov. Optical dipole traps for neutral atoms. *Advances in Atomic, Molecular, and Optical Physics*, 42:95, 12 2000.
- [95] Arno Trautmann. *Spin Dynamics and Feshbach Resonances in Ultracold Sodium-Lithium Mixtures*. PhD thesis, Universität Heidelberg, 2016.
- [96] G. Reinaudi, T. Lahaye, Z. Wang, and D. Guéry-Odelin. Strong saturation absorption imaging of dense clouds of ultracold atoms. *Opt. Lett.*, 32(21):3143–3145, Nov 2007.
- [97] Alexander Mil. Design and implementation of a versatile imaging objective for imaging of ultracold mixtures of sodium and lithium. Masterarbeit, Universität Heidelberg, 2016.
- [98] Jan Krieger. Zeeman-slower und experimentsteuerung für das nali-experiment. Masterarbeit, Universität Heidelberg, 2008.

- [99] P. T. Starkey, C. J. Billington, S. P. Johnstone, M. Jasperse, K. Helmerson, L. D. Turner, and R. P. Anderson. A scripted control system for autonomous hardware-timed experiments. *Review of Scientific Instruments*, 84(8):085111, 2013.
- [100] C. J. Billington. *State-dependent forces in cold quantum gases*. PhD thesis, Monash University, 2018.
- [101] P. T. Starkey. *A software framework for control and automation of precisely timed experiments*. PhD thesis, Monash University, 2019.
- [102] Wolfgang Ketterle and N.J. Van Druten. Evaporative cooling of trapped atoms. volume 37 of *Advances In Atomic, Molecular, and Optical Physics*, pages 181–236. Academic Press, 1996.
- [103] Harold Metcalf and Peter van der Straten. Cooling and trapping of neutral atoms. *Physics Reports*, 244(4):203–286, 1994.
- [104] Kai-Niklas Schymik. Implementing an optical accordion lattice for the realization of a quantized otto cycle. Masterarbeit, Universität Heidelberg, 2018.
- [105] Alexander Hesse. A nv center based magnetic field stabilization for atomic physics experiments. Masterarbeit, Universität Heidelberg, 2020.
- [106] Helmut Strobel. *Fisher Information and entanglement of non-Gaussian spin states*. PhD thesis, Universität Heidelberg, 2016.
- [107] Marcell Gall. Active magnetic field stabilisation for ultracold sodium lithium mixtures. Masterarbeit, Universität Heidelberg, 2015.
- [108] Wilhelm Zwerger. Mott hubbard transition of cold atoms in optical lattices. *Journal of Optics B: Quantum and Semiclassical Optics*, 5(2):S9–S16, apr 2003.
- [109] W. M. Itano, J. C. Bergquist, J. J. Bollinger, J. M. Gilligan, D. J. Heinzen, F. L. Moore, M. G. Raizen, and D. J. Wineland. Quantum projection noise: Population fluctuations in two-level systems. *Phys. Rev. A*, 47:3554–3570, May 1993.
- [110] Wolfgang Muessel, Helmut Strobel, Maxime Joos, Eike Nicklas, Ion Stroescu, Jiří Tomkovič, David B. Hume, and Markus K. Oberthaler. Optimized absorption imaging of mesoscopic atomic clouds. *Applied Physics B: Lasers and Optics*, 113(1):69–73, October 2013.

- [111] Jan Dreher. A microwave power stabilization setup for controlling spin dynamics in a bose-einstein condensate. Masterarbeit, Universität Heidelberg, 2022.
- [112] D. B. Hume, I. Stroescu, M. Joos, W. Muessel, H. Strobel, and M. K. Oberthaler. Accurate atom counting in mesoscopic ensembles. *Phys. Rev. Lett.*, 111:253001, Dec 2013.
- [113] Rohit Bhatt, Jan Kilinc, Lilo Höcker, and Fred Jendrzejewski. Stochastic dynamics of a few sodium atoms in presence of a cold potassium cloud. *Scientific Reports*, 12:2422, 02 2022.
- [114] John Weiner, Vanderlei S. Bagnato, Sergio Zilio, and Paul S. Julienne. Experiments and theory in cold and ultracold collisions. *Rev. Mod. Phys.*, 71:1–85, Jan 1999.
- [115] T Fiegele, G Hanel, I Torres, M Lezius, and T D Märk. Threshold electron impact ionization of carbon tetrafluoride, trifluoromethane, methane and propane. *Journal of Physics B: Atomic, Molecular and Optical Physics*, 33(20):4263–4283, sep 2000.
- [116] S. J. M. Kuppens, K. L. Corwin, K. W. Miller, T. E. Chupp, and C. E. Wieman. Loading an optical dipole trap. *Phys. Rev. A*, 62:013406, Jun 2000.
- [117] Nicolas Schlosser, Georges Reymond, Igor Protsenko, and Philippe Grangier. Sub-poissonian loading of single atoms in a microscopic dipole trap. *Nature*, 411:1024–7, 07 2001.
- [118] Daniel Steck. Sodium D line data. 01 2000.

Acknowledgement

Doing a PhD is not easy, and doing a PhD during a pandemic is particularly challenging. Therefore, I have a list of people I would like to express my appreciation at this particular moment. My journey in Heidelberg has been epic because of every single one of you.

I would like to thank Prof. Dr. Markus Oberthaler for being my first referee and supervisor. He has always been a cool man and picked me up during the most difficult time of my journey in Heidelberg and spent all these time with me pointing out the direction. It would be very difficult for me to cross the line without you.

I would like to thank Jun.-Prof. Dr. Lauriane Chomaz for being my second referee, she has always been helpful and has shown a tremendous understanding of the difficulties of the experiment.

I would like to thank Prof. Dr. Thomas Gasenzer and Prof. Dr. Werner Aeschbach to be in my thesis committee as well as all the insightful discussions.

I would like to thank Apoorva for being so annoying during her time in the lab.

I would like to thank Lisa for the work on atom counting and helping me through the tough time during this work.

I would like to thank Rohit, Jan and Lilo for their help during my time in the lab. All the Indian food I had with Rohit, all the Chelsea banter with Jan and for Lilo all the espresso tonic and vacuum time together. This work would not have been possible without any of you.

I would like to thank Yannick and Gopal for explaining to me all these complicated theories which I still do not really understand.

I would like to thank Dr. Helmut Strobel for all the detailed experimental discussions and efforts for this work.

I would like to thank the Synqs and Matterwave family for all the amazing ideas during seminars and gatherings.

NaLi has taught me a great lesson in both science and life in general through all her imperfections. However, the journey to improve the machine is both challenging and fun. Therefore, thank you NaLi and rest in peace.

Finally, I would like to say thank you to Fred. Although we could not complete the journey together, we had a great time together working on this machine. Thank

you for giving me the freedom to do what I would like to do and supporting me for as long as you could.